INVESTIGATIONS ON THE CHARGE ORDER MELTING IN $Pr_{0.5}Ca_{0.5}MnO_3$ AND ITS INFLUENCE ON SUPERCONDUCTIVITY AND TRANSPORT BEHAVIOUR OF $YBa_2Cu_3O_{7-\delta}$ THIN FILMS

By

DIPAK KUMAR BAISNAB
(Enrollment No. PHYS 02200704008)

Condensed Matter Physics Division
Indira Gandhi Centre for Atomic Research
Kalpakkam, India

A thesis submitted to the

Board of Studies in Physical Sciences

In partial fulfillment of requirements

For the Degree of

DOCTOR OF PHILOSOPHY
Of
HOMI BHABHA NATIONAL INSTITUTE

February, 2013

Homi Bhabha National Institute

Recommendations of the Viva Voce Board

As members of the Viva Voce Board, we certify that we have read the dissertation prepared by **Dipak Kumar Baisnab** titled **"Investigations on the charge order melting in $Pr_{0.5}Ca_{0.5}MnO_3$ and its influence on superconductivity and transport behaviour of $YBa_2Cu_3O_{7-\delta}$ thin films"** and recommend that it may be accepted as fulfilling the dissertation requirement for the Degree of Doctor of Philosophy.

-- Date
Chairman

-- Date
Guide/Convener

-- Date
Examiner

-- Date
Member 1

-- Date
Member 2

-- Date
Member 3

Final approval and acceptance of this dissertation is contingent upon the candidate's submission of the final copies of the dissertation to HBNI.

Certificate

I hereby certify that I have read this dissertation prepared under my direction and recommend that it may be accepted as fulfilling the dissertation requirement.

Dr. A. Bharathi

Date:

Place:

STATEMENT BY AUTHOR

This dissertation has been submitted in partial fulfillment of requirements for an advanced degree at Homi Bhabha National Institute (HBNI) and is deposited in the Library to be made available to borrowers under the rules of the HBNI.

Brief quotations from this dissertation are allowable without special permission, provided that accurate acknowledgement of source is made. Requests for permission for extended quotation from or reproduction of this manuscript in whole or in part may be granted by the Competent Authority of HBNI when in his or her judgment the proposed use of the material is in the interests of scholarship. In all other instances, however, permission must be obtained from the author.

Dipak Kumar Baisnab

DECLARATION

I, hereby declare that the investigation presented in the thesis has been carried out by me. The work is original and has not been submitted earlier as a whole or in part for a degree / diploma at this or any other Institution / University.

Dipak Kumar Baisnab

To

My beloved family

ACKNOWLEDGEMENTS

First of all, I would like to thank my supervisor, Dr. A. Bharathi for her advice, guidance and patience during the project. Her constant encouragement and freedom helped me to work more efficiently.

I am greatly indebted to Mr. M. P. Janawadkar whose active collaboration, endless patience and moral support made this thesis a reality. He has always been a source of inspiration for me.

My sincere thanks are due to members of my Doctoral Committee, Dr. C. S. Sundar, Dr. T. Jayakumar and Dr. P. Kuppusami, whose constant advice and encouragement have been extremely useful in shaping this thesis.

I must express my sincere thanks to Dr. Awadhesh Mani and Dr. T. Geetha Kumary for their assistance during the execution of experiments and several fruitful discussions.

I would like to thank Mr. A. T. Satya, Mr. Shilpam Sharma, Dr. J. Janaki, Dr. R. Nithya, Mr. R. M. Sarguna and Dr. K. Vinod for their help in experiments without which this thesis would not have been completed.

It is my pleasure to thank Mr. N. R. Sanjay Kumar, Dr. Arindam Das and Mr. L. M. Sundaram for their affection, friendly company and cooperation.

I gladly recall the friendship I enjoyed with my colleagues, Mr. R. Baskaran, Dr. L. S. Vaidhyanathan, Dr. K. Gireesan, Mr. R. Nagendran, Mr. A. V. Thanikai Arasu, Mr. N. Chinnasamy and Mrs. G. Chinnamma.

I thank Dr. C. S. Sundar, Director, MSG, for his interest in my work as well as support in carrying out the research. I express my sincere thanks to all the MSG members for providing an excellent environment. I would like to thank Director, IGCAR for granting me permission to register for Ph. D.

Finally, I would like to thank my parents, my wife, daughter and son, and my brother for their support throughout my life without which this endeavour would not have been successful.

Dipak Kumar Baisnab

CONTENTS

Chapters:

on T_c of YBCO in PCMO/YBCO bilayer film

SYNOPSIS

Introduction:

The study of oxide heterostructures based on strongly correlated electron systems has emerged as an active and promising area of research in recent times [1,2]. The fabrication of heterostructures incorporating high temperature superconductors (cuprates) and manganites by using modern thin film deposition techniques such as laser ablation and molecular beam epitaxy [3,4] has enabled the study of exotic phenomena such as oscillation of superconducting transition temperature (T_c) as a function of ferromagnetic layer thickness, spin triplet superconductivity, domain wall superconductivity, depression of superconductivity because of proximity to a ferromagnetic layer, superconducting spin switch effect, Josephson effect involving two spin singlet superconducting layers separated by a half-metallic ferromagnet etc. [5-9]. Cuprate / manganite multilayer heterostructures are unique compared to several other classes of multilayers due to the structural compatibility of these materials which enables formation of high quality heterostructures with sharp interfaces [3,4]. The high transition temperature of cuprate superconductors viz., $YBa_2Cu_3O_{7-\delta}$ ($T_c \geq 90K$), $Bi_2Sr_2CaCu_2O_8$ ($T_c=90K$), $Tl_2Ba_2CaCu_2O_8$ ($T_c=110K$), $HgBa_2CaCu_2O_8$ ($T_c=134K$) etc. opened up the possibility of applications at liquid nitrogen temperature. $YBa_2Cu_3O_{7-\delta}$ (YBCO) has been chosen in the present study due to its robust T_c, that can easily be optimized by oxygen annealing. In addition, YBCO exhibits better phase stability, high crystalline quality, high flux pinning properties and low surface resistance [10]. The most interesting property of manganites is the occurrence of high magnetoresistance which is attributed to the coupled metal-insulator and ferromagnetic-paramagnetic phase transitions [11]. In thin film heterostructures of manganites and cuprate superconductors, the superconducting and magnetic orders influence each other and the latter's physical properties can be controlled by application of magnetic/electric field, light and electric current [24-27]. Hence, altering the property of manganite overlayer can in turn affect the T_c of YBCO. These structures, therefore, have opened up the possibility of studying several interesting phenomena involving ferromagnetism and superconductivity, which are known to be antagonistic in nature in the bulk form [12-17]. In FM/SC thin film heterostructures, superconductivity can be influenced mainly by two mechanisms: first, the direct proximity effect involving leakage of Cooper pairs inducing weak superconductivity across the interface and second, the injection of either unpolarized or spin polarized quasiparticles into the superconducting layer which results in the suppression of the superconducting energy gap. Manganites have been used as a potential source of spin polarized carriers [18-22] since they order magnetically at low temperature under an applied magnetic field.

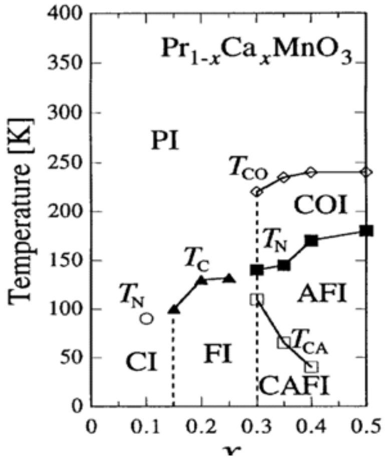

Fig.1. Phase diagram of PCMO. PI, FI, AFI,COI and CAFI denote paramagnetic insulator,ferromagnetic-insulator, antiferromagnetic insulator, charge-ordered insulator and canted AF insulator states respectively.

Manganites such as, $La_{1-x}Sr_xMnO_3$, $La_{1-x}Ca_xMnO_3$ etc. have been extensively studied in literature along with YBCO for the study of FM/SC thin film heterostructures [12-16]. However, less attention has been paid on $Pr_{1-x}Ca_xMnO_3$ for forming thin film heterostructures. $Pr_{1-x}Ca_xMnO_3$ is a hole doped manganite [23]. In this compound, no stable ferromagnetic metallic phase exists at low temperatures for any Ca content. Fig.1. shows the phase diagram of $Pr_{1-x}Ca_xMnO_3$ for different calcium concentrations. It is evident from the figure that this compound exhibits a transition from a paramagnetic insulating phase (PI) to charge ordered insulating (COI) phase at relatively high temperatures in a wide doping range x=0.3-0.5. At low temperature and zero field these compounds are antiferromagnetic insulators (AFI) with a large resistivity. A canted spin state is seen at low temperature between x=0.3 and 0.4 [23]. For x=0.15 to 0.3, a FM insulating (FI) phase is seen. As is evident from fig.1, the onset of charge ordering temperature (T_{CO}) is ~ 240K for the Ca concentration x = 0.5. This charge ordered insulating phase of the manganite is seen to transform to a conducting FM phase by application of magnetic or electric field, substrate induced strain, photon exposure etc [24-27]. It is known that these external variables can induce insulator-metal transition (MIT) in $Pr_{0.5}Ca_{0.5}MnO_3$ thin films as well. Thus, a heterostructure comprising of a $Pr_{0.5}Ca_{0.5}MnO_3$ (PCMO) and $YBa_2Cu_3O_7$ (YBCO) thin films is suitable for investigations of a variety of interesting physical phenomena, especially under the control of external variables like electric and magnetic fields. This thesis focuses on the experimental investigations that examine the influence of charge order melting of PCMO on YBCO. The CO melting is achieved by application of current, magnetic field and substrate induced strain.

The major findings reported in this thesis are given below:

1. Deposition parameters were fine tuned to standardize the process of pulsed laser deposition of YBCO and PCMO thin films having a good quality as qualified by higher superconducting transition temperature T_c (for YBCO) and lower surface roughness.
2. PCMO thin films grown on MgO substrate exhibit a decrease in charge order transition temperature (T_{CO}) with decrease in film thickness. A field induced insulator to metal transition corresponding to charge order (CO) melting is

observed for films with very small thickness. The charge order melting and the observed variation in T_{CO} could be understood based on the effects related to substrate induced strain.

3. Electric field (or current) was also found to induce the CO melting in PCMO thin films. Current and magnetic field dependent resistance measurements carried out on PCMO/YBCO bilayer showed a decrease in the T_c of YBCO with increase in current. A hump like feature appears in the resistivity near T_c for higher values of applied current. The bilayers exhibit higher critical current (J_c) values due to improved vortex pinning characteristics. The results can be explained on the basis of the formation and growth of ferromagnetic clusters on account of charge order melting in PCMO upon application of high current and magnetic field.
4. In the PCMO/YBCO/PCMO trilayer heterostructures, the combined effect of current and substrate induced strain was studied with and without applied magnetic field. PCMO/YBCO/PCMO trilayer having a smaller thickness of bottom PCMO layer (strained film), exhibited a larger suppression of T_c with applied magnetic field as compared to the film with larger thickness of the bottom PCMO layer (relaxed film). A negative magnetoresistance (MR) is observed in the strained film near the hump like anomaly in R(T), prior to T_C, whereas a positive MR is observed in the relaxed film. These experimental observations could be explained on the basis of spin injection and proximity effects due to the growth of FM clusters inside the strained PCMO layer.

This thesis is divided into six chapters, and the content of each is briefly summarized below.

Chapter 1

In this chapter, overview of the manganites, specially $Pr_{1-x}Ca_xMnO_3$ will be presented and the physical properties of this system will be discussed. The mechanism of colossal magnetoresistance (CMR) effect will be described, which, in turn will be used to explain the charge order melting of $Pr_{1-x}Ca_xMnO_3$. The chapter also presents a brief account of the Resistor network model and the Random Field Ising and Heisenberg Models, which have been invoked in the literature for understanding the CO melting through percolation mechanism [28-33]. An overview of the superconducting properties of the YBCO and a brief discussion on the flux vortex dynamics in type II superconductor will be given subsequently. The physical phenomena governing the behaviour of Ferromagnet / Superconductor bilayer and Superconductor / Ferromagnet / Superconductor trilayer heterostructures will be described. The proximity effect across a superconductor-ferromagnet interface and the effect of injection of spin polarized carriers into the superconducting layer will be discussed briefly.

Chapter 2

The details of experimental techniques starting with the preparation of superconducting YBCO and charge ordered, insulating PCMO compound will be discussed in this chapter. The Pulsed Laser Deposition system, will be described in detail, with emphasis on standardization of the deposition parameters carried out for the realization of high quality thin films and heterostructures. Photolithography technique for the fabrication of the YBCO microbridges, used for the measurement of the J_c of YBCO thin film, is discussed in this chapter; the RF ion beam etching system, which was used to etch photolithographically patterned YBCO thin film to realize desired geometries is also described. Use of surface profiler for the measurement of the thickness of the deposited thin films and microbridges will be discussed in detail. Characterization of both the thin films deposited by PLD technique as well as bulk materials using X-ray diffraction (XRD) is discussed subsequently. Then, a brief description of the magnetoresistance measurement (MR) system and the four probe dipstick based electrical resistance measurement system used for measurement of transport properties of the thin film heterostructures down to liquid helium temperatures will be described. A brief discussion on Vibrating Sample Magnetometer (VSM) used for magnetic characterisation characterization will be prsented at the end of this chapter

Chapter 3

In this chapter, the process used for the deposition of YBCO thin films on different substrates and their experimental characterization have been described in detail. Thin films of YBCO were deposited on various substrates viz. MgO, $SrTiO_3$ (STO) and $LaAlO_3$ (LAO) under identical deposition parameters and their T_c and J_c values were estimated. The thin films deposited on STO substrate showed the highest T_c value of 92 K. The effect of oxygen annealing on the T_c of YBCO film is also studied. This chapter also presents the experimental study of the substrate induced strain effect on charge-ordered PCMO thin films. Thin films of PCMO with different thicknesses ranging from 25 to 200 nm were prepared. XRD measurements reveal that the thin films have a (121) orientation. The nature of the strain experienced by the films is obtained from high resolution X-ray rocking curve measurements. Resistance R(T) measurements were performed under different applied magnetic fields (0T to 12T) in the temperature range of 4K to 300K. A field induced charge order melting, manifested as a metal-insulator transition (MIT), has been observed for films with very small thicknesses of PCMO film. The charge order transition temperature T_{CO} and the magnetic field induced charge order melting are observed to depend on the nature of the strain that is experienced by the film.

Chapter 4

This chapter examines the proximity and spin injection effects of PCMO on the T_c of YBCO in PCMO/YBCO bilayer film. PCMO and YBCO thin films were successively deposited on LAO substrate using pulsed laser deposition technique to form the bilayer, which was characterizated by XRD and magnetoresistance (MR) measurements. R(T) measurements were performed for different applied currents (10μA to 40mA) and magnetic fields (0T to 12T). It has been observed that the T_c decreases with increase in current at a given field. A pronounced increase in R(T), manifested as a hump in R(T), is observed just above T_c at higher values of current. The height of the hump like feature increases with increase in current. Remarkably this upturn in R(T) gets strongly suppressed under external magnetic fields of 6T and 12T. These experimental results have been explained on the basis of the formation and growth of ferromagnetic clusters on account of charge order melting in $Pr_{0.5}Ca_{0.5}MnO_3$ due to the application of high current and magnetic fields.

Chapter 5

In this chapter, we demonstrate the possibility of controlling the superconducting properties of YBCO thin film by nucleating ferromagnetic clusters in a PCMO thin film under the influence of a suitable control variable. A bilayer thin film of PCMO/YBCO has been deposited on $SrTiO_3$ in which only about half of the bottom YBCO film is covered by the top PCMO layer. R(T) measurements were performed for different applied currents (10μA to 40mA) and magnetic fields (0T to 12T). An upturn in R(T) is observed just above T_c similar to that in the case of PCMO/YBCO bilayer film grown on LAO substrate. The suppression of T_c is higher on the bilayer side of the sample compared to that on the YBCO side. Arrhenius plot of logR(T) versus 1/T is carried out to estimate the flux pinning parameters using thermally activated flux flow (TAFF) model [34]. It has been observed that the value of the activation energy,U_0, inferred for the bilayer side is higher compared to that observed for the YBCO side. In the bilayer side, the YBCO thin film is in direct contact with the PCMO layer so that the FM clusters nucleated in the PCMO layer contribute to the enhancement of pinning strength leading to the observation of the U_0 on the bilayer side as compared to that for the YBCO side. These results also reveal that the nucleation and growth of FM clusters increase the pinning strength in the bilayer side but simultaneously weaken the superconductivity properties due to spin injection and proximity effect.

Chapter 6

This chapter describes the combined effect of current and strain induced CO melting on the superconducting YBCO in PCMO/YBCO/PCMO trilayer thin film heterostructures deposited on MgO substrate. The experiments were performed on PCMO/YBCO/PCMO trilayers having different layer thicknesses for the bottom PCMO layer and the same thickness(~100nm) for the sandwiched YBCO layer. In one of the trilayers, designated as the strained film, the bottom PCMO film had a relatively low thickness of ~ 40nm where the strain in the PCMO film plays an important role in determining the superconducting properties of YBCO. In the other trilayer, designated as the relaxed film, the bottom PCMO thin film had a relatively higher thickness of ~ 110nm. R(T) measurements were carried out under magnetic fields of up to 8 T and at two different values of applied current (1mA and 5mA). The strained film showed a larger suppression of T_c with magnetic field compared to the relaxed film. In the measurement of temperature dependence of electrical resistivity, a hump-like anomaly was observed near the onset of T_c due to the competition between charge ordered and ferromagnetic states in the PCMO layer and the superconducting state in the YBCO layer. A negative magnetoresistance (MR) is observed in the strained film near the hump like anomaly whereas a positive MR is observed in the relaxed film. R(H) curves measured at various temperatures are compared for both the trilayers. Comparison of the behavior of the two trilayers clearly shows that the trilayer under the simultaneous influence of both strain and electric field exhibits a stronger spin injection behavior compared to the trilayer which was subjected to the effect of electric field only. A brief summary of the thesis and the major conclusions are discussed chapter 7. The directions for possible future research have been presented at the end of this chapter.

References:

[1] A. I. Buzdin, Rev. Mod. Phys. 77, 935 (2005)

[2] F. S. Bergeret, A. F. Volkov, and K. B. Efetov, Rev. Mod.Phys. 77, 1321 (2005)

[3] D. B. Chrisey, G. K. Hubler, Pulsed Laser Deposition of Thin Films, Wiley, New York, Wiley 1994

[4] D. G. Schlom and J. S. Harris, Jr., in Molecular Beam Epitaxy: Applications to Key Materials, edited by R. F. C. Farrow (Noyes, Park Ridge, 1995), pp. 505–622.

[5] F. S. Bergeret, A. F. Volko, and K. B. Efetov, Rev. Mod. Phys. 77, 1321 (2005)

[6] W. Gillijns, A. Yu. Aladyshkin, M. Lange, M. J. Van Bael, and V. V. Moshchalkov, Phys. Rev. Lett. 95, 227003 (2005)

[7] Z. Yang, M. Lange, A. Volodin, R. Szymczak, and V. Moshchalkov, Nature Mat. 3, 793 (2004)

[8] LR Tagirov, Phys. Rev. Lett. 83, 2058 (1999)

[9] M. Eschrig, J. Kopu, J.C. Cuevas and G. Schön Phys. Rev. Lett. 90, 137003 (2003)

[10] R. Wordenweber, Supercond. Sci. Technol. 12, R86-R102 (1999)

[11] A.P. Ramirez, J. Phys.: Condens. Matter 9, 8171 (1997)

[12] Daniel Hsu, L. G. Lin, C. P. Chang, C. H. Chen, C. H. Chiang, W. C. Chan and W. F. Wu, J. Appl. Phys. 103, 07C710 (2008)

[13] J. G. Lin, Daniel Hsu, W. F. Wu, C. H. Chiang and W. C. Chang, J. Appl. Phys. 101, 09G106 (2007)

[14] Hanns-Ulrich Habermeier, Soltan Soltan and Joachim Albrecht, Physica C 460-462, 32(2007)

[15] J. G. Lin, S. L. Cheng, C. R. Chang and D. Y. Xing, J. Appl. Phys. 98, 023910(2005)

[16] Daniel Hsu, L. G. Lin, C. P. Chang, C. H. Chen, W. F. Wu,C. H. Chiang and W. C. Chan Appl. Phys. Lett. 90, 162504(2007)

[17] W. Westhauser, S. Schramm, J. Hoffmann and C. Jooss Eur. Phys. J. B 53, 323(2006)

[18] V. Peña, Z. Sefrioui, D. Arias, C. Leon, and J. Santamaria PhysRevB.69.224502 (2004)

[19] Z. Sefrioui, D. Arias, V. Pena, J. E. Villegas, M. Varela, P. Prieto, C. Leon, J. L. Martinez, and J. Santamaria, Phys. Rev. B 67, 214511 (2003)

[20] Z. Sefrioui, M. Varela, V. Pena, D. Arias, C. Leon, J. Santamaria, J. E. Villegas, J. L. Martinez, W. Saldarriaga, and P. Prieto, Appl. Phys. Lett. 81, 4568 (2002)

[21]M. van Zalk, M. Veldhorst, A. Brinkman, J. Aarts, and H. Hilgenkamp, Phys. Rev. B 79, 134509 (2009)

[22] Przyslupski P2005 Phys. Status Solidi c 2 1625

[23] Elbio Dagotto, Nanoscale Phase Seperation and Colossal Magnetoresistance: The Physics of Manganites and Related Compounds, May 27, 2002, Springer-Verlag

[24] A. Asamitsu, Y. Tomioka, H. Kuwahara and Y. Tokura, Nature 388, 50 (1997).

[25] V. Kiryukhin, D. Casa, J. P. Hill, B. Kelmer, A. Viglinate, Y. Tomioka and Y. Tokura, Nature 386, 813 (1997).

[26] W. S. Tan, L. Yang, X. S. Wu, S. S. Jiang, T. L. Kam, J. Gao, J. Wang and Z. H. Wu Physica C 384,437(2003)

[27] D. K. Baisnab et al. J. Magn. Magn. Mater 323, 2823(2011)

[28] Y. Imry and S-K. Ma: Phys. Rev. Lett. 35 (1975) 1399

[29] E. T. Seppala and M. J. Alava, Phys. Rev. E 63, 066109 (2001)

[30] A. P. Young, ed., Spin Glasses and Random Fields, World Scientific, Singapore (1998)

[31] Introduction to Percolation Theory, 2nd ed., D.Staufferand A.Aharony, Taylor and Francis, London 1994

[32] M. Mayr, A. Moreo, J. A. Vergés, J. Arispe, A. Feiguin, and E. Dagotto Phys. Rev.Lett. 86, 135 (2001)

[33] I. Zutic, J. Fabian, and S. Das Sarma, Journal of Physics Condensed Matter, 16, 5071 (2004)

[34] T. T. M. Palstra, B. Batlogg, R. B. Van Dover, L. F. Schneemeyer and J. V. Waszczak, Phys. Rev. B 41, 6621(1990)

List of figures:

List of tables:

Chapter 1

Introduction

1.1 Introduction:

Although ferromagnetism and superconductivity have been separately investigated for several decades, investigations on the interplay between these two antagonistic orders have generated a great deal of interest in modern solid state physics. While ferromagnetism was already known to the ancient Greeks, its origin remained a complete mystery for several centuries. The experimental and theoretical investigations aimed at understanding the origin of ferromagnetism could make significant progress only after the advent of the modern quantum theory, which emerged as the new tool to understand the underlying physics [1-6]. Since then, however, the phenomenon of ferromagnetism has attracted a lot of attention from researchers. Different types of magnetic materials have been discovered and new theories have been advanced to explain their behaviour [7-9]. The discovery of superconductivity is comparatively recent one; this extra-ordinary phenomenon was discovered in 1911 by H.K. Onnes [10], soon after the liquefaction of helium became possible. Despite the tireless efforts of many researchers, it had not been understood until 1957, when the trio, comprising of J. Bardeen, L.N. Cooper and J.R. Schrieffer, devised a successful quantum mechanical theory to account for the amazing properties of superconductors [11]. In the more recent times, this formalism has been suitably modified and extended to explain the properties of the newly discovered superconducting materials [12,13]. The discovery of high temperature superconductors by J.G. Bednorz and K.A. Muller, in 1986, generated a tremendous flurry of research activities on superconducting materials [14]. New superconducting materials such as iron-based pnictides continue to be discovered [15-17].

The antagonism between ferromagnetism and superconductivity was recognised very early by Ginzburg [18]. Nevertheless, not much attention has been paid to investigating the behavior of thin film heterostructures comprising ferromagnetic and superconducting thin films. However, recent development of artificially fabricated thin film heterostructures has made it possible to bring the ferromagnetic phase in close proximity to the superconducting phase. A number of exotic phenomena such as oscillation of superconducting transition temperature (T_c) as a function of ferromagnetic layer thickness, spin triplet superconductivity [19,20], domain wall superconductivity [21-23], depression of superconductivity because of proximity to a ferromagnetic layer [24-26], superconducting spin switch effect [27-29], Josephson effect involving two spin singlet superconducting layers separated by a half-metallic ferromagnet [30] etc. have stimulated further scientific research on such systems. The first studies on heterostructures involving thin films of un-conventional superconducting materials and ferromagnetic materials were reported in late 1990s [31,32]. The use of high temperature superconductors and ferromagnetic manganites unveiled a rich potential for possible application in devices based on injection of spin polarized quasiparticles from the manganite into the superconducting layer. Soon, novel phenomena based on proximity-effect were discovered, which operated at a much larger length scale than the ones observed in conventional heterostructures [33,34]. Detailed experimental and theoretical investigations and discovery of several exotic interfacial phenomena attracted more researchers to this field to further investigate the properties of such heterostructures.

The goal of this thesis is to investigate the influence of external perturbations like strain/ electric current/ magnetic field to induce the charge order melting in

$Pr_{0.5}Ca_{0.5}MnO_3$ (PCMO) thin films and its effect on the properties of superconducting $YBa_2Cu_3O_{7-\delta}$ (YBCO) in PCMO/YBCO thin film multilayer heterostructures. The work mainly involved the following investigations: (a) the effect of substrate induced strain on the charge order melting in PCMO thin films (b) current induced charge order melting of PCMO and its effect on T_c of YBCO in PCMO/YBCO bilayer films and (c) current and substrate induced strain effect on PCMO/YBCO/PCMO trilayer thin film structures. The results obtained in these experimental investigations have been explained with the help of a model based on a few concepts which include the phase separation and percolation theory for charge order manganites, proximity and spin injection in superconductor/ferromagnet interfaces and the thermally activated vortex flow in the YBCO superconductor. In this chapter, we present a very brief overview of these concepts that are necessary to account for the experimental observations reported in this thesis.

1.2 Overview of Manganite materials:

In solid state physics, mixed valence oxides with a generic formula $RE_{1-x}M_xMnO_3$ (RE=rare earth trivalent cation, M= divalent cation) with three dimensional perovskite type structure are often referred to as manganites. The colossal magnetoresistance (CMR) effect and the occurrence of metallic phases with a fully spin polarized conduction band in manganites have kindled a renewed interest in the field of both basic and applied research [35]. They show a broad spectrum of electronic and magnetic properties which arise from their unique structure (see Figure 1.1).

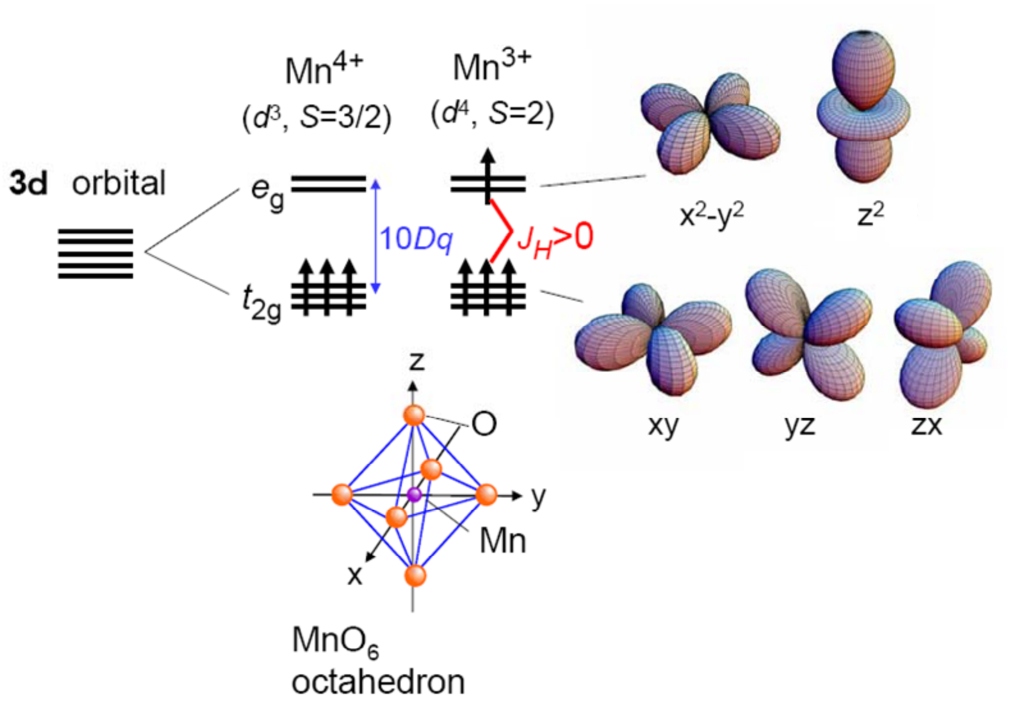

Fig. 1.1. *Splitting of 3d orbital of a transition metal atom (Mn) due to the octahedral crystal field of oxygen ions. 10Dq is the crystal field splitting whereas* J_H *is the Jahn-Teller distortion [36].*

In the structure of $RE_{1-x}M_xMnO_3$ oxides, the ratio of Mn^{3+} to Mn^{4+} is tuned by the stoichiometry (i.e., the ratio x of tri- and divalent cations). The atomic arrangement in the crystal is in such a way that the Mn-cations are octahedrally coordinated by oxygen anions. These octahedrons form a lattice with the A- and B-cations located in the gaps. Therefore the oxygen octahedrons gets distorted by the change in the ratio of RE and M cations and corresponding change of the atomic radii. Inside the octahedrons, overlap between the Mn 3d-orbitals and the oxygen 2p-orbitals depends on the orientation of the affected orbitals and on the extent of the distortion of the oxygen octahedrons (see Figure 1.1). It determines the Coulomb repulsion between the electrons occupying the orbitals and thus modifies the energy levels of the orbitals. In the case of undistorted oxygen octahedrons, this leads to a crystal field splitting of the five Mn 3d-orbital levels into two

e_g-levels with increased energy and three t_{2g}-levels with reduced energy (see Figure 1.1). In the case of three Mn 3d-electrons (Mn^{4+}), only the t_{2g}-levels are occupied. Because of the Hund's coupling, these electrons have parallel aligned spins. The total spin of such a Mn^{4+} ion is coupled antiparallel to the one of the next nearest Mn^{4+} by a coupling that is mediated via a small orbital overlap with the oxygen 2p-electrons (super exchange) [37]. In the case of four Mn 3d-electrons (Mn^{3+}), the strong Hund's coupling leads to the occupation of three t_{2g}-orbitals and one e_g-orbital. It can then be energetically favourable for the crystal to stretch the oxygen octahedron along the z-axis and reduce the energy of the d_{z2}-orbital while increasing the energy of the d_{x2-y2}-orbital (Jahn-Teller effect) [37].

1.3 The manganites and the Jahn-Teller effect.

In the manganites, the presence of the Mn^{+3} ions produces the Jahn-Teller effect [37,38], that affects both the crystalline and electronic structure and dramatically affects the physical properties of the materials. As stated already, the electronic configuration of the Mn^{3+} ion is $t^3_{2g}\ e^1_g$; in this configuration, a single electron is present in the two-fold degenerate e_g level. According to the Jahn-Teller theorem, the $Mn^{3+}O_6$ groups present in $RE_{1-x}M_xMnO_3$ are energetically unstable towards distortion, which is expected to result in a reduction of the total energy of the system as a consequence of a lifting of the degeneracy of the e_g levels. The degree of distortion is determined by the competition between the gain in energy due to the e_g level splitting and the increase of the elastic energy associated with the lattice distortion itself [38].

Let us assume that the octahedron elongates (distorts) along the z-axis. Then the crystalline field loses the cubic symmetry around the Mn ion, and the energies of the d_{x2-}

$_{y2}$ and d_{xy} orbitals increase, because they are brought closer to the oxygen p orbitals. On the contrary, the energy of the d_{z2}, d_{xz}, and d_{yz} orbitals decreases, because they recede further from the oxygen p orbitals as shown in figure 1.2. The distorted octahedron then has a considerably lower electronic energy, but at the cost of a slightly higher elastic energy caused by the deformation. Therefore, the octahedron has a tendency to distort spontaneously if the gain in electronic energy offsets the loss in elastic energy. This effect is kown as Jahn-Teller (JT) effect [37, 38].

The absence of an unpaired electron in the e_g orbitals of the Mn^{4+} ion makes it JT inactive. It may also be noted that the JT effect is local since it considers the environment of a single Mn ion.

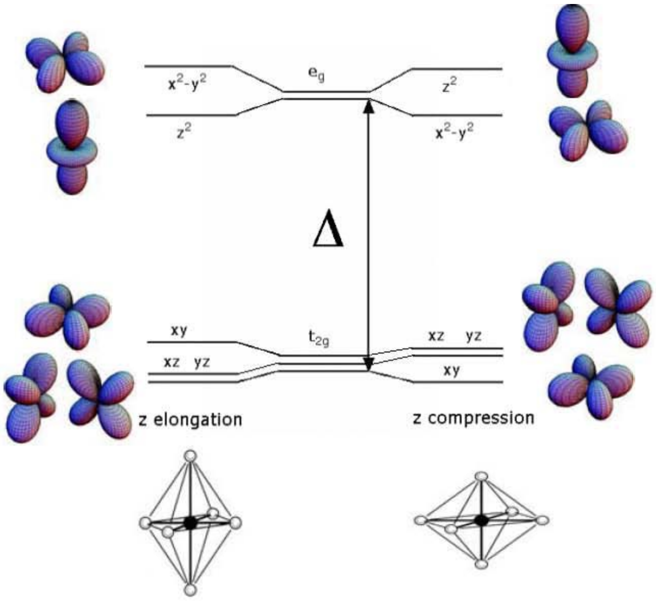

Fig. 1.2. *JT effect on d-energy levels in the case of elongation and of compression along z directionof the* Mn^3O_6 *octahedra.*

Since the neighbouring Mn ions have common ligands (e.g. oxygen), a local JT deformation around one centre interacts with the corresponding deformation of its neighbours, giving rise to correlated displacements. Thus the symmetry of the crystal as a whole is reduced. This is known as the cooperative Jahn-Teller effect (see figure 1.3) [39].

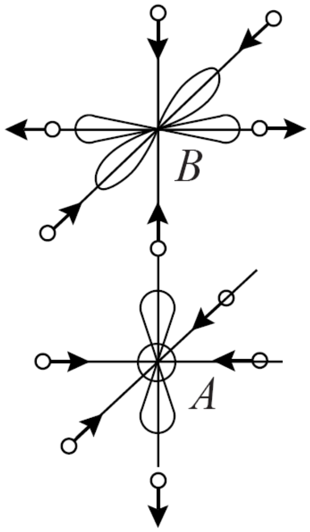

Fig. 1.3. *An illustration of cooperative JT effect where the correlation of local deformations around neighbouring JT ions A and B are shown with the corresponding orbital occupation.*

1.4 Orbital and charge ordering.

The orbital ordering arises when the d orbitals in the crystal are in a spatially ordered arrangement. Strongly associated with the carrier concentration, it develops when the d electron occupies an asymmetric orbital [36]. The ratio Mn^{3+}/Mn^{4+} is responsible for the phenomenon of charge ordering (CO). This consists of a periodic distribution of electric charge (i.e. e_g electrons of Mn^{3+} ions in the crystal lattice), driven by Coulomb interaction. The mobile e_g electrons may become localised at certain Mn ion positions in the lattice, forming an ordered sublattice. In principle, however, these charges do not need to be necessarily localized on the Mn sites, and in fact they could sit on the bond centres as well, or, in the most general case, on some intermediate point between those two.

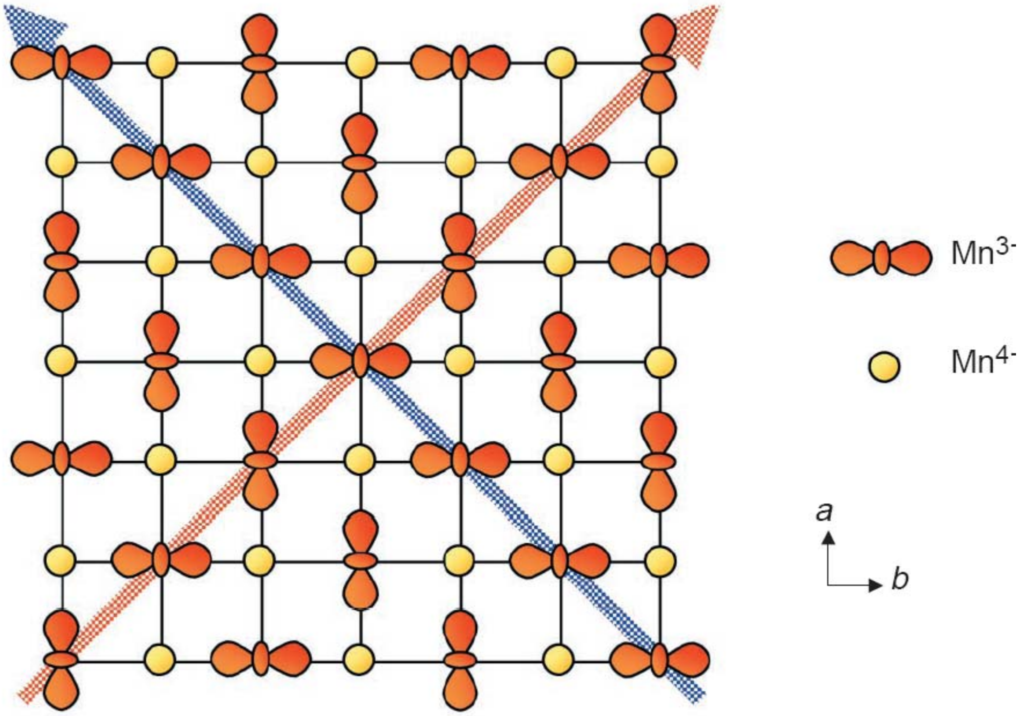

Fig. 1.4. A two dimensional schematic of orbital ordering and charge ordering. The blue and red color arrows show the identical and alternating orbitals whereas charges are identical along both the diagonals [40].

CO is mainly observed at certain special concentrations of the dopant, namely at rational fractions like, for example, x = 1/8, 3/10, 1/2, 3/4 etc. In this case, the extra electron of Mn^{3+} gets localised on alternate manganese ions, creating an ordered path of charge in the lattice (as shown in figure 1.4). The CO can be either long-ranged or short-ranged. It is evident that CO competes with the electronic conductivity, because it tends to inhibit the movement of the charges through the crystal. Compounds with long-range CO are generally insulating, but the localized CO is responsible for an enhancement of resistivity, introducing scattering centers for the mobile electrons [41].

1.5 Exchange interaction in magnetism:

1.5.1 Direct exchange.

The electronic structure of isolated Mn ions in the crystal arises due to an interaction between ions. One such effect mentioned already is the cooperative JT effect or orbital ordering. The exchange interactions are also important in this system, which can lead to some kind of long range magnetic ordering and creates the possibility of electron transfer from site to site. Primarily, exchange interactions arise in a system of fermions because of the requirement for an overall antisymmetry of the wavefunction comprising of both spatial and spin parts; difference in the energy of the spin triplet and spin singlet states is on account of different charge distributions of the corresponding orbitals since charges of the same sign cost energy when they are close together and save energy when they are farther apart. Indeed, in general, the direct magnetic interaction between a pair of electrons is negligibly small compared to this electric interaction.

Direct exchange is one type of exchange interaction through which the electrons on nearest neighbour magnetic atoms interact. The direct exchange is modelled by the Heisenberg exchange Hamiltonian:

$$H_{ex} = -\sum J_{ij} S_i . S_j$$

where J_{ij} is the exchange constant between the i-th and j-th spins, distributed on a regular lattice. Only the nearest neighbours are usually included in the summation. The magnetic properties of the crystal depend on the sign and the strength of the interaction between spins: if $J_{ij} = J > 0$ the parallel orientation of the spins is favoured, giving a ferromagnetic state. If $J_{ij} = J < 0$, the magnetic order is antiferromagnetic, having antiparallel orientation of the spins. However the manganites show some kind of indirect exchange interaction, because the Mn ions are connected through the non magnetic O ion in the lattice [39].

1.5.2 Indirect exchange: superexchange.

Superexchange is an indirect exchange interaction where two non-neighbouring magnetic ions interacts through a non-magnetic ion placed between them. This interaction was first proposed by Kramers [42] in 1934 to explain the magnetic properties observed in insulating transition metal oxides. In this case, the magnetic ions are so far apart from each other that a direct exchange interaction could not explain the presence of magnetically ordered states. In this case, which may be called as “super-exchange”, a longer range interaction is required to operate in order to account for the observed properties. The problem was thereafter treated theoretically by Anderson in 1950 [43]. He gave the first quantitative formulation showing that the superexchange favours an antiferromagnetic order.

1.5.3 Double-exchange:

The double-exchange mechanism is a type of a magnetic exchange that may arise between ions in different oxidation states. This theory was first proposed by Zener [44] and predicts the relative ease with which an electron may be exchanged between two sites. It has important implications for whether a given material is ferromagnetic, antiferromagnetic, or does not develop any long range order. For example, consider the 180 degree interaction of Mn-O-Mn in which the Mn "e_g" orbitals are directly interacting with the O "2p" orbitals, and one of the Mn ions is in Mn^{3+} state while the other Mn ion is in Mn^{4+} state. In the ground state, electrons on each Mn ion are aligned according to the Hund's rule (see the sketch in figure 1.5).

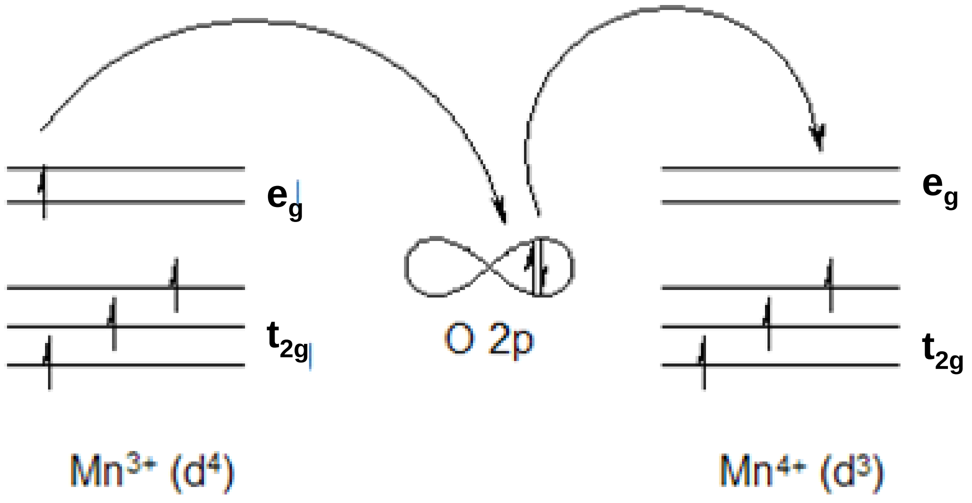

Fig. 1.5. *The sketch of the double exchange mechanism.*

If O gives up its spin-up electron to Mn^{4+}, its vacant orbital can then be filled by an electron from Mn^{3+}. At the end of the process, an electron moves between the neighboring metal ions, retaining its spin. The double-exchange predicts that this electron movement from one site to another will be facilitated more easily if the electrons do not have to change spin orientation in order to conform to the Hund's rules. The ability to hop (to delocalize) reduces the kinetic energy. Hence the overall energy saving can lead to ferromagnetic alignment of neighbouring ions.

This model is superficially similar to super-exchange. However, in super-exchange, a ferromagnetic or antiferromagnetic alignment occurs between two atoms with the same valence (number of electrons); while in double-exchange, the interaction occurs only when one atom has an extra electron compared to the other [45].

1.6 Origin of CMR: competition of phases:

The colossal magnetoresistance (CMR) effect manifests as a drastic reduction of the resistivity of a material in the presence of an external magnetic field. The effect, observed in the manganese perovskites, was called "colossal" magnetoresistance to distinguish it from the giant magnetoresistance observed in magnetic multilayers [46]. In doped manganites $RE_{1-x}M_xMnO_3$, the origin of the CMR is connected with the presence of a metal-insulator transition. The CMR effect is observed in manganites where the coexistence of two micrometric magnetic phases in the absence of the magnetic field exists. A large number of recent experimental reports have suggested simultaneous presence of both the lattice distorted insulating and undistorted metallic phases coexisting together in manganites [47]. It is seen that the fraction and size of the metallic phase increases with the decrease in temperature. Random Field Ising Model (RFIM) has been used by Imry and Ma (1975) to explain the origin of the co existence of a large cluster of one phase in manganites even though the density is uniform [48]. RFIM are based on the competition between two tendencies: uniform state favored by one tendency and the formation of small clusters favored by the other. From the competition between these two tendencies, a situation with clusters of variable size emerges. In the presence of a magnetic field, these phases transform to a ferromagnetic metallic phase at a Curie temperature T_C. The maximum CMR effect appears near the Curie temperature T_C.

The magnetoresistance is usually defined as:

$$\frac{\Delta R}{R} = \frac{R(H) - R(0)}{R(0)}$$

where R(H) and R(0) represent the resistance in the presence and in the absence of the external magnetic field, respectively. Resistivity measurements versus temperature and applied magnetic field for the $Pr_{0.7}Ca_{0.3}MnO_3$ single crystals are shown in figure 1.6. In manganites, the origin of the CMR due to the application of magnetic field is partly connected with the double-exchange phenomenon. In a Mn^{3+} ion, the t_{2g} electrons are tightly bound to the ion but the e_g electron is itinerant. Because of the double exchange interaction, the hopping of e_g electrons between Mn sites is only permitted if the spins of two Mn ions are aligned. The magnetic field aligns the core spins and therefore increases the conductivity, especially near the Curie temperature T_C. The situation is actually more complicated as the carriers interact with phonons due to the Jahn-Teller effect.

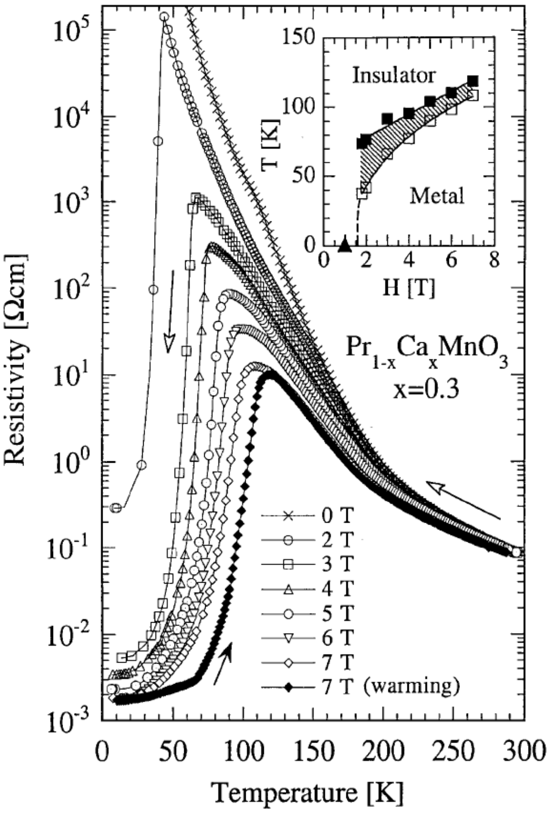

Fig. 1.6. Temperature dependent resistivity of $Pr_{1-x}Ca_xMnO_3$ at x=0.3 and various magnetic fields. Inset shows the phase diagram in the temperature-magnetic field plane where the hatched area denotes the hysteresis [49].

1.7 Effect of percolation:

The concept of percolation [50] is an important issue that has been discussed in this thesis for the explanation of the CMR effect in charge ordered $Pr_{0.5}Ca_{0.5}MnO_3$ thin film under the influence of external perturbations. The idea of percolation and its threshold was first studied formally by Broadbent and Hammersley [50]. They introduced lattice model for the flow of a fluid through a static random medium and showed that no fluid will flow if the concentration of active medium is smaller than a threshold value. In this model fluid has to flow through the 'bonds' which connect nearest neighbors located on regular lattice 'sites'. The most common statistical assumptions in this context are known as the 'bond percolation' and the 'site percolation' models. The recent interest in the percolation theory is because of the prediction that percolation effects may play a role in the metal-insulator transitions seen in some disordered systems. A class of models with random resistor network (shown in figure 1.7) has been introduced in order to simulate the details of transport properties of similar systems [51]. This model assumes that a random resistor network of insulating and metallic paths is formed inside the phase separated manganites where lattice spacing is much larger than the separation between the two neighbouring Mn ions. Hence the electrical transport properties of manganites in the CMR region are assumed to be percolative with the spread of metallic filaments across the sample [52]. Figure 1.8 shows a schematic representation of percolation through a metallic filament in a mixed phase state of manganites. In chapter 4 and chapter 6, we have used such models to explain the results of our investigations on YBCO/PCMO heterostructures.

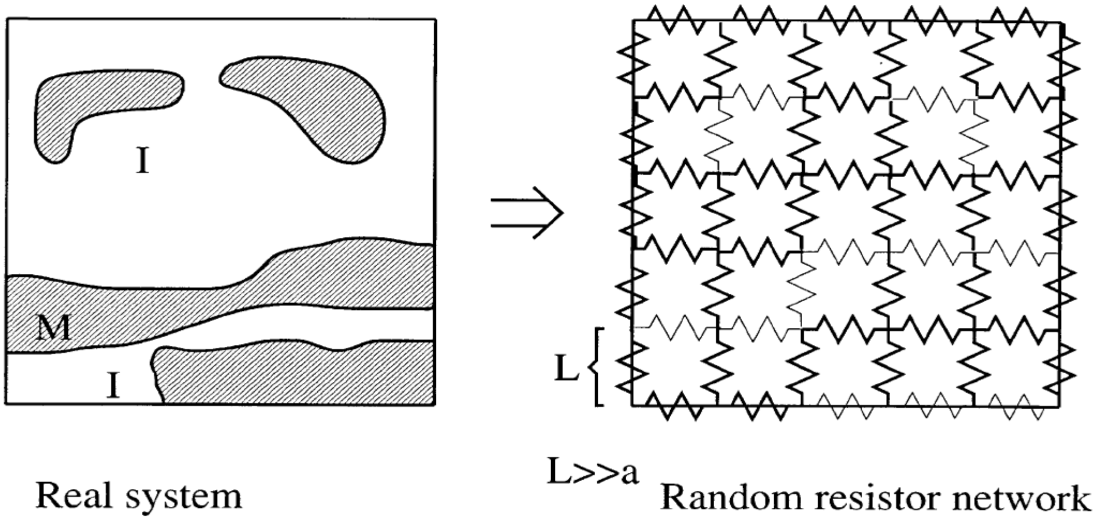

Fig. 1.7. *Schematic representation of the random resistor network approximation. On the left is a sketch of the real system with metallic and insulating regions. On the right is the resistor network where dark (light) resistances represent the insulator (metal). "a" is the Mn-Mn lattice spacing, while L is the actual lattice spacing of the resistor network [52].*

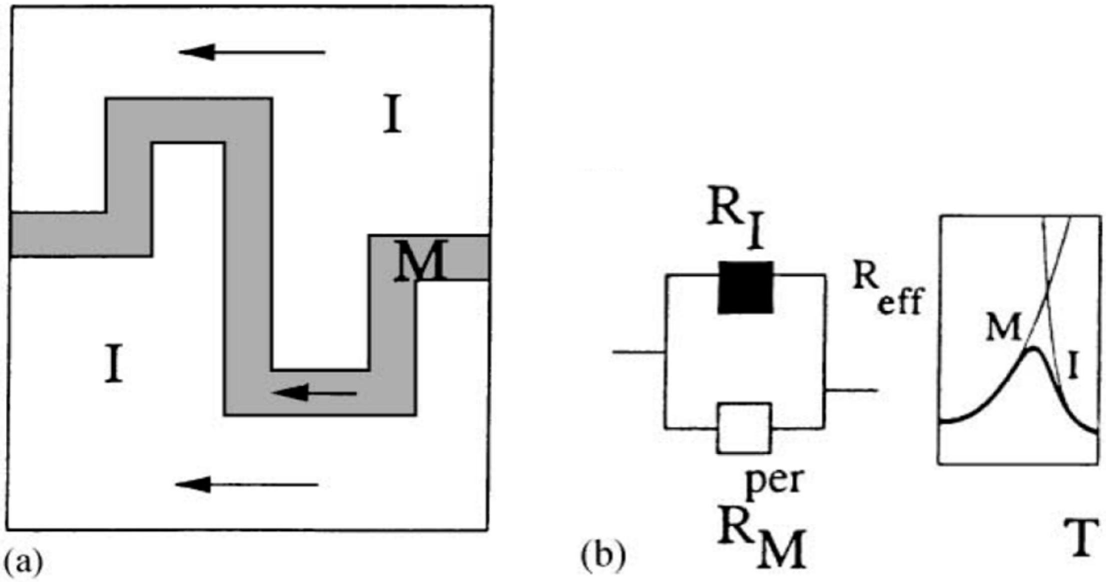

Fig. 1.8. *(a) Schematic representation of the mixed-phase state near percolation. The arrows indicate conduction either through the insulating or metallic regions depending on temperature. (b) Two resistances in parallel model for Mn-oxides. The schematic plot for the effective resistance* R_{eff} *vs. T arises from the parallel connection of metallic (percolative)* R_M^{per} *and insulating* R_I *resistances [52].*

1.8 Basic properties of $Pr_{1-x}Ca_xMnO_3$:

The undoped $PrMnO_3$ exhibits an orthorhombic distorted structure (space group Pbnm) at room temperature, and a transition at $T_N = 91$ K to an antiferromagnetic order [53]. $Pr_{1-x}Ca_xMnO_3$ is obtained by chemical doping through the substitution of Ca^{2+} into Pr^{3+} sites. Figure 1.9. shows the phase diagram of $Pr_{1-x}Ca_xMnO_3$ as a function of the Ca content (x). $Pr_{1-x}Ca_xMnO_3$ is a unique example among manganites, exhibiting insulating behaviour over the entire chemical composition x and over the entire temperature range. This is a consequence of the small ionic radius of Ca, which results in a pronounced orthorhombic distortion that favours charge localization.

Antiferromagnetic insulating (AFI) phases are stable below 100 K for $0 \leq x \leq 0.1$ doping level, followed by a region of insulating ferromagnetic (FI) phases with $T_C \leq 140$ K for $0.15 \leq x \leq 0.3$. For $0.3 \leq x \leq 0.75$, at low temperatures (≤ 240 K), $Pr_{1-x}Ca_xMnO_3$ shows a Jahn–Teller distortion that causes a charge ordered (CO) state at T_{CO}. At lower temperatures (≤ 175 K), d electrons of Mn ions show antiferromagnetic (AF) spin ordering, resulting in an AF insulator [54]. The magnetic state for $T_N < T < T_{CO}$ is paramagnetic. It has been reported that the CO state of AF insulating $Pr_{1-x}Ca_xMnO_3$ collapses to a charge disordered state when an external stimulus such as a magnetic field [55,56], light [57], x-rays [58], high pressure [59], or an electric field is applied; this manifests as an insulator-metal transition. The canted AF insulating (CAFI) state also shows up below the AFI state in the COI phase for $0.3 < x < 0.4$. A paramagnetic insulator (PI) phase is present at high temperatures. Orthorhombic $Pr_{0.5}Ca_{0.5}MnO_3$ is the charge ordered manganite compound which has been studied in this thesis along with YBCO. It may be noted that the mixed-valent manganites are typically considered to be disordered compounds, where Mn^{3+} and Mn^{4+} ions are randomly distributed in the lattice. However, under certain conditions of temperature and doping, and specially when Mn^{3+} and Mn^{4+} cations are present in equal amounts, these cations order coherently over long distances to form a charge-ordered (CO) lattice. $Pr_{0.5}Ca_{0.5}MnO_3$ has Pbnm space group with lattice parameters of a = 5.3949(1) Å, b = 5.4042(2) Å, c = 7.6064(2) Å at room temperature [48, 60]. In $Pr_{0.5}Ca_{0.5}MnO_3$, the charge and orbital order develops in the paramagnetic phase below T_{CO} = 250 K [60]. The ordering process is accomplished at T_N = 170 K [60] where the charge-exchange (CE) type antiferromagnetism sets in (see figure 1.9) [61]. By applying a magnetic field, the combined AF/CO state can undergo a first-order phase transition (called the melting of the charge order) and transform to a FM state. The melting fields are quite high, around 27 T at low temperatures [62]. There are a number of reports that the charge order in $Pr_{0.5}Ca_{0.5}MnO_3$ thin films can be destroyed by the application of magnetic field [63], electric field [58], substrate induced strain [64] or exposure to x-ray photons [58] resulting in FM metallic phase.

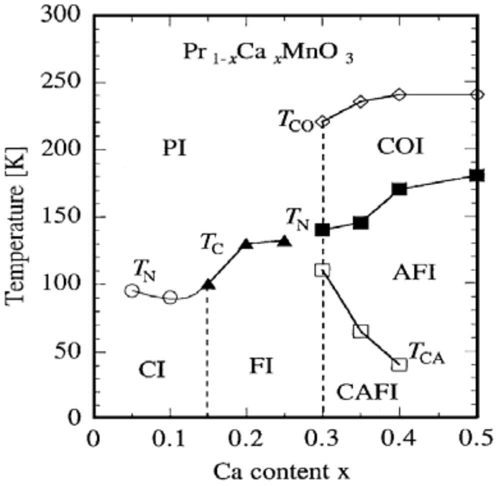

Fig. 1.9. *Phase diagram of $Pr_{1-x}Ca_xMnO_3$. PI, FI, AFI, COI and CAFI denote paramagnetic insulator, ferromagnetic insulator, antiferromagnetic insulator, charge order insulator and canted AF insulator states respectively [65].*

1.9 Basic properties of $YBa_2Cu_3O_{7-\delta}$:

Yttrium barium copper oxide is a crystalline chemical compound with the formula $YBa_2Cu_3O_{7-\delta}$ (YBCO). As a high-temperature superconductor material, YBCO has achieved prominence because it was the first material to show superconductivity above the boiling point (77 K) of liquid nitrogen. The high transition temperature (~92 K) of this material makes it a good candidate for applications because liquid nitrogen is a cheap and easy-to-handle coolant compared to liquid helium. YBCO is a perovskite cuprate with a quasi-two-dimensional structure. The superconductivity in this material is determined by the electrons moving within the copper-oxide (CuO_2) layers. The other layers act to stabilize the structure and provide electrons/holes into the copper-oxide layers. The crystal structure of YBCO [66, 67] is shown in Figure 1.10 .

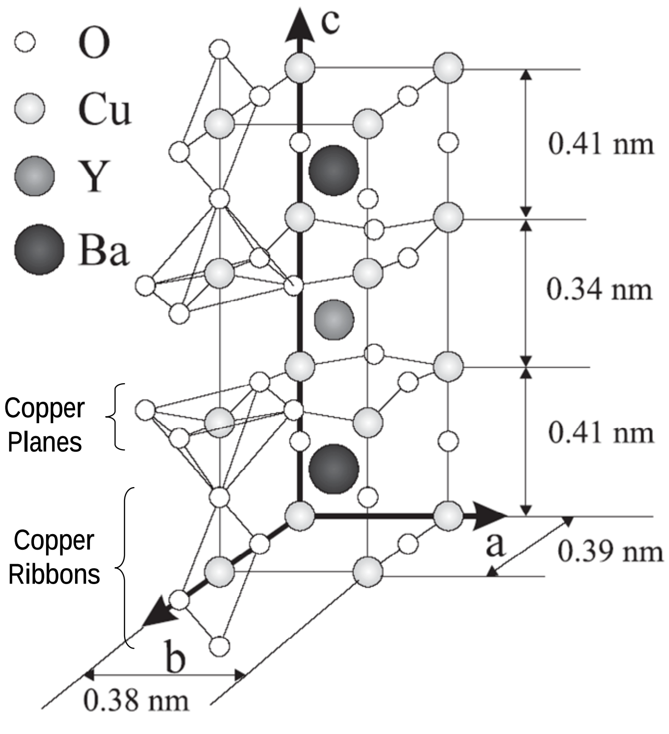

Fig. 1.10. *Crystal structure of YBCO .*

YBCO crystal has a layered perovskite structure with oxygen vacancies at specific lattice sites ($\delta = 1$). Each layer of YBCO unit cell has the boundary which is defined by the planar square CuO_4 units, called ribbons, sharing 4 vertices. The CuO_2 planes, which are known to be important for superconductivity, are perpendicular to these CuO_4 ribbons. The yttrium atoms are located between the CuO_2 planes, while the barium atoms are located between the CuO_4 ribbons and the CuO_2 planes. The YBCO has an orthorhombic structure with the crystal lattice parameters a =0.39 nm, b =0.38 nm, and c =1.16 nm as shown in figure 1.10. The superconducting gap, shown in the figure 1.11, vanishes along the [110] directions in the k_x-k_y plane in the reciprocal space i.e. along the directions defined by $k_x = \pm k_y$ [68] directions of the Fermi surface, giving rise to the nodes, while the “+”and “-”are the signs of the order parameter in the momentum k-space.

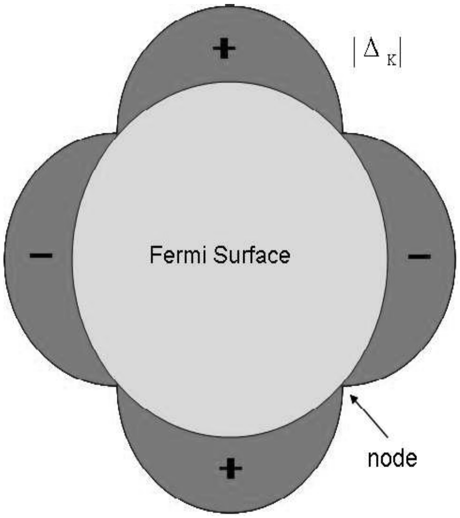

Figure 1.11: *The d-wave pairing symmetry in YBCO.*

The low-energy superconducting properties of YBCO are dominated by single particle excitations near these nodes. Furthermore, the d-wave symmetry of the gap shows that the superconductivity is of an unconventional type with significant contributions to electron pairing from interactions other than the conventional electron-phonon interaction, which is known to result in a s-wave superconductivity [69]. The possible mechanisms responsible for superconductivity in YBCO are not yet clear, with several theories actively discussing the importance of various specific features for sustaining superconductivity at such relatively high temperatures. A summary of the properties of the optimally doped YBCO ($YBa_2Cu_3O_{6.93}$) is presented in Table 1.1 including the superconducting transition temperature T_c, coherence length ξ, penetration depth λ, the resistivity ρ in the normal state (at 100 and 290 K) and so on, taken from Ref. [70].

Properties	Symbol	Values along the a-b plane	Values along the c direction	General values %
Critical Temperature	T_c			92K
Resistivity at 100K	$\rho(100K)$	70 - 250 $\mu\Omega$cm	9 - 18 mΩcm	
Resistivity at 290K	$\rho(290K)$	180 - 550 $\mu\Omega$cm	11 - 21 mΩcm	
Critical density of current at 77K	J_c (77K)			5×10^6 A/cm^2
Critical density of current at 4.2K	J_c (4.2K)			6×10^7 A/cm^2
Penetration Depth	λ	26 - 260 nm	125 - 550 nm	
Coherence Length	ξ_s	1.2 - 4.3 nm	0.2 - 0.8 nm	
Lower Critical Field	B_{c1}	5 - 18 mT	53 - 520 mT	
Upper Critical Field	B_{c2}	110 - 240 T	29 - 40 T	B_{c2}: 120 - 200 T
Energy Gap	$2\Delta_0$			30 meV

Table 1.1: *Summary of the properties of $YBa_2Cu_3O_{6.93}$ [70].*

The parent compound (oxygen content $7 - \delta < 0.25$) of YBCO is an antiferromagnetic Mott insulator. At low hole doping, it shows antiferromagnetic (AF) long range order and insulator behavior in the transport properties. This long range AF order can be destroyed and superconductivity emerges when the parent Mott insulator is doped with a certain level of hole doping. Furthermore, the superconducting transition temperature T_c changes with doping. The temperature vs hole doping [71] phase diagram of YBCO is schematically represented in Figure 1.12.

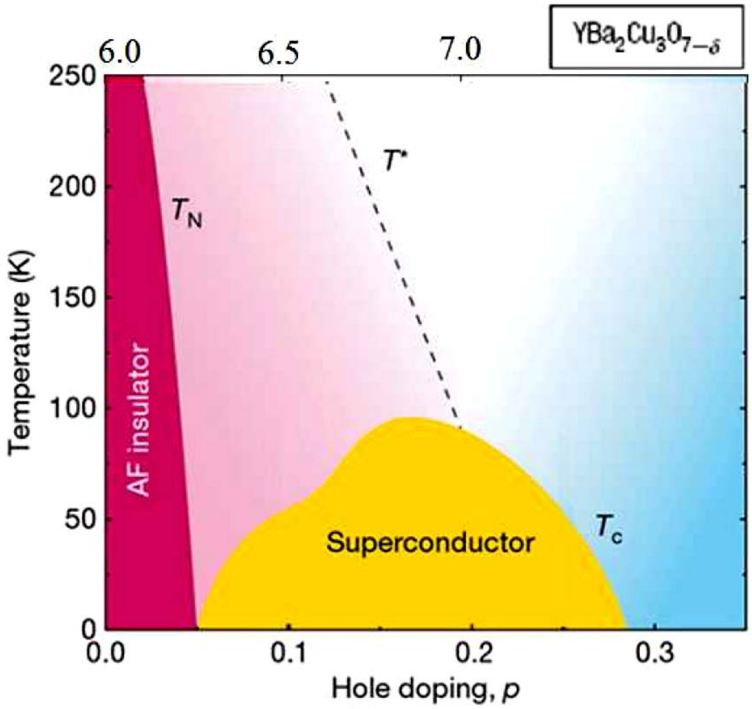

Fig. 1.12. *Schematic phase diagram of temperature vs. hole doping in YBCO and corresponding oxygen content (top axis). The antiferromagnetic (T_N) and superconducting (T_C) transition temperature and the pseudogap crossover temperature T^* in YBCO are also indicated in this diagram [71].*

The Neel temperature T_N is the temperature at which the transition from paramagnetism to antiferromagnetism takes place while T^* is the temperature below which a pseudogap is observed. The pseudogap represents a region of depleted density of states near the Fermi surface in the normal state of the cuprates [72].

1.10 Vortex Matter and Flux Flow Resistance :

1.10.1 The Concept of Pinning Force:

In the mixed state of type II superconductors like YBCO, when a magnetic field B is applied, the magnetic flux penetrates the superconductor in the form of vortices. According to the Abrikosov vortex lattice model, the vortices interact with each other and arrange themselves in a regular structure known as the vortex lattice [73]. The vortex matter can also interact with the defects present the material, which can pin the vortices. However, passage of transport current gives rise to a Lorentz force F_L on the vortices which drives the flux vortices and produces dissipation. The Lorentz force on each vortex per unit length is given by

$$F_L = J\ \varphi_0$$

Here, φ_0 is the magnetic flux quantum and J is the current density. When the Lorentz force F_L exceeds the pinning force F_P , the flux lines can move accompanied by a dissipation of energy. When the applied force density is equal to F_P, the corresponding current density is defined as the critical current density, J_C, giving:

$$F_P = J_C\ B$$

The above definition can be used to calculate the pinning force. In studies on superconductors, various types of dynamics of vortices are important during the measurement of transport J_C. A typical variation of the voltage V as a function of applied current I (alternatively electric field versus current density J) is schematically illustrated in figure 1.13 to demonstrate the presence of different types of vortex flow dynamics during the measurement of transport J_C. From the figure, it is seen that the three different parts of the I-V curve are “thermally activated flux flow (TAFF)” in the low current end, flux flow in the high current region and “flux creep in the transition region between the two. While the latter two terms were commonly used in the earlier research on low T_c superconductors, TAFF mechanism was specially invoked to describe a new aspect of vortex dynamics in high temperature superconductors which becomes relevant on account of the relatively low pinning potential and high operating temperatures [74].

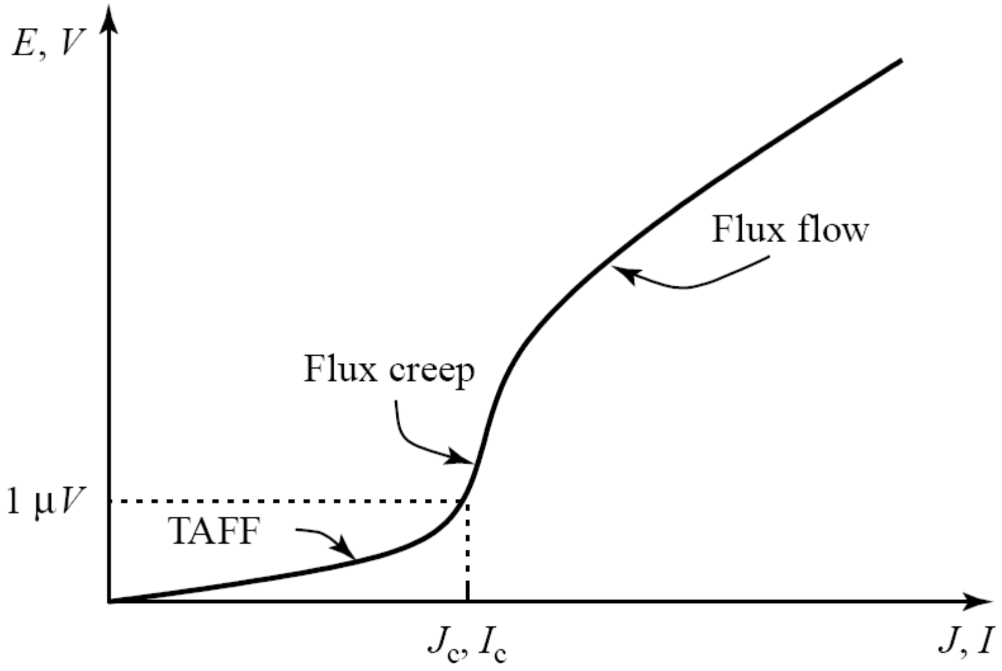

Fig. 1.13. *A schematic sketch of the variation of the voltage(V) with applied current (I) by transport measurements in high T_c superconductors in the presence of an external magnetic field illustrating different types of vortex dynamics which are relevant in different regions of the I-V characteristic[74].*

1.10.2 Flux flow:

If the superconductor is free from pinning sites or if the Lorentz force is so strong that it exceeds the pinning force, the velocity of the vortex, υ_L, is limited by the viscous drag exerted by the surrounding medium. The movement of the flux vortices is then called flux flow, giving,

$$\eta\upsilon_L = J\,\varphi_0$$

where η is the viscosity coefficient of the vortex matter. The vortices move in a direction which is perpendicular to the current and an electric field E_0 is induced in the direction of the applied current J, that is

$$E_0 = \upsilon_L B$$

With a flux-flow resistivity ρ_f as,

$$\rho_f = dE_0/dJ = \varphi_0 B/\eta$$

So, the flux-flow resistivity ρ_f can be determined from the slope of E_0 vs. J curve. It is found that ρ_f is independent of the critical current of the sample, or the pinning force Fp [75].

1.10.3 Flux creep:

Flux creep occurs due to thermal energy which may randomly induce a vortex to escape from its potential minimum at the pinned position. Depinned vortices will move or creep in order to relax the critical state field gradient. The theory of flux creep was put forward by Anderson and Kim [76]. They suggested that all flux lines within a distance λ would constitute a correlated flux bundle and these correlated flux lines move simultaneously.

1.10.4 TAFF:

In thermally activated flux flow (TAFF) regime, the flux vortex dynamics is not primarily determined by pinning but the vortex motion will resemble more closely a steady flow of vortices. A linear flux flow resistance has been observed in this regime which is mainly dominated at low current densities in a large range of temperatures below the superconducting transition temperature. The relevance of the TAFF diffusive dynamics for this regime was discussed by Kes and coworkers [77].

1.11 Ferromagnet/superconductor interaction in thin film form:

1.11.1 Introduction:

Thin layers can have considerably different physical properties compared to the corresponding bulk materials. This change in properties could be on account of several reasons. One possibility is the increased importance of the surfaces and interfaces which influence the physical properties. In the former case, a reconstruction of the surface or a chemical change due to contact with air can induce a change in properties, while in the latter case, a lattice mismatch with the material of an adjacent layer can lead to strain induced effects [78]. A second possibility is that the proximity to another material with a different or even competing order (superconducting or magnetic) gives rise to new electronic or magnetic properties due to the mutual interaction of the two orders [79,80]. Proximity effects can therefore be of structural or of electronic or magnetic in origin. The strain induced proximity effects are often intentionally reduced to a minimum in order to perform detailed experimental investigations on the proximity effects, which are electronic or magnetic in origin. This is achieved by using materials with a minimal lateral lattice mismatch which allows for epitaxial growth of the heterostructures and a tailoring of atomically flat interfaces. Technical advances in the past years have made the growth of such heteroepitaxial heterostructures possible as is shown in the prominent example of a high conductivity observed at the interfaces between two insulators [79,80]. Besides the intentional reduction of the structural proximity effects, one can investigate layers of materials with suitable physical properties, especially, where the electronic and magnetic orders of the individual layers are antagonistic or competing. Ferromagnet / superconductor heterostructures are therefore promising candidates for such investigations because the electron spins couple parallel in ferromagnets and antiparallel in the Cooper pairs of superconductors.

According to the BCS theory, the superconducting ground state consists of Cooper pairs with equal and opposite momentum and spin. At T>0, there is a nonzero probability for the Cooper pairs to break into individual quasiparticles using the available thermal energy kT. In the steady state equilibrium, the rate of breaking of Cooper pairs is exactly equal to the quasiparticle recombination rate. Non-equilibrium can, however, be induced by the addition of energy. For instance, the change in the energy distribution of its quasiparticle population can alter the characteristics of the superconducting state [81]. In a superconductor in equillibrium, the quasiparticle distribution function is described by the Fermi-Dirac distribution function:

$$f_k(E) = \frac{1}{1+\exp\dfrac{E-q'}{K_B T_e}} \qquad \text{------------(1.11.2.1)}$$

where T_e is the electronic temperature and q' is the effective chemical potential. Combining the quasiparticle probability distribution function with the BCS energy gap [82], it has been shown that the quasiparticle distribution function directly affects the energy gap:

$$\ln(\frac{\Delta(0)}{\Delta}) = \int_0^\infty \frac{N(E,\Delta) f(E,T)}{E} dE \qquad \text{-----------(1.11.2.2)}$$

Where N(E,Δ) denotes that the density of states of the superconductor, which is dependent on the energy E and the energy gap Δ.

The presence of excess quasiparticles in a superconductor could not only result in a suppression of the energy gap but also reduce the critical current of the film. A sufficiently high density can even suppress the order parameter to zero. The exact energy distribution of quasiparticles and phonons, however, is complicated because it depends on several parameters, such as the energy distribution of quasiparticle excitation rates, the phonon-to-quasiparticle and quasiparticle-to-phonon transition rates, phonon lifetimes, and the elastic scattering rates for quasiparticles and phonons. When the perturbing source is removed from the system, the non-equilibrium state relaxes. Excited quasiparticles can decay through phonon emission into lower energy states. The excess quasiparticles will recombine and while doing so, emit phonons of energies greater than 2Δ, which can cause further pair breaking effects. These phonons will eventually escape through the surface, such as into the insulator substrate, without reabsorption, or thermalize within the superconductor. Phonons can also be reabsorbed by quasiparticles, but only at high quasiparticle densities, eg. at $T \simeq T_c$.

Quasiparticle spin injection into superconductors can be of two types: the first one is the ordinary quasiparticle injection where the injector can be a normal metal or a superconductor, while the second one is the spin polarized quasiparticle injection; the spin polarized quasiparticle injection involves the use of a magnetic injector layer.

1.11.2 Ordinary quasi particle injection:

This section discusses, from a different perspective, non-equilibrium induced in the superconductor consequent to current injection and the presence of excess quasiparticles. Although the equations used here to explain the effects of quasiparticle injection [83] were derived and applied for conventional s-wave superconductors, they also serve to provide an understanding of the spin injection in HTS materials with a d-wave symmetry for the order parameter.

Consider current injection into a normal metal/superconductor (N/S) junction. Excess quasiparticle density (number of quasiparticles (N) per volume) is proportional to the injected current:

$$\delta n_{qp} = \frac{J_{inj}\tau_{eff}}{et} \qquad \text{------------(1.11.3.1)}$$

where δn_{qp} represents the excess quasiparticle density, J_{inj} is the injected current density, τ_{eff} is the effective quasiparticle recombination time, e represents the electron charge, and t is the thickness of the perturbed region.

The excess quasiparticles can cause uniform perturbation of equilibrium superconductivity if the film is sufficiently thin, i.e. if the film is thinner than the quasiparticle recombination length in the superconductor, which is defined by,

$$\delta_R \sim \sqrt{D_S}\,\tau_{eff} \qquad \text{------------(1.11.3.2)}$$

where D_S is the carrier diffusion constant. For a thick film, the superconductivity is only perturbed near the injection source to a depth of δ_R.

The superconducting order parameter decreases monotonically with increasing quasiparticle density, n_{qp}, in an S/N junction as described by the equation,

$$\frac{\Delta(n_{qp})}{\Delta(0)} \cong 1 - \frac{2n_{qp}}{4N(0)\Delta(0)} \qquad \text{----------(1.11.3.3)}$$

where $\Delta(n_{qp})$ is the perturbed energy gap, $\Delta(0)$ is zero temperature energy gap and N(0) is the single-spin density of states in the superconductor.

Combining the two equations, we get,

$$\frac{d\Delta}{dJ_{inj}} \cong -\left(\frac{\tau_{eff}}{2eN(0)t}\right) \qquad \text{-----------(1.11.3.4)}$$

where t is the thickness of the superconducting film. The above equation shows that the superconducting energy gap in a thin film decreases with increase in the injection current which, in turn, decreases the T_c of the superconductor. Since τ_{eff} has a large value at low temperatures, the rate of suppression of Δ with J_{inj} increases. τ_{eff} is also expected to increase slightly as T_c is approached but these effects are relatively small [84].

1.11.3 Spin-polarized quasiparticle injection:

Spin-polarized current injection causes pair breaking in superconductors by two different mechanisms; one is by raising the effective temperature in the presence of a high injection rate (present also in case of ordinary quasiparticle injection) which weakens the pairing, and the second is through the exchange interaction which is responsible for spin-flip scattering [85].

Spin injection is achieved by passing a current from a ferromagnet into a superconductor. Electrons are spin polarized in the ferromagnet due to the splitting of the density of states corresponding to the two spin orientations. This polarization decays monotonically with distance away from the interface. Spins can relax either through exchange coupling with other electrons in the vicinity of magnetic atoms or via spin-orbit coupling to impurity atoms or defects. In the absence of such spin flip processes, however, the orientation of the carriers' spins may be very long-lived, although the carriers may undergo numerous scattering events [86].

It may be noted that near T_c, an injected carrier recombines rapidly to form a Cooper pair regardless of its spin due to a high availability of thermally excited quasiparticles of both the spin orientations. At very low temperatures, however, the thermal quasiparticle density becomes negligible in the s-wave and very small in d-wave superconductor, and is given by the equation [87],

$$n_{qp}(t) \cong 4N(0)\Delta(0)\left(\frac{\pi\Delta(T)K_B T}{2\Delta(0)^2}\right)^{1/2} \exp-\frac{\Delta(T)}{K_B T} \qquad \text{-----------(1.11.4.1)}$$

Thus, well below T_c, there is a larger perturbation of the superconducting order parameter due to spin-polarized injection compared to the ordinary quasiparticle injection. Hence the amount of suppression of the order parameter due to spin-induced non-equilibrium effects is dependent on temperature.

It is important to note that although it is true that the effective recombination time due to spin polarized injection increases at low temperatures, and could result in a larger suppression of the order parameter, the superconducting energy gap also increases with decreasing temperature. This increase in order parameter at lower temperatures is thus in direct competition with the increasing value of τ_{sf} and the consequent spin-induced non-equilibrium. Hence, taking advantage of the lower energy gap at temperatures close to T_c, most investigations of spin injection into HTS have been performed at relatively higher temperatures (ie. ~50-90K).

1.11.4 Proximity effects:

When the superconductor is in contact with a non-superconducting material, such that the interfacial resistance is low, Cooper pairs will 'leak' into the non-superconducting material and extend the superconducting properties into the non-superconducting layer over a characteristic length from the interface. This effect is known as proximity effect and has the effect of reducing the number of Cooper pairs in the superconductor near the interface.

For proximity effects at the S/N interface, the mean free path of the electrons in the normal metal, l_N , determines the form of the coherence length in the normal metal, ξ_N . In the clean limit when the impurity level is low, where $l_N > \xi_N$, there is an exponential decay of the superconducting order parameter over the length ξ_N inside the normal metal, given by,

$$\xi_N = \frac{\hbar v_{F_N}}{2\pi K_B T} \qquad \text{------------ (1.11.5.1)}$$

where v_{FN} is the Fermi velocity in the normal metal, K_B is the Boltzmann constant and T is the temperature. In the dirty limit, where $l_N < \xi_N$, the coherence length becomes a function of the l_N ,as shown,

$$\xi_N = \sqrt{\frac{\hbar v_F l_N}{6\pi K_B T}} \qquad \text{------------(1.11.5.2)}$$

The suppression of the superconducting order parameter in the S layer near the boundary leads to a reduction of the superconducting transition temperature T_c. Hauser et al [88] showed that ferromagnetic films grown in contact with superconducting samples suppress the superconducting transition temperature to a much greater extent compared to the interfacial contact with a normal metal. The superconducting order parameter in F/S multilayer is suppressed near the F/S interfaces due to pair breaking effects caused by interactions between the aligned spins in the ferromagnet and the singlet Cooper pairs in the superconductor [89]. Matthias et al [90] investigated the interaction between the superconducting electrons and the magnetic moments, which interact with electrons via the exchange interaction. The exchange field in the ferromagnet will tend to align the spins of the electrons in Cooper pairs in the same direction leading to a weakening of spin-singlet Cooper pairs. The uniform exchange field due to the aligned spins in the ferromagnet will interact with the superconducting electrons. This interaction will cause a Zeeman splitting of the electronic energy levels. If the Zeeman energy is larger than the superconducting energy gap, superconductivity could be suppressed. We now briefly describe a few additional concepts related to proximity effects in Ferromagnet/superconductor heterostructures:

1.11.5 FFLO-State:

P. Fulde, R.A. Ferrell, A.I. Larkin and Y.N. Ovchinnikov presented a theory for a superconductor in the presence of a strong, spatially homogeneous magnetic exchange field h [91,92]. Their model is based on the BCS-theory [11], where the electrons form so-called Cooper pairs. The pairs form in the spin singlet state, and consist of two electrons with equal energy E_F and opposite momenta ($k_{F\uparrow}$ and $-k_{F\downarrow}$). Thus, the total momentum of the Cooper pair vanishes ($k_{Cooper} = k_{F\uparrow} + -k_{F\downarrow} = 0$). The presence of a ferromagnetic exchange field h gives rise to a Zeeman splitting ΔE_{ex} of the energies of the spin down and spin up electron states. When the Cooper pair enters the ferromagnet, its properties are modified: The electrons still have the same energy E_F, but the momentum of the spin up electron is reduced by $\Delta E_{ex}/\hbar v_F$, while that of the spin down electron is increased by $\Delta E_{ex}/\hbar v_F$ where v_F is the Fermi velocity. Under these circumstances, the Cooper pairs acquire a finite non-zero momentum $k_{Cooper} = 2\Delta E_{ex}/\hbar v_F$. Due to this non-zero momentum, the superconducting order parameter has a spatially oscillatory character on a length scale of $2\pi/k_{Cooper}$. Therefore, spatially inhomogeneous superconducting state may be expected to be stabilized relative to uniform superconducting state in the vicinity of ferromagnet / superconductor interfaces.

1.11.6 Oscillating T_{sc} :

Z. Radovi´c et al. predicted an oscillatory dependence of the superconducting transition temperature T_{SC} on the ferromagnet layer thickness d_{FM} [93]. Assuming both the ferromagnet and the superconductor to be in the dirty limit (i. e. a small mean free path and therefore nearly isotropic movement of the electrons), they used Usadel's dirty limit version of the quasiclassical theory of superconductivity [13]. In that case, the characteristic length scale over which the superconducting order parameter decays into the ferromagnet is given by

$$\xi_{FM} = \sqrt{\frac{4\hbar D_{FM}}{\Delta E_{ex}}} \qquad \text{-------------(1.11.7.1)}$$

where D_{FM} is the diffusion coefficient in the ferromagnet and ΔE_{ex} the exchange energy of the ferromagnet (Zeeman splitting of the spin up and spin down bands due to the magnetic exchange field h). Since the exchange energy favours one of the spin orientations, it acts as a pair breaker for the spin singlet Cooper pairs and reduces the value of ξ_{FM}. In a normal metal, where there is no such exchange energy, the corresponding length scale over which the superconducting order parameter decays is

$$\xi_N = \sqrt{\frac{\hbar D_N}{2\pi K_B T}} \qquad \text{--------------(1.11.7.2)}$$

where D_N is the diffusion coefficient in the normal metal.

In the calculations of Z. Radovic et al., the superconducting order parameter is also assumed to be reduced on the superconductor side of the interface. This characteristic length scale for a bulk superconductor is given by

$$\xi_{SCO} = \sqrt{\frac{\hbar D_{SC}}{2\pi K_B T_{SCO}}} \qquad \text{-------------(1.11.7.3)}$$

where D_{SC} is the diffusion coefficient in the superconductor and T_{SCO} is the superconducting transition temperature of the bulk superconductor. Since the transition temperature of a superconductor becomes reduced in a thin layer placed in proximity to a ferromagnet, Z. Radovi´c et al. use a corresponding length scale ξsc which depends on the reduced transition temperature T_{SC}^{red} :

$$\xi_{SC} = \sqrt{\frac{\hbar D_{SC}}{2\pi K_B T_{SC}^{red}}} \qquad \text{------------(1.11.7.4)}$$

The value of ξ_{SC} is thus larger than the one of ξ_{SCO}. It gives a lower limit below which no superconductivity occurs: T_{SC}^{red} vanishes if the thickness of the superconductor d_{SC} is smaller than twice the length ξ_{SC} over which the superconducting order parameter changes ($d_{SC} < 2\xi_{SC}$). In the opposite case, T_{SC}^{red} remains finite and non-zero.

If T_{SC}^{red} is finite and the ferromagnetic layer thickness is of the same order as the coherence length associated with the superconducting order parameter in the ferromagnetic layer ($d_{FM}/\xi_{FM} \approx 1$), an oscillatory behaviour of T_{SC}^{red} is expected in superconductor / ferromagnet / superconductor heterostructures as a function of d_{FM}. If $d_{FM} < \xi_{FM}$, the phase of the superconducting order parameter remains the same in the two superconducting layers. In this limit, the exchange energy ΔE_{ex} acting on the superconductor increases with increasing d_{FM}. Therefore T_{SC}^{red} decreases with increasing d_{FM}. If d_{FM} is about the same as ξ_{FM}, it becomes favourable for the superconducting order parameter to introduce a π-phase shift between the phases of the two superconductors. This reduces the pair-breaking effect of the exchange energy ΔE_{ex} on the superconducting order parameter. Therefore T_{SC}^{red} is enhanced even though the thickness of the ferromagnetic layer is increased. With further increase in d_{FM}, T_{SC}^{red} reduces again, as the phase of the superconducting order parameter changes over a length scale of ξ_{FM}. This oscillatory behaviour of T_{SC}^{red} as a function of d_{FM} has been confirmed in several experiments on ferromagnet / superconductor heterostructures based on conventional, non-oxide materials [94-96].

1.11.7 Inverse Proximity Effect:

F.S. Bergeret, A.F. Volkov and K.B. Efetov observed a high conductance across contacts between metallic ferromagnets placed in proximity to a superconductor in the superconducting state [97] with a spin-triplet contribution to the superconducting order parameter. They assumed a small value of the anomalous quasiclassical Green's function (low interface transparency) in order to linearise the Usadel's equations. They showed that an inhomogeneity in the magnetization at an interface can induce such a triplet component of the superconducting order parameter that corresponds to Cooper pairs with parallel electron spins [97-99]. The penetration depth of this triplet component into the ferromagnetic layer is eventually much larger than that of the singlet component ξ_{FM}:

$$\xi_{FM}^{\uparrow\uparrow} = \sqrt{\frac{\hbar D_{FM}}{2\pi K_B T}} > \sqrt{\frac{4\hbar D_{FM}}{\Delta E_{ex}}} = \xi_{FM}{}^{\uparrow\downarrow} \qquad \text{-------------(1.11.8.1)}$$

The length $\xi_{FM}^{\uparrow\uparrow}$ is in fact of the same order as the penetration depth of the singlet component into a normal metal (see Equation 11). Following the idea of a triplet component of the superconducting order parameter, they calculated the influence of the conduction electrons on the magnetization of the ferromagnet and on the magnetization induced in the superconductor. They used a simple mean field approximation model [99] where they assumed the ferromagnetic exchange energy ΔE_{ex} to be smaller than the Fermi energy and assumed a low interface transparency. They concluded that the magnetization in the ferromagnet can be reduced and that a magnetic moment aligned antiparallel to the one in the ferromagnet can be induced in the superconductor over the length scale of the coherence length ξ_{SC} of the superconductor [97,99]. In an extremely simplified picture, one can imagine Cooper pair spin singlets, of which one of the electrons penetrates into the ferromagnetic layer, while the second one is more localised in the superconductor. The electron in the ferromagnet will align its spin along the local magnetic field. Subsequently, the spin of the second electron has to align antiparallel in order to sustain the singlet state of the Cooper pair. F.S. Bergeret, A.F. Volkov and K.B.

Efetov called this effect the inverse proximity effect because there is a magnetic moment induced in the superconductor which is aligned antiparallel to the ferromagnetic moment [97].

1.11.8 Recent trend in the research of Ferromagnet/superconductor multilayers:

In recent times, there has been an extensive research into the behavior of Ferromagnet / Superconductor multilayer systems involving metallic thin films. However, the focus of these investigations has shifted to a study of the interaction between ferromagnetism and superconductivity in oxide systems. This is due to a reawakening of the interest in the study of spin polarized quasiparticle injection into high-temperature superconductors such as $YBa_2Cu_3O_7$ and the potential applications of the associated effects in the context of spintronics. There is also an active interest in understanding the F/S interaction in layered intrinsic superlattices. The fundamental difference is that in the metallic systems, the short-range spin diffusion length of several nm will confine the interaction effects to regions close to the interface. However, the relevant length scales in oxides are estimated to be longer [89].

In layered F/S systems, the interplay between superconductivity and ferromagnetism can be studied in a controlled manner, for instance, by changing the layer thicknesses, by changing the relative strengths of the two competing order parameters; indeed, by a proper choice of materials, these multilayer structures offer an opportunity to study these two antagonistic phenomena.

1.12 Outline of the thesis:

This thesis focuses on the experimental investigations that examine the influence of charge order melting of PCMO on YBCO. The CO melting is achieved by application of current, magnetic field and substrate induced strain. The thesis is divided into seven chapters, and the content of each chapter is briefly summarized below.

After an introduction to the physics of manganites and high transition temperature superconductors and their interface-phenomena, chapter-2 describes the details of experimental techniques starting with the preparation of superconducting YBCO and charge ordered insulating PCMO compound by solid state reaction. The Pulsed Laser Deposition system, which has been extensively used for the deposition of thin films of YBCO, PCMO and their heterostructures, is discussed in detail. Chapter 2 also gives an account of the photolithography technique used for the fabrication of the microbridges with a view to measure the J_c of YBCO thin film. Other characterization techniques like X-ray diffraction (XRD), magnetoresistance measurement (MR) system are also discussed briefly in this chapter.

In chapter-3, the deposition of YBCO thin film on different substrates and their experimental characterization are described. Also the experimental study of the substrate induced strain effect on charge-ordered PCMO thin film is discussed in this chapter.

Chapter-4 investigates the proximity and spin injection effects of PCMO on the T_c of YBCO in PCMO/YBCO bilayer film deposited on LAO substrate by pulsed laser deposition technique. The experimental results are explained on the basis of the formation and growth of ferromagnetic clusters on account of charge order melting in $Pr_{0.5}Ca_{0.5}MnO_3$ due to the application of high current and magnetic fields.

In chapter-5, the studies on PCMO/YBCO bilayer film is discussed to demonstrate the possibility of controlling the superconducting properties of YBCO thin film by nucleating ferromagnetic clusters in a PCMO thin film under the influence of a suitable control variable even when the two regions are not in close proximity.

Chapter-6 describes the combined effect of current and strain induced CO melting on the superconducting properties of YBCO in PCMO/YBCO/PCMO trilayer thin film heterostructures deposited on MgO substrate.

Finally, chapter-7 summarizes the thesis and presents a few directions for possible future research.

References:

[1] W. Gerlach and O. Stern, Zeitschrift fur Physik 9, 349 (1922).

[2] A.H. Compton, Journal of the Franklin Institute 192, 145 (1921).

[3] G.E. Uhlenbeck and S. Goudsmit, Nature 117, 264 (1926).

[4] P.A.M. Dirac, Proceedings of the Royal Society of London Series A-containing Papers of a Mathematical and Physical Character 117, 610 (1928).

[5] E. Ising, Zeitschrift f¨ur Physik 31, 253 (1925).

[6] W. Heisenberg, Zeitschrift fur Physik 49, 619 (1928).

[7] J.C. Slater, Reviews of Modern Physics 25, 199 (1953).

[8] E.P. Wohlfarth, Reviews of Modern Physics 25, 211 (1953).

[9] M.B. Salamon and M. Jaime, Reviews of Modern Physics 73, 583 (2001).

[10] H.K. Onnes, Proceedings of the Koninklijke Akademie Van Wetenschappen te Amsterdam 14, 113 (1911).

[11] J. Bardeen, L.N. Cooper and J.R. Schrieffer, The Physical Review 108, 1175 (1957).

[12]P.G. De Gennes, Reviews of Modern Physics 36, 225 (1964).

[13]K.D. Usadel, Physical Review Letters 25, 507 (1970).

[14] J.G. Bednorz and K.A. M¨ uller, Zeitschrift fur Physik B: Condensed Matter 64, 189 (1986).

[15] Y. Kamihara, T. Watanabe, M. Hirano and H. Hosono, Journal of the American Chemical Society 130, 3296 (2008).

[16] X.H. Chen, T. Wu, G. Wu, R.H. Liu, H. Chen and D.F. Fang, Nature 453, 761 (2008).

[17] A.J. Drew, Ch. Niedermayer, P.J. Baker, F.L. Pratt, S.J. Blundell, T. Lancaster, R.H. Liu, G. Wu, X.H. Chen, I. Watanabe, V.K. Malik, A. Dubroka, M. R¨ossle, K.W. Kim, C. Baines and C. Bernhard, Nature Materials 8, 310 (2009).

[18] Ginzburg, V. L. Zh. Exsp. Teor. Fiz 31,201 (1956)

[19] I. Sosnin, H. Cho, V. T. Petrashwo and A. F. Volkov Phys. Rev. Lett. 96, 157002 (2006)

[20] V. Pena, Z. Sefrioui, D. Arias, C. Leon, J. Santamaria, J. L. Martinez, S. G. E. te Velthuis and A. Hoffman Phys. Rev. Lett. 94, 057002 (2005)

[21] Yang Z, Lange M, Volodin A, Szymczak R and Moshchalkov V V Nat. Mater. 3, 793 (2004)

[22] Gillijns W, Aladyshkin A Yu, Van Bael M J, Lange M and Moshchalkov Physica C 437, 73 (2006)

[23] Zhu L Y, Chen T Y and Chien C L Phys.Rev.Lett. 101, 017004 (2008)

[24] Samal D, Shivakumara C and Anil Kumar P S Phys. Rev. B 77, 094510 (2008)

[25] Sefrioui Z, Arias D, Pena V, Villegas J E, Varela M, Prieto P, Leon C, Martinez J J L and Santamaria J Phys. Rev. B 67, 214511 (2003)

[26] Sefrioui Z, Varela M, Pena V, Arias D, Leon C and Santamaria J Appl. Phys. Lett. 81, 4568 (2002)

[27] Tagirov L R Phys. Rev. Lett. 83, 2058 (1999)

[28] Moraru I C, Pratt W P Jr and Birge N O Phys. Rev. Lett. 96, 037004 (2006)

[29] Gu J Y, You C Y, Jiang J S, Pearson J, Bazaliy Ya B and Bader S D Phys.Rev.Lett. 89, 267001(2002)

[30] A. A. Golubov, M. Yu. Kupriyanov, Pis'ma Zh. Exp. Teor. Phys. 52, 1089 (1990)

[31] G. Jakob, V.V. Moshchalkov and Y. Bruynseraede, Applied Physics Letters 66, 2564 (1995).

[32] A.M. Goldman, V. Vas'ko, P. Kraus, K. Nikolaev and V.A. Larkin, Journal of Magnetism and Magnetic Materials 200, 69 (1999).

[33] Z. Sefrioui, D. Arias, V. Pena, J.E. Villegas, M. Varela, P. Prieto, C. Le´on, J.L. Martinez and J. Santamaria, Physical Review B 67, 214511 (2003).

[34] T. Holden, H.-U. Habermeier, G. Cristiani, A. Golnik, A. Boris, A. Pimenov, J. Huml´ı˘cek, O.I. Lebedev, G. Van Tendeloo, B. Keimer and C. Bernhard, Physical Review B 69, 064505 (2004).

[35] S. Jin, M. McCormack, T.H. Tiefel and R. Ramesh, Journal of Applied Physics 76, 6929 (1994).

[36] Y.Tokura Phys. Today 56, 50 (2003)

[37] F. Duan and J. Guojun, Introduction to Condensed Matter Physics,1 ed. (World Scientific Publishing Co. Pvt. Ltd., Singapore-596224, 2005), Vol. 1.

[38] H. A. *Jahn,* E. *Teller*, *Proc. Roy. Soc.* A161, 220 (1937).

[39] M.J. Thornton and M. Ziese (Eds.): LNP 569, 89 (2001)

[40] T. Ogasawara, T. Kimura, T. Ishikawa, M. Kuwata-Gonokami, and Y. Tokura Phys. Rev B 63,113105 (2001)

[41] Y.Tokura Rep. Prog. Phys. 69, 797 (2006)

[42] H. A. Karmers Physica 1, 182 (1934)

[43] P. W. Anderson, *Phys.Rev.* **79**, 350 (1950).

[44] C. Zener Phys. Rev. B 82, 403 (1951)

[45] M. Cieplak Phys. Rev. B 18, 3470 (1978)

[46] A. P. Ramirez J. Phys.: Condens. Matter 9, 8171 (1997)

[47] M. Vehara, S. Mori, C. H. Chen and S-W. Cheong Nature 399, 560(1999)

[48] Y. Imry and S. K. Ma Phys. Rev. Lett 35, 1399 (1975)

[49] Y. Tomioka, A. Asamitsu, Y. Moritomo, Y. Tokura, *J. Phys. Soc. Jap.* 64, 3626 (1995).

[50] S. R. Broadbent and J. M. Hammersley Proc. Camb. Phillos. Soc. 53, 629 (1957)

[51] S. Kirkpatrick Rev. Mod. Phys. 45, 574 (1973)

[52] E. Dagotto, T. Hotta and A. Moreo, Physics Reports 344, 1 (2001).

[53] S. Quezel-Ambrunaz, *Bull. Soc. Franc. Minér. Crist.* 91, 339 (1968).

[54] Z. Jirák, S. Krupiþka, Z. Šimša, M. Dlouhá, S. Vratislav, *J. Magn. Magn. Mat.* 53, 153 (1985).

[55] J. Barratt, M. R. Lees, G. Balakrishnan, D. McK Paul, *Appl. Phys. Lett.* 68, 424 (1996).

[56] Y. Tomioka, A. Asamitsu, Y. Moritomo, Y. Tokura, *J. Phys. Soc. Jap.* 64, 3626 (1995).

[57] M. Fiebig, K. Miyano, Y. Tomioka, Y. Tokura, *Science* **280**, 1925 (1998)

[58] V. Kiryukhin, D. Casa, J.P. Hill, B. Keimer, A. Vigliante, Y. Tomioka, Y. Tokura, *Nature* 386, 813 (1997).

[59] Y. Moritomo, H. Kuwahara, Y. Tomioka, Y. Tokura, *Phys. Rev. B* 55, 7549 (1997)

[60] Z. Jirak, F. Damay, M. Hervieu, C. Martin, B. Raveau, G. Andre, F. Bouree, *Phys. Rev. B* 61, 1181 (2000).

[61] A. Trokiner, A. Yakubovskii, S. Verkhovskii, A. Gerashenko, D. Khomskii *Phys. Rev. B* 74, 092403 (2006).

[62]] M. Tokunaga, N. Miura, Y. Tomioka, Y. Tokura, *Phys. Rev. B* 57, 5259 (1998).

[63] A. Asamitsu, Y. Tomioka, H. Kuwahara and Y. Tokura, Nature 388, 50 (1997).

[64] W. S. Tan, L. Yang, X. S. Wu, S. S. Jiang, T. L. Kam, J. Gao, J. Wang and Z. H. Wu Physica C 384,437(2003)

[65] H. Sha, F. Ye, Pengcheng Dai, J. A. Fernandez-Baca, Dalgis Mesa, J. W. Lynn, Y. Tomioka, Y. Tokura, J. Zhang, *Phys. Rev. B* 78, 052410 (2008).

[66] D. Kang, Ph.D. thesis, University of Cambridge, 1998.

[67] Paul M. Grant, Nature 407, 139 (2000).

[68] Shigeji Fujita and Salvador Goday " Theory of High Temperature Superconductivity" Kluwer academic Publishers, 2001

[69] P. Monthoux, A. V. Balatsky, and D. Pines, Phys. Rev. B 46, 14803 (1992).

[70] C. Poole, H. Farach, and R. Creswich, *Superconductivity*, 1st ed. (Academic Press Inc., London, U. K., 1995).

[71] Ruixing Liang and D. A. Bonn and W. N. Hardy, Phys. Rev. B 73, 180505 (2006).

[72] H. Kamimura, H. Ushio, S. Matsuno and T. Hamada "Theory of Copper Oxide Superconductors", Springer-Verlag Berlin Heidelberg 2005

[73] A. A. Abrikosov, Sov. Phys. JETP 5,1174 (1957)

[74] K. Fossheim and A. Sudbo " Superconductivity Physics and Application" John Wiley and Sons Ltd., 2004

[75] J. Bardeen and M. J. Stephen Phys. Rev. 140, A1197 (1965)

[76] P. W. Anderson and Y. B. Kim Rev. Mod. Phys. 36, 39 (1964)

[77] P. H. Kes, J. Aarts, J. van der Berg, C. J. van der Beek and J. A. Mydosh Supercond. Sci. Technol 1, 242 (1989)

[78] S. Lin, T. H. Tiefel, M. McCormack, H. M. U'Bryan, L.H. Chen, R. Ramesh and D. Schurig Appl. Phys. Lett. 67, 557 (1995)

[79] A. Ohtomo, D.A. Muller, H.L. Grazui and H.Y. Hwang, Nature 419, 378 (2002).

[80] A. Ohtomo and H.Y. Hwang, Nature 427, 423 (2004).

[81] M. Tinkham and J. Clarke, Phys. Rev.Letters 28, 1366 (1972).

[82] R. Moseley, Ph.D. thesis, University of Cambridge (2000).

[83] Y. Gim, A. W. Kleinsasser, and J. B. Barner, Journal of Applied Physics 90, 4063 (2001)

[84] C. W. Schneider,R.Moerman,F.J.G.Roesthuis,R.G.Wichern,G.J.Gerritsma,and H. Rogalla, Ieee Transactions on Applied Superconductivity 7, 2730 (1997).

[85] J. Y. T. Wei, Journal of Superconductivity 15, 67 (2002).

[86] G. Prinz, Physics Today April, 58 (1995).

[87] W. Eisenmenger, Nonequilibrium Superconductivity, Phonons and Kapitza Boundaries (Plenum, New York, 1981).

[88] J. J. Hauser, H. Theuerer, and N. R. Werthamer, Phys. Rev. 142, 118 (1966).

[89] H. U. Habermeier and G. Cristiani, Ieee Transactions on Applied Superconductivity 13, 2842 (2003).

[90] B. Matthias, H. Suhl, and E. Corenzwitz, Phys. Rev.Letters 1, 444 (1958).

[91] P. Fulde and R.A. Ferrell, Physical Review 135, A550 (1964).

[92] A. I. Larkin and Y.N. Ovchinnikov, Soviet Physics Journal for Experimental and Theoretical Physics 20, 762 (1965).

[93] Z. Radovi´c, M. Ledvij, L. Dobrosavljevi´c-Gurji´c, A.I. Buzdin and J.R. Clem, Physical Review B 44, 759 (1991).

[94]Th. Muhge, N.N. Garif'yanov, Yu.V. Goryunov, G.G. Khaliullin, L.R. Tagirov, K. Westerholt, I.A. Garifullin and H. Zabel, Physical Review Letters 77, 1857 (1996).

[95] L.V. Mercaldo, C. Attanasio, C. Coccorese, L. Maritato, S.L. Prischepa and M. Salvato, Physical Review B 53, 14040 (1996).

[96] J.S. Jiang, D. Davidovi´c, D.H. Reich and C.L. Chien, Physical Review B 54, 6119 (1996).

[97] F.S. Bergeret, A.F. Volkov and K.B. Efetov, Reviews of Modern Physics 77, 1321 (2005).

[98] F.S. Bergeret, A.F. Volkov and K.B. Efetov, Physical Review Letters 86, 4096 (2001).

[99] F.S. Bergeret, A.F. Volkov and K.B. Efetov, Physical Review B 69, 174504 (2004).

Chapter 2

Details of Experimental Techniques

Pulsed laser deposition is one of the most often employed method for the deposition of thin oxide films. Although the underlying physics of pulsed laser deposition is very complex, this technique offers a convenient way to produce thin films [1,2]. The major progress with this film growth technique has come hand in hand with the exploration of the high-temperature superconductors (mainly the cuprates). As compared to the other deposition techniques (i.e. molecular beam epitaxy, magnetron sputtering and metal organic chemical vapour deposition), the main advantage of PLD is the flexibility and the possibility to obtain high quality stoichiometric multi-component thin films without any requirements for wet processing (as MOCVD) or ultra-high vacuum (as MBE). However, a disadvantage of PLD is that the technique is not suitable for large area depositions; it is preferably used for small substrates ($\leq$ 1cm).

2.1 Pulsed Laser Deposition

The PLD system consists of a target holder, a substrate stage coupled to heater, housed in a vacuum chamber. A high powered laser is used as an external energy source to vaporize materials (from the targets) which will be deposited on the substrate, forming the thin films. The laser beam is focused onto the target using a system of optics producing, a rectangular beam spot, homogeneous in intensity. The vacuum chamber is usually connected to an external O_2 cylinder to get required O_2 pressure during the deposition of the film. A schematic diagram of a PLD system is shown in figure 2.1.

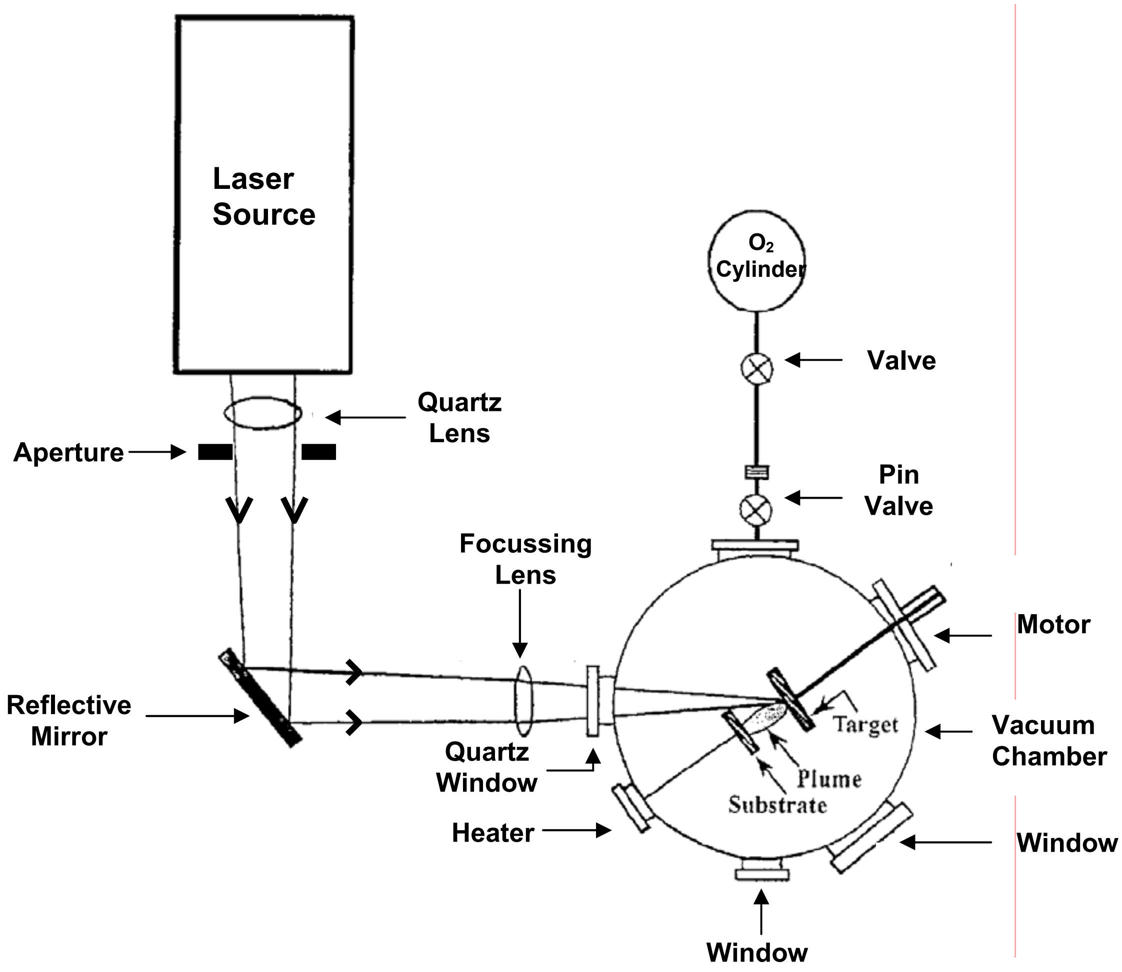

Fig. 2.1: A schematic diagram of a PLD system for depositing oxides films.

2.2 PLD film growth :

The PLD of oxide films is usually carried out in a reactive environment containing gas or gas mixtures with or without plasma excitation. KrF Excimer laser has been used in the PLD system for depositing $YBa_2Cu_3O_7/Pr_{0.5}Ca_{0.5}MnO_3$ (YCBO/PCMO) bilayer or trilayer heterostructures studied in the present thesis work. This PLD system consists of several important components which have different important parameters to consider for oxide thin film deposition. A brief description of all these important components and parameters are given below.

2.2.1 Basics of excimer Laser :

The most commonly used range of excimer laser wavelength for thin film growth by PLD lies in the UV region (195 to 508nm) between 200 to 400 nm. Most materials used for deposition exhibit strong absorption in this spectral region. Below 200nm, strong absorption by molecular oxygen prohibits the laser deposition. In addition, the optics for shorter wavelengths are more difficult to handle. The absorption co-efficients of materials tend to increase at the shorter wavelength end of this range, and thus the penetration depths into the target materials are reduced. The use of shorter wavelength lasers may be favourable, however, if thinner layers of the target need to be ablated.

An excimer laser is a gas laser which emits radiation directly in the UV range. The KrF excimer laser operating wavelength is 248nm. Excimer molecules are formed in the gaseous mixture of their component gases. Energy is pumped into the gas mixture through electric discharge excitation. The pumping creates ions and electronically excited species that react chemically and produce excimer molecules. The chemical reactions leading to the formation of the KrF Excimer molecules is briefly shown in the equations below [2]:

$Kr + e^- \rightarrow Kr^+, Kr^*, Kr^{2+}$

$F_2 + e^- \rightarrow F + F^-$

$Kr^+ + F^- + X \rightarrow KrF + X$

$Kr^{2+} + F^- \rightarrow KrF^* + Kr$

$Kr^* + F_2 \rightarrow KrF^* + F$

* denotes the electronically excited species and X represents a third body (He, Ne).

Once, the excimer (excited dimer) molecule is formed, it will decay via spontaneous emission and collisional deactivation, giving the molecule a lifetime of about 2.5ns. Thus, in order for lasing action to occur, the formation rate of the ionic and excited precursors must be fast enough to produce excimers at a rate of several 10^{23} /cm^3s^{-1} [2].

For a chosen material and a fixed laser wavelength, the laser fluence on the target has the most significant effect on the film stoichiometry, particulate size and density. The laser fluence affects the instantaneous deposition rate and the degree of supersaturation of vapour, and can be varied by varying the laser power or the laser spot size. In general, there exists a threshold laser fluence below which the particulates are barely observable. Below the threshold, deposition is in the thermal regime, similar to evaporation. Above this threshold laser fluence, the particulate number density increases rapidly with increasing fluence.

2.2.2 Laser Beam:

A homogeneous, uniform beam is essential for good quality deposition. Poor beam quality can result in non-stoichiometric films as well as undesirable droplet formation.

2.2.3 Target:

Successful depositions can be made from pressed powders, sintered pellets, cast material, single crystals, and metal foils. Porous and inhomogeneous targets yield poor quality films. High density and smooth target surfaces are desirable features of a target material in order to yield the best quality of film. To achieve uniform target erosion and consumption, the target is usually rotated during deposition. Also, the target should be flat to ensure uniform ablation.

When the laser is absorbed on the target surface, electro-magnetic energy is converted first into electronic excitation and then into thermal, chemical and even mechanical energy leading to evaporation, ablation, excitation, plasma formation and exfoliation. Targets are usually mounted on a carousel containing several other targets. This is advantageous as it allows for fabrication of in-situ multilayer structures.

2.2.4 Plume:

Evaporants from the ablated target form a plume, which consists of a mixture of energetic species including atoms, molecules, electrons, ions, clusters, micron-sized solid particulates, and molten globules. The plume is always perpendicular to the target regardless of the angle of the incident laser beam. Due to the increased collisions between the laser produced plume and the background gas, the plume expansion decreases when as the background gas pressure increases. The substrate to be coated should be placed at a distance on the edge but just within the visible part of the laser plume. The plume is usually elongated, hence, one of the disadvantages of PLD is that film deposition only takes place uniformly over a small area. We have recorded the roughness, thickness and the effective deposition area of the YBCO film for three different background O_2 pressure in the deposition chamber and also measured their superconducting transition temperatures and the data are given in table 2.1. It is seen from the table that background oxygen pressure plays an important role in achieving the higher transition temperatures of the high T_C -YBCO superconductor.

Oxygen pressure (mbar)	Rough ness (nm)	T_C (K)	Thickness of the film (nm)	Area of the deposition
0.14	5.5	82	100	High
0.33	5.5	90	90	High
0.45	7	90	75	Less

***Table 2.1**: Variation of roughness, transition temperature (T_C), thickness and the effective deposition area of the YBCO film for three different background O_2 pressure.*

2.2.5 Ambient Gas Pressure:

The use of an ambient gas during pulsed laser ablation deposition can be characterized as either passive or active. The passive use of an ambient gas is mainly to compensate for some loss of a constituent element such as oxygen or nitrogen in ceramics. Active gas is used to deliberately form particulates with a desired size or composition. The gas pressure in the deposition chamber also reduces the vapour flux. The gas molecules provide a high flux of background gas particles bombarding on the surface during deposition.

2.2.6 Heater/substrate holder:

The substrate and the target are held parallel and opposite to each other as the evaporants from the target are ejected in a highly forward-directed plume of material which is normal to the target surface. The target-substrate distance varies according to the energy delivered to the target. This distance affects the film stoichiometry and the deposition rate. When the target-substrate distance is much smaller than the plume length, there is no marked difference in particulate size. As the distance increases, the proportion of smaller particulates decreases, and a few larger particulates appear indicating agglomeration during flight. The generation of particulates produces higher roughness on the film surface. If the substrate is located far beyond the plume, the adhesion of the deposited film to the substrate is poor and also the deposition rate decreases. In our depositions, three different substrate to target distances (d, where substrate is always within the plume) have been chosen to get an idea of the relation between the distance d, roughness and film thickness. Figure 2.2 shows the plot for these three parameters.

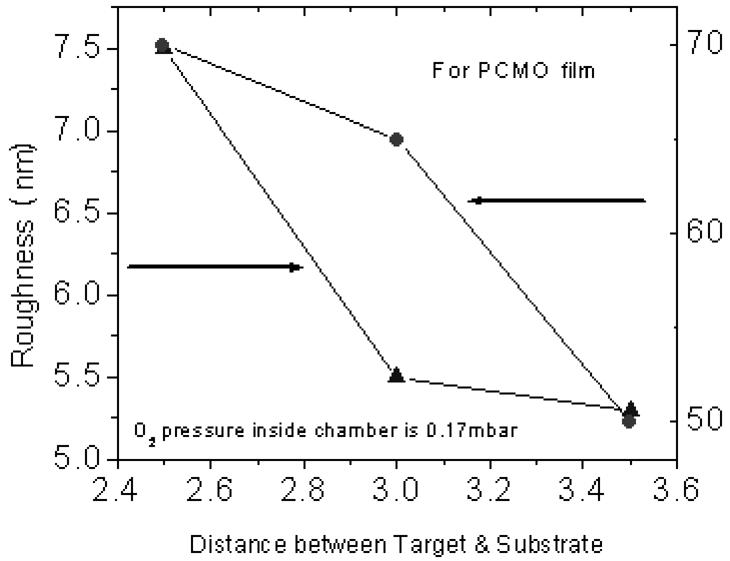

Fig. 2.2. *Plot shows the dependence of roughness and thickness on the distance between target and substrate.*

Figure 2.2 shows that an increase in the distance between target and substrate decreases the roughness of the film but simultaneously thickness of the film also decreases. Therefore, the location and orientation of the substrate relative to the target are important. Frequently, the substrate must be heated to produce good adhesion and/or epitaxy. The temperature of the substrate is important in preserving the stoichiometry of the films. The rate of crystallization also depends on the substrate temperature. A lower substrate temperature results in a faster cooling rate, which in turn leads to a lower velocity of crystallization as the adatom diffusion distance is short. Therefore the film is not completely mono-crystalline and the film composition deviates significantly from the stoichiometric one. Temperature uniformity becomes critical when the formation energy of the desired compound, or the need for epitaxy, forces the deposition temperature into a narrow band. For instance, in the case of YBCO, high substrate temperature (~ 840^0 C) favors the growth of c-axis oriented films. Smoother films can be deposited at a lower substrate temperature, but this improved morphology is at the expense of the film structure as the smoother films are typically a mixture of a and c axis oriented material as opposed to being exclusively c-axis oriented [2,3].

2.2.7 Pulse Frequency:

The laser pulse rate is especially important when the deposition is performed at elevated temperatures, and the diffusion time constants of the material atoms are comparable to the laser frequency. If the period of pulsing is much larger than the time constants for all other relevant diffusion, agglomeration, and dissociation phenomena, the pulsing is not expected to have any effect on the final microstructure. We have maintained a frequency of 5Hz/sec for all the films' deposition.

2.3 Photolithography :

Photolithography is the process of transferring geometric shapes on a mask to the surface of a desired wafer (substrate). The steps involved in the photolithographic process are wafer cleaning, photoresist application, soft baking, mask alignment, exposure and development, hard-baking, etching and photoresist removal.

2.3.1 Wafer Cleaning and Photoresist Application:

In the first step, the wafers are cleaned using soap water solution, distilled and deionized (DI) water, acetone and propanol to remove particulate matter as well as any traces of organic, ionic, and metallic impurities from the surface. After cleaning, photoresist is applied to the surface of the wafer. High-speed centrifugal whirling of desired wafers is the standard method for applying photoresist coatings. This technique, known as "Spin Coating," produces a thin uniform layer of photoresist on the wafer surface. There are two types of photoresist: positive and negative. For positive photoresists, the resist is exposed with UV light wherever the underlying material is to be removed. The mask, therefore, contains an exact copy of the pattern which is to remain on the wafer. The negative photoresist remains on the surface wherever it is exposed, and the developer solution removes only the unexposed portions. Masks used for negative photoresists, therefore, contain the inverse (or photographic "negative") of the pattern to be transferred. The figure 2.3 below shows the pattern differences generated from the use of positive and negative resist.

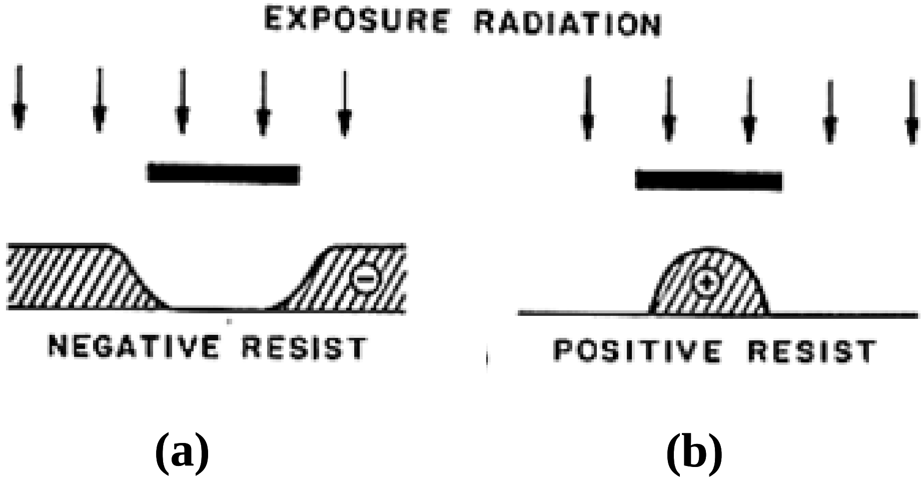

Fig. 2.3. *Photoresist exposure characteristics after development for the (a) negative photoresist and (b) positive photoresist.*

Solid state Equipment Corporation made photoresist spinner has been used for spin coating in this thesis. 'AZ5214 E' as a positive photo resist has been used to produce 1.2μm thin uniform layer on the substrate at a rotation of 3000 rpm for 30 seconds.

2.3.2 Soft-Baking:

Soft-baking is the process during which almost all of the solvents are removed from the photoresist coating. Soft-baking plays a very critical role in photo-imaging. The photoresist coatings become photosensitive only after soft-baking. We have kept the spin coated substrate for 20minutes at 90 ^{0}C temperature, using a photoresist baking oven.

2.3.3 Mask Alignment and Exposure:

One of the most important steps in the photolithography process is mask alignment. A mask or "photomask" is a square glass plate with a patterned emulsion of metal film on one side. The mask is aligned with the wafer, so that the pattern can be transferred onto the wafer surface. For multi-level patterning, each mask after the first one must be aligned to the previous pattern.

Once the mask has been accurately aligned with the pattern on the wafer's surface, the photoresist is exposed through the pattern on the mask with a high intensity ultraviolet light. For the preparation of micro-bridges used for J_C measurement of YBCO film, M'JB3, Karl Suss mask aligner has been used for the mask alignment where Hg-Cd lamp (350 watts) was used as a UV source.

2.3.4 Development:

One of the last steps in the photolithographic process is development. For positive photoresists, the resist solubility in its developer is finite even at zero-exposure energy. The solubility gradually increases until, at some threshold of the exposure energy at which it becomes completely soluble. NaOH solution has been used as a developer.

2.3.5 Hard-Baking :

Hard-baking is the final step in the photolithographic process. This step is necessary in order to harden the photoresist and improve adhesion of the photoresist to the wafer surface. After the development we used to keep the sample inside the oven at 110 ^{0}C for 20 minutes for the purpose of hard baking.

2.3.6 Etching:

In etching, a liquid ("wet") or plasma ("dry") chemical agent removes the uppermost layer of the substrate in the areas that are not protected by photoresist. In order to etch the photo-lithographically patterned film on the substrate, we have used RF ion beam etching system as a dry etching to get the final pattern of the film on the substrate. 150 watt RF power was used to produce the Ar-plasma which took 15 minutes to remove the 100nm thick YBCO film on different substrate to create the 10μm narrow bridge.

2.3.7 Photoresist removal:

After the etching, photoresist is no longer needed and hence it must be removed from the substrate. This usually requires a liquid "resist stripper", which chemically alters the resist so that it no longer adheres to the substrate. Boiled acetone has been used to remove the unwanted positive photo resist on the YBCO film.

2.3.8 Surface profile measurement system:

Profilometer is a measuring instrument used to measure a surface's profile, in order to quantify its roughness and the thickness of the films. We have used DEKTAK 3030 as a contact profilometer for the measurement of the thickness as well as the roughness of the heterostructure multilayer films. A diamond stylus is used as a measuring tip which is moved vertically in contact with a sample and then moved laterally across the sample for a specified distance and specified contact force. It can measure small surface variations in vertical stylus displacement as a function of position. DEKTAK 3030 can measure small vertical features ranging in height from 10 nanometres to 1 millimetre. The position of the diamond stylus generates an analog signal which is converted into a digital signal and then it is stored, analyzed and displayed. The radius of the tip of this diamond stylus is 12.5 μm, and the vertical resolution is 0.1nm.

2.4 Sample preparation:

Two different samples in pellet form have been used for thin film deposition in the present thesis. These pellets are $Pr_{0.5}Ca_{0.5}MnO_3$ and $YBa_2Cu_3O_7$.

2.4.1 Preparation of $Pr_{0.5}Ca_{0.5}MnO_3$:

The synthesis of this sample was carried out starting with high pure rare earth oxide Pr_6O_{11} (99.99%), alkaline earth carbonate $CaCO_3$ (99.999%) and transition metal oxides MnO_2 (99.9%). These compounds were synthesized using solid state reaction method. The stoichiometric proportions of starting oxide and carbonates were weighed and mixed together using agate mortar and pestle to obtain a homogeneous powder. This mixture was then fired at 1000 ^{0}C for 15 hours in air to remove the carbonates from the mixture. After cooling, the mixture was again thoroughly ground and the fine ground powder was pelletized to form uniform and compact pellets. The pellets were sintered at elevated and controlled temperatures by placing them in an Alumina crucible. The sintering was done at 1200°C for 15hrs and finally cooled down to room temperature. The heating and the cooling were done at the rate of 0.5°C /min. The final sintering process was repeated twice at a further elevated temperature of 1350°C, where it was soaked for 24 hours. After each sintering process, intermediate grinding and pelletizing were performed in order to enhance the homogeneity of the samples.

2.4.2 Preparation of $YBa_2Cu_3O_7$:

High pure form of Y_2O_3 (99.9%), $BaCO_3$ (99.999%) and CuO (99.5%) were used to synthesize this sample using solid state reaction method. Stoichiometric quantities of the above three oxides were weighed and the powders were mixed together. This mixture was then annealed at 930°C for 16 hours. After grinding this mixture again, the fine powder of this was pelletized, which were sintered at 930^0C for 24 hours. The heating were done at the rate of 3°C /min whereas cooling rate is 1^0C/min. The sintering process was repeated again after grinding and pelletizing the sample.

2.5 Transport properties characterization

2.5.1 The vander Pauw technique

The vander Pauw technique for resistivity measurements allows avoiding problems due to incorrect knowledge of sample geometry. This technique has been used to measure the resistivity of thin film of PCMO, YBCO and its multilayer heterostructures. The procedure that was adopted to determine the room temperature vander Pauw resistivity of the bulk YBCO, PCMO target and single layer PCMO thin films is schematically described in Figure 2.4.

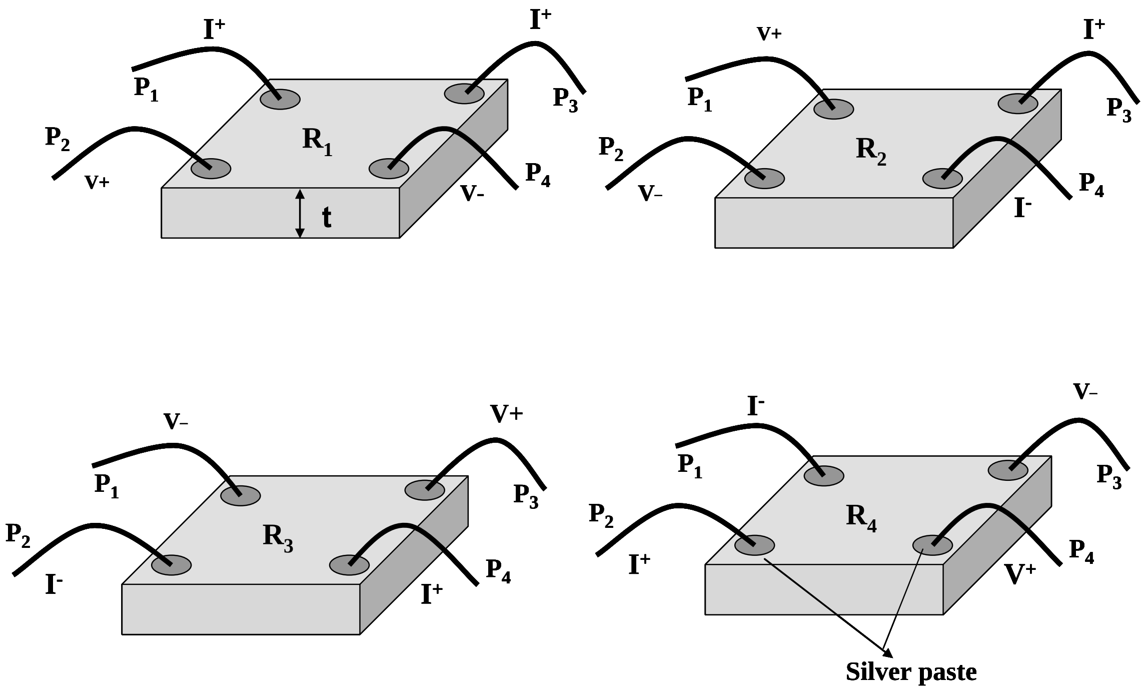

$$\rho^1_{RT} = \rho^1_{RT}(R_1,R_2,t) \qquad \rho^2_{RT} = \rho^2_{RT}(R_2,R_3,t)$$
$$\rho^3_{RT} = \rho^3_{RT}(R_3,R_4,t) \qquad \rho^4_{RT} = \rho^4_{RT}(R_4,R_1,t)$$

Fig. 2.4. *Schematic representation of the contacts used for measuring four probe van der Pauw resistivity.*

Here R_1 and R_2 are the sample resistances at different configurations (see Fig.2.4) and *t* is the thickness of the sample. Four contacts are made on the sample as shown in figure and the four resistances (R_1, R_2, R_3 and R_4) are measured on the sample by sequentially changing the current and voltage leads(P_1, P_2, P_3 and P_4) as shown in Figure 2.4. The room temperature (RT) vander Pauw [4] resistivity (ρ_{RT}) was determined by iteratively solving the equation :

$$exp\left[\frac{-\pi t}{\rho_{RT}} R_1\right] + exp\left[\frac{-\pi t}{\rho_{RT}} R_2\right] = 1$$

where the pair of resistance values (R_2, R_3), (R_3, R_4) and (R_4, R_1) are substituted in place of (R_1, R_2) in the van der Pauw equation and a set of four van der Pauw values

(ρ^1_{RT}, ρ^2_{RT}, ρ^3_{RT} and ρ^4_{RT}) are obtained. The average of these values is taken as the room temperature van der Pauw resistivity (ρ_{RT}) of the sample. The temperature dependent resistance on the sample is then scaled to the ρ_{RT}, by the factor ($\alpha = \rho_{RT} / R_i$) where R_i (i = 1 to 4) is resistance of a particular configuration in which the temperature dependent resistivity $\rho(T) = \alpha \times R(T)$ is to be measured.

The low temperature resistivity setup, used for the thin film resistivity measurement, has a OFHC (Oxygen Free High thermal Conductivity) Cu platform on which a pre-calibrated Si diode sensor is firmly attached using GE-varnish for monitoring the temperature. The sample (thin film) on the substrate, is stuck to the other side of the platform, positioned at the back of the diode sensor, with proper electrical insulation. Four contacts are made on the sample in the van der Pauw geometry using Cu wire (38SWG) glued with silver paste. The leads of the sensor and the sample are soldered onto a connector pad, from which connections to the corresponding current sources and nano-voltmeters were made. The temperature variation of 300K to 4.2K is achieved by inserting the dipstick mounted with the sample and sensor, into a liquid helium storage Dewar, containing the cryogen and making use of the natural thermal gradient. During the insertion, data from the sample and the sensor are simultaneously collected using a LabView program through GPIB interface with a computer. The sequence of data acquisition is as follows. Initially a known minimal current (I), is passed through the sample leads using a DC current source. The Si diode is activated with 10μA current with another similar current source. The sensor voltage is first read, from which the measurement temperature is determined using a set of pre-calibrated coefficients. Then the sample voltages are read with both forward (I^+) and reversed currents (I^-), to eliminate contributions from thermo-emf and from these voltage values the sample resistance is determined as $R_S=V_S / I_S$ where $V_S=V_S^{I+} - V_S^{I-}$. This process of data acquisition is repeated every second while the dipstick is slowly inserted into the liquid helium Dewar to achieve the temperature variation from 300K to 4.2K. After each data collection, the data are written into a file and stored for further analysis. The measurement is generally repeated in the warming run by raising the dipstick and repeatable data could be obtained as in the cooling run, by the slow movement of the dip-stick and ensuring good contacts were made on the samples.

2.5.2 Magnetoresistance setup

The magnetoresistance (MR) setup was the essential instrument with which a majority of the experimental results are presented in this thesis. The magnetoresistance of the samples was measured using a 12 Tesla superconducting solenoid with a 30 mm bore. The magnet is mounted on a platform and suspended inside the tail region of a stainless steel liquid helium cryostat (CVE, Korea) with a liquid helium capacity of 50 *l*. The cross sectional view of the MR cryostat with the magnet is schematically illustrated in Figure 2.5(a) and a photographs of the setup and the sample holder are shown in Figure 2.5(b) and (c) respectively. The evaporation rate of liquid helium in this cryostat is less than 300 cc / hour when the magnet is idle. The sample assembly is placed inside a double walled chamber inside the 30 mm bore of the magnet. During the measurements, the outer region of the double walled chamber is kept at a partial pressure (~ 8 mbar) of helium gas, used as a thermal link to control the temperature of the sample. The inner chamber houses the sample holder assembly, filled with helium gas at a pressure of 1 bar. The desired rate of

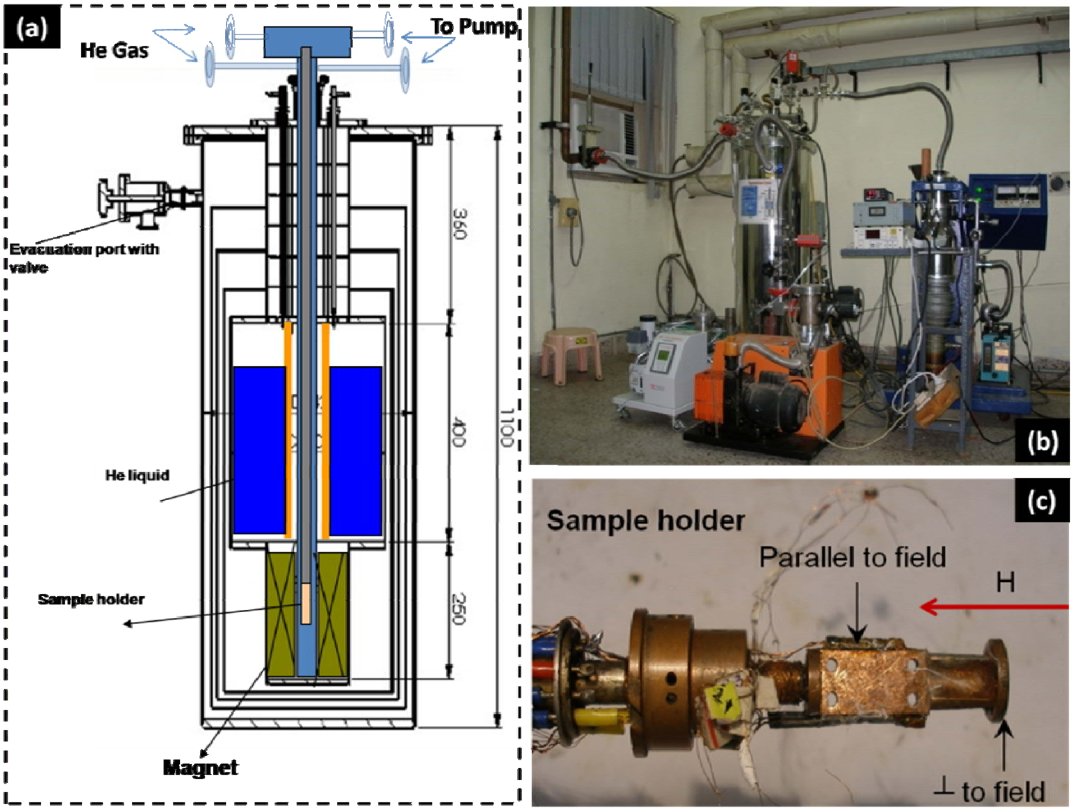

Fig. 2.5. (a) *Schematic cross-sectional view of the MR cryostat illustrating the position of SC magnet, sample holder etc.* ***(b)*** *Photograph of the MR setup* ***(c)*** *Photorgraph of the sample holder; showing the OFHC platforms mentioned in the text.*

cooling and warming is achieved using a temperature controller (Oxford instruments, model ITC503) which uses a heater (manganine wire of resistance 30 Ω) wound around a copper shield, surrounding the sample holder. The copper shield provides a uniform temperature environment for samples. The sample holder is made up of OFHC copper block attached to one end of a SS rod by brazing. The SS rod together with the copper block rests on the top flange of the double wall chamber with a vacuum compatible neoprene O-ring. The current and voltage leads are thermally anchored to the SS rod at various places using GE varnish. The leads are terminated at connection ports in order to avoid the thermal gradient from ambient temperature to OFHC copper sample holder.

Initially, the cryostat and the magnet are pre-cooled, prior to liquid helium transfer. For pre-cooling, the cryostat is filled with liquid nitrogen for 12-24 hours so that the radiation shield and super-insulation cools sufficiently and reaches equilibrium. After pre-cooling, the liquid nitrogen is removed by pressuring the cryostat with hot nitrogen gas. Once the liquid nitrogen is completely removed, the cryostat is purged with helium gas three times. After the purging, liquid helium is transferred. Once the liquid helium bath is filled, the magnet is completely immersed in liquid helium.

The sample holder has three platforms; two for mounting the samples parallel to the field and one perpendicular to the field (Figure 2.5 (c)). For measurements parallel to the field, the sample holder can accommodate four samples with maximum size of 5 mm diameter and 1 mm thickness. Four samples can be mounted two on each side of the copper block. Four different set of probes each consisting of four leads are made available to the connection pad attached to OFHC copper block to feed in the current and to measure the voltage across the four samples. The resistance is measured by four probe technique. A calibrated DC current source (Time Electronics) is used to pass a fixed current to the sample and an Agilent (model 34420A) two channel nano-voltmeter is used to measure the voltage across the sample. The schematic diagram illustrating the

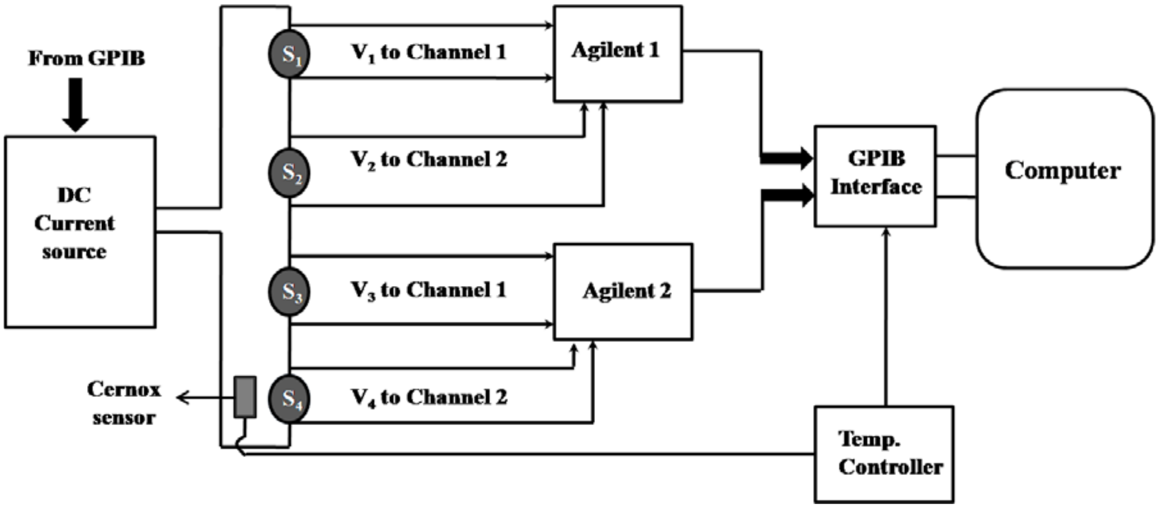

Fig. 2.6. *Schematic illustration of the resistance measurement in MR setup. Four samples are connected in series with a dc current source and the voltage drop across the samples are measured using two channel Agilent nanovoltmeters.*

method of measuring resistance of four samples simultaneously is shown in Figure 2.6. Four samples S_1-S_4 are connected in series and the voltage drop across the four samples V_1-V_4 are measured using two channel Agilent nano-voltmeters. The temperature of the sample is measured using a pre-calibrated cernox sensor which is known to be a good miniaturized temperature sensor at high magnetic fields. The cernox sensor is firmly fixed at one side of the copper block, very close to the samples. The resistances of the sample during positive and negative cycling of currents are measured (in order to remove the contribution from the thermo-emf generated in copper leads) and the averaged value is taken as the resistance at that particular temperature. Current source and Agilent voltmeters are connected to computer through GPIB interface.

2.5.3 Vibrating Sample Magnetometer:

The Vibrating Sample Magnetometer (VSM) supplied by Cryogenic Inc., UK has been used for the magnetization measurement in this thesis. The vibrating sample magnetometer can be operated in the field range of 16 Tesla with a temperature span of 1.6 K to 300 K. In order to generate a signal proportional to the magnetic moment, the sample is set to vibrate in a constant (or slowly varying) applied field. The signal is detected by an astatic pair of pick-up coils. The coils sense the variation of magnetic flux due to the sample movement. The pick-up coils are located inside the Variable Temperature Insert (VTI) within the bore of the superconducting magnet. The signal is detected by a lock-in amplifier. The magnetometer has an automated gas handling system, and the sample is loaded through an airlock. The VTI can be kept at low temperature during sample exchange, which makes the sample replacement easy and quick.

2.6 XRD characterization:

The room temperature powder diffraction pattern of all the samples studied in this thesis are recorded using a STOE diffractometer operated at a power of 40 kV and 30 mA, in the Bragg-Brentano geometry. The X-ray radiation used was the $Cu-K_{\alpha}$ line. The lattice parameters from XRD pattern are extracted using STOE and PCW programs [5]. High resolution XRD for thin film analysis has been done by D8 DISCOVER High Resolution X-ray Diffractometer at UGC-DAE Consortium, Indore.

References:

[1] Singh, R., and Narayan, J. Pulsed-laser evaporation technique for deposition of thin films: Physics and theoretical model. Phys. Rev. B, 41 (13), 8843 (1990).

[2] D. B. Chrisey,, and G. K. Hubler (Eds.). (1994). Pulsed laser deposition of thin films. New York: John Wiley & Sons, Inc.

[3] R. K. Singh and D. Kumar Materials Science and Engineering, R22 113 (1998).

[4] L. J. van der Pauw, Philips. Res. Repts., **13**, 1 (1958)

[5] W. Krause, G. Nolze, Powder Cell for windows, version 2.3 (1999)

Chapter 3

Characterization of YBCO Thin Film & Substrate Induced Strain Effect on PCMO Thin Film

3.1 Deposition and Characterization of $YBa_2Cu_3O_{7-x}$ Thin Film:

3.1.1 Introduction:

Characterization of the individual layers is essential for a comprehensive understanding of the properties of thin film multilayer heterostructures. Here we describe the optimization of the deposition parameters necessary for the realization of high quality thin films of YBCO and PCMO using the PLD technique.

Among many other techniques available for the deposition of thin films, Pulsed Laser Deposition (PLD) has emerged as a popular technique to realize high quality superconducting thin films of YBCO with high superconducting transition temperature [1,2]. A key advantage of PLD over other available techniques is that it allows the deposition process to be carried out in the presence of relatively high partial pressure of oxygen, which is crucial for the growth of high quality thin films of oxide materials [1,4]. Although several research groups have optimized and documented the process parameters for the deposition of YBCO thin films on a given substrate, variations in the size of the PLD chamber and the target to substrate distance make it necessary to standardize the process parameters for a particular PLD set up so as to yield optimum characteristics in the properties of thin films as required for a particular application. In a study undertaken to optimize the deposition parameters, several parameters of interest such as substrate temperature, laser fluence, oxygen pressure and target to substrate distance etc. have been varied. For each set of process parameters, the deposited thin films have been characterized employing a number of experimental techniques such as temperature dependence of normal state resistance using the four probe method, measurement of superconducting transition temperature (T_c) of the thin film etc. Deposited thin films were also characterized by X-ray Diffraction (XRD) for an analysis of structure and crystallographic orientation.

3.1.2 Selection of substrates:

Several different criteria exist that determine the suitability of a particular substrate for the deposition of thin films of HTSC materials; among these, the first one relates to the chemical compatibility of the substrate with the high T_c YBCO thin film, especially at the high temperatures typically used for the in-situ deposition or for the post-deposition annealing in oxygen atmosphere [2,3]. The other important issue is the inertness of the substrate in the oxygen rich ambience required for the growth and processing of HTSC thin films. The next one is the thermal expansion match between the high T_c thin film and the substrate; a mismatch between the thermal expansion coefficients of the substrate and the thin film inevitably generates thermal stresses during repeated thermal cyclings, which can potentially lead to a cracking of the deposited thin film and impair its overall adhesion. Lattice matching is important for the growth of epitaxial thin films. Other physical properties of the substrate such as its dielectric constant may also be important for specific applications. Finally, an important criterion for the selection of a particular substrate in an application is its cost. Based on these criteria, a list of properties which govern the selection of a suitable substrate is given in the table 3.1.1.

Desired Property	Reason
Atomically smooth surface	Increases film uniformity and enables epitaxial growth
Perfect flatness	Important for photolithographic patterning into device geometries
No porosity	Prevents excessive outgassing and improves microstructure of the thin film
Mechanical strength	Prevents film stress
Thermal coefficient of expansion equal to that of deposited film	Minimizes film stress
High thermal conductivity	Prevents heating of circuit components
Resistance to thermal shock	Prevents damage and cracking during processing
Thermal stability	Permits processing at high temperatures
Chemical stability	Permits use of a variety of process reagents
High electrical resistance	Provides insulation of circuit components
Low cost	Permits commercial application
Good lattice match	Maximizes crystalline perfection

Table 3.1.1. *Ideal substrate properties and their influence on film growth [2].*

Though a large variety of substrate materials have been used by other research groups for the deposition of thin films of YBCO, only three of them viz. $SrTiO_3$ (STO), $LaAlO_3$ (LAO) and MgO have been used in the present study for standardizing the process parameters for the deposition of thin films of YBCO. These substrates are ideally suited for the deposition of charge ordered $Pr_{0.5}Ca_{0.5}MnO_3$ and YBCO thin films and for the investigation of the effects of substrate induced strain in thin film heterostructures.

Table 3.1.2 lists the bulk crystal structures, lattice constants, lattice mismatch and thermal expansion coefficients of STO, LAO and MgO which are used as substrates for the deposition of YBCO thin films. It is well known that the a and b lattice constants of YBCO are not equal; hence, the use of substrate materials like STO and LAO (closely lattice matched to YBCO) or MgO (less closely lattice matched to YBCO) will produce twinned region and 45^0 grain boundary in the deposited YBCO film [5]. However, it is found in practice that the overall epitaxial growth of the YBCO film on these substrates is not hampered if suitable precautions are taken during the deposition of the YBCO thin film. It may be noted that the thermal expansion coefficients of MgO and STO are slightly larger than that of YBCO. This means that after cooling from high temperatures typically used for their deposition, YBCO films tend to be under compressive stress when grown on these substrates implying that, in general, cracking is not likely to occur [1,2].

Material	Structure	Lattice constant (Å)	Thermal expansion coefficient ($10^{-6}/^{0}C$)	Lattice mismatch (%)
$Y_1Ba_2Cu_3O_7$ (YBCO)	Orthorhombic	a=3.83 b=3.89 c=11.7	8.5	-----
$SrTiO_3$ (STO)	Cubic	3.905	9.4	1.9
$LaAlO_3$ (LAO)	Rhombohedral	3.79($\alpha=90^{0}5'$)	9.8	-1.0
MgO	Cubic	4.21	14	9

Table 3.1.2: *Crystal properties of bulk YBCO, STO, LAO and MgO substrates [1,2]. Lattice mismatch of substrates with respect to YBCO is indicated in the last column.*

3.1.3 Film deposition:

In the present work, thin films of YBCO have been deposited on the polished and cleaned surface of STO, MgO and LAO substrates. The substrates were cleaned successively in an ultrasonic bath with acetone, boiling isopropanol and thoroughly dried by blowing compressed nitrogen gas. The substrate was then mounted on the substrate holder using a thin layer of silver paste to attach the substrate firmly to the substrate holder in order to provide good thermal contact between the substrate and the substrate holder. The silver paste is usually dried outside the chamber without heating it. Then the substrate holder, which is equipped with a heater to raise the substrate temperature upto 900°C, was attached to a support structure in the PLD vacuum chamber (schematic diagram has been given in chapter 2) in such a way that the substrate is approximately 30mm away from the YBCO target. The face of the substrate is aligned parallel to the face of the target and it is positioned in the PLD chamber in such a way that the substrate will intercept the centre of the plume produced by the laser when it strikes the target. The YBCO target is stoichiometric and is prepared from YBCO powder pressed into 15mm diameter disk and sintered at high temperatures. The preparation of the YBCO target has been described in detail in chapter 2.

For the deposition of the YBCO thin film, the deposition chamber is initially evacuated to a vacuum of about 2.0×10^{-5} mbar using a turbo-molecular pump and the substrate temperature is maintained at 840^{0}C using a PID temperature controller. A KrF excimer laser (wave length: 248nm) with a fluence of ~ 1.2 J/cm^2 and a pulse repetition rate of 5Hz was used for the deposition of the YBCO thin film. Pulsed laser deposition was carried out under an oxygen pressure of 0.33 mbar with a flow rate of oxygen gas set to 40 sccm using a mass flow controller. The surface of the target is cleaned with 1000 laser shots with the shutter closed to prevent the deposition of any material on the substrate during this precleaning. Finally, the shutter is opened and the deposition of the YBCO thin film on the substrate is carried out to achieve the required thickness. After the deposition, oxygen pressure in the chamber is kept at 1000mbar and the freshly deposited YBCO thin film is allowed to cool rapidly from 840 °C to 450 °C in 30 minutes and subsequently it is annealed at 400 °C for one and a half hours. This deposition procedure has been optimized after carrying out several trial runs to study the influence of process parameters on the properties of deposited YBCO thin films and were then used for all the three substrates, viz. STO, LAO and MgO.

3.1.4 Film characterization:

The thickness and surface roughness of the YBCO thin films were evaluated using DEKTAK surface profiler. The thickness of the YBCO thin films was measured to be 100nm (for 5000 laser pulse shots) and the surface roughness of the YBCO thin films was within a range of 5-6nm. YBCO bulk polycrystalline sample (which was used as PLD target) and the YBCO thin films deposited on three different substrates have been characterized by X-ray diffraction (XRD) measurements in a STOE diffractometer using Cu K_α radiation. XRD patterns of the deposited YBCO thin films and bulk YBCO target are shown in figure 3.1.1(a), (b), (c) and (d) respectively. All the diffraction lines could be indexed to an orthorhombic unit cell with lattice parameters, a = 3.825 Å, b = 3.895 Å and c = 11.672 Å [2]. No impurity lines were seen in XRD confirming that all the samples investigated are single phase pure samples upto the limit of detection by this technique. As shown in fig. 3.1.1(a), (b) and (c), the presence of only (00l) lines in the XRD pattern of the YBCO thin films deposited on LAO, STO and MgO substrates indicates that all the thin films are c-axis oriented.

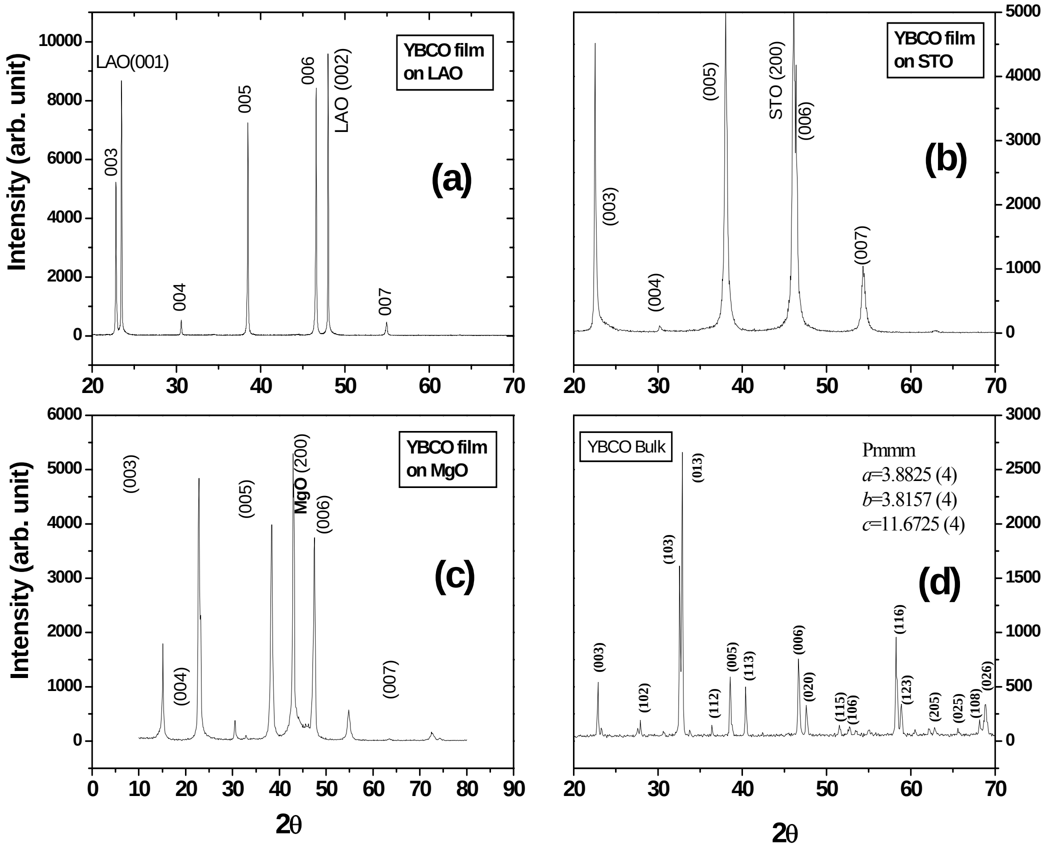

Fig. 3.1.1. XRD patterns of YBCO thin films grown on (a) LAO, (b) STO and (c) MgO substrates respectively. (d) XRD pattern of bulk YBCO target.

The temperature dependent resistances (*R(T)*) of the YBCO thin films deposited on three different substrates viz., LAO, MgO and STO, along with that of the bulk polycrystalline bulk YBCO, have been measured using the standard four probe technique to eliminate the parasitic contact resistance. For these measurements, four copper leads were attached to each thin film sample using silver paste. Two leads were used for passing electrical current of 10μA and other two leads were used for voltage measurement. The results of these measurements are shown in fig. 3.1.2.

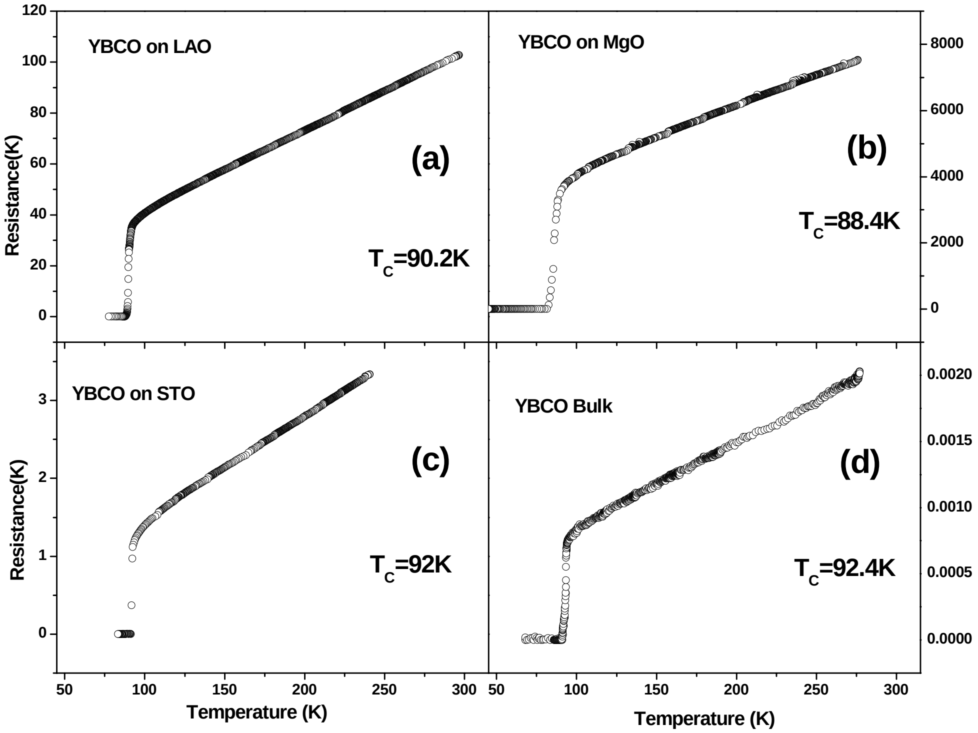

Fig. 3.1.2. *Variation of the resistance of the YBCO thin film deposited on (a) LAO, (b) MgO and (c) STO substrates as a function of temperature. In all the measurements, T_c onset is inferred from the intersection of the linear resistivity behaviour above T_c and the precipitous fall in resistance accompanying the superconducting transition. (d) Variation of resistance of the polycrystalline bulk target as a function of temperature.*

Fig. 3.1.2 shows that the properties of YBCO thin films with similar thickness (~100nm) grown on (100) oriented LAO, MgO and STO substrates differ from each other. The T_c of YBCO thin films deposited on the MgO substrate was observed to be the lowest (~ 88.4 K) compared to the T_c observed for YBCO thin films deposited on STO (T_c ~92K) and LAO (T_c ~ 90.2K) substrates. It is also observed that for the YBCO thin film deposited on the MgO substrate, the room temperature resistance is the highest while the the ratio of R_{300K} / R_{100K} is the lowest although all the thin films exhibit a linear variation of the normal state resistance with temperature. It may be noted that R_{300K} and R_{100K}

denote the electrical resistance of the thin film measured at room temperature (300K) and at 100 K respectively. The slightly poorer quality of the YBCO thin films deposited on MgO substrate as compared to those deposited on STO and LAO substrates has also been reported by other research groups and has been attributed to the presence of higher granularity [2] in the former compared to the latter. The granularity in the YBCO thin films has been found to be dependent on the lattice mismatch with the substrate; larger the lattice mismatch with the substrate used, larger would be the granularity in the deposited YBCO thin films [2].

The critical current densities (J_c) of the YBCO thin films deposited on LAO, STO and MgO substrates have been experimentally measured. For these measurements, a photolithographically patterned micro-bridge, which is just 10μm wide, is fabricated on each YBCO thin film to evaluate the corresponding J_c. A schematic diagram of the micro-bridge is shown in figure 3.1.3. The micro-bridge is terminated with four contact pads, which serve to pass electric current and to measure the resulting voltage, if any. Silver paste of high electrical conductivity has been used to connect the current and voltage leads to the contact pads photolithographically patterned on the thin film. After immersing the thin film sample in liquid helium (4.2K), the current passing through the micro-bridge is slowly increased while simultaneously measuring the potential difference developed across the micro-bridge at each value of the measuring current. The maximum value of the current which can be passed through the micro-bridge while the potential difference developed across the micro-bridge remains zero is defined as the critical current of the micro-bridge at 4.2K. The value of the critical density J_c of the YBCO thin film is obtained by dividing the critical current of the microbridge by its cross-sectional area. The experimentally measured values of J_c for all the YBCO thin films deposited on different substrates have been tabulated in table 3.1.3. The highest value of J_c is observed for the YBCO thin film deposited on STO substrate while the smallest value of J_c is observed for the YBCO thin film deposited on MgO substrate.

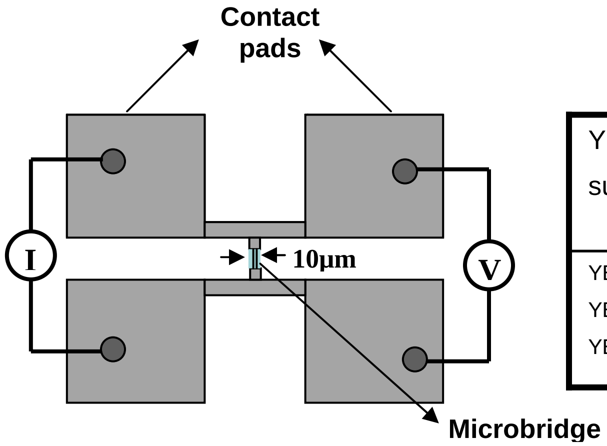

YBCO film on the substrate	Critical current density (J_c) at 4.2K (Amp/cm^2)
YBCO on STO	2.3 X 10^6
YBCO on LAO	2.0 X 10^6
YBCO on MgO	0.9 X 10^6

Fig. 3.1.3. *Schematic of the microbridge photolithographically patterned on the YBCO thin films deposited on different substrates for measuring the value of J_c.*

Table 3.1.3: *Measured values of J_c of the YBCO thin films deposited on STO, LAO and MgO substrates at 4.2K.*

Post deposition annealing of the YBCO thin film is extremely important in order to obtain high quality YBCO thin films with relatively high superconducting transition temperature T_c. This is illustrated in fig. 3.1.4, which shows the temperature dependence of the resistance measured for an as deposited “virgin” sample and the sample subjected to post-deposition anneal. In the absence of the post-deposition annealing, a negative temperature coefficient of resistance is observed since the deposition was carried out at relatively low oxygen pressure in the chamber (~100 mbar); a post deposition annealing at 1000 mbar oxygen pressure restores the metallic behavior and results in YBCO thin films with superior properties.

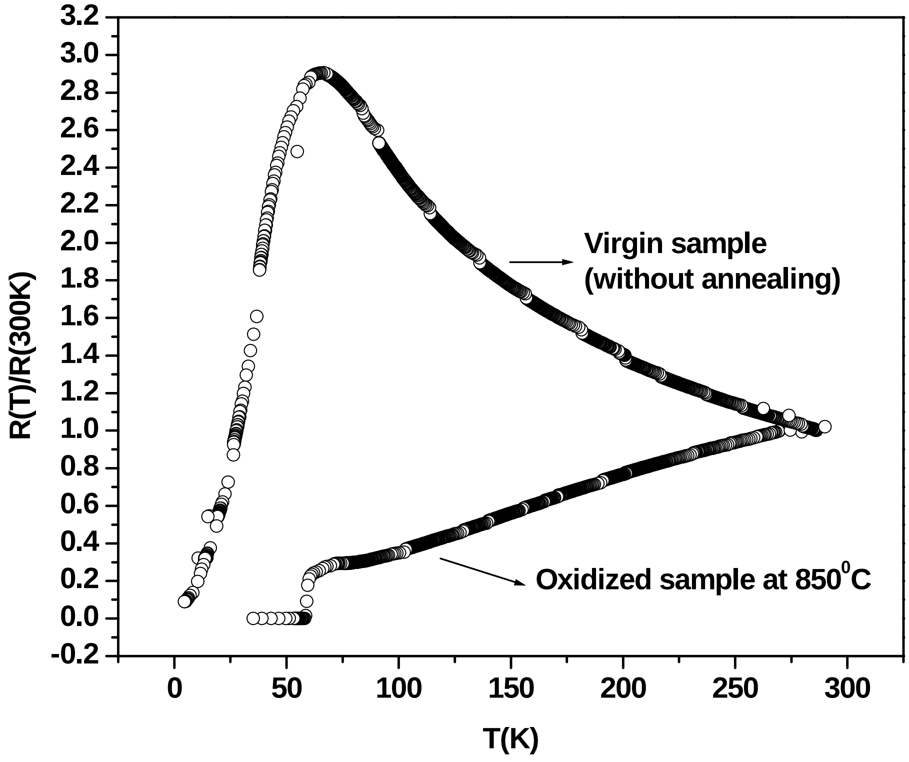

Fig. 3.1.4. *Variation of the normalized electrical resistance of YBCO thin films as a function of temperature with and without post-deposition anneal.*

The variation of the temperature dependent resistance of the YBCO thin films as a function of measuring current has been investigated for a YBCO thin film deposited on STO substrate and the typical experimental results are shown in figure 3.1.5 for a range of sample currents upto 200 mA. For these measurements, four electrical leads were attached to the YBCO thin film using silver paste; two leads were used for applying current and the other two leads were used for measuring the voltage developed across the sample. The resistance measurements were performed using the standard four probe technique over a temperature range of 4.2K to 300K with applied sample current ranging from 50μA to 200mA. Special precautions like good thermal anchoring and allowing adequate time between two consecutive measurements were taken to avoid local heating due to high applied current. Inset of figure 3.1.5 shows the variation of the superconducting transition temperature T_c with applied sample current. Here, different scaling factors have been used for plots corresponding to different applied values of current for clarity. It is evident from fig. 3.1.5 that there is only a very small change in the value of observed T_c of the YBCO thin film over the range of applied currents investigated; this small change in the observed T_c probably arises due to local heating.

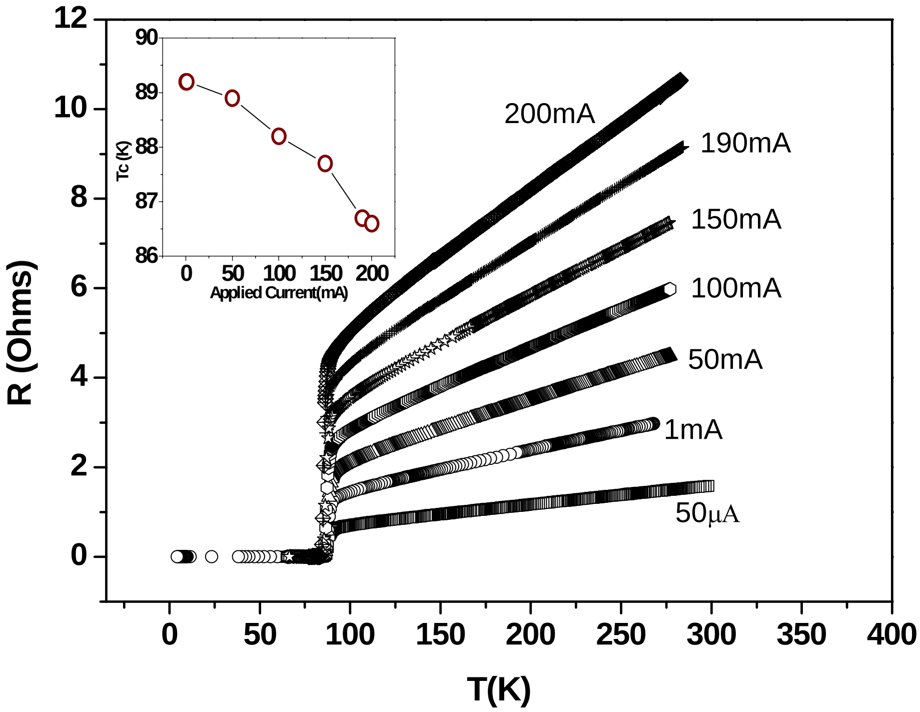

Fig. 3.1.5. *Variation of electrical resistance of the YBCO film as a function of temperature for different values of applied current. Different scaling factors have been used for plots corresponding to different values of applied current for clarity. Inset shows the variation of onset* T_c *with different values of applied current.*

3.1.5 Summary:

YBCO target has been prepared by solid state reaction method and characterized with X ray diffraction (XRD) and the measurement of electrical resistance as a function of temperature. Superconducting transition temperature T_c for the YBCO thin film deposited on STO substrate was observed to be 92.4 K. A number of YBCO thin films were deposited on three different substrates, viz., STO, LAO and MgO. The deposition parameters have been optimized for the growth of high quality thin films of YBCO. All the thin films were characterized using XRD and four probe resistivity measurement technique. XRD data shows c-axis oriented growth of the YBCO thin film deposited on all the three substrates. The electrical resistance measurements show that the maximum T_c (~92K) is obtained for the YBCO film grown on STO substrate whereas the T_c for the YBCO thin film grown on MgO substrate was observed to be 88.4 K. Measurements of electrical resistance of YBCO thin film were performed for different values of applied currents ranging from 50μA to 200mA and these measurement showed only a relatively small change in the superconducting transition temperature T_c as a function of applied current.

3.2 Substrate Induced Strain Effect on $Pr_{0.5}Ca_{0.5}MnO_3$ Thin Film:

3.2.1 Introduction:

As discussed in chapter 1, this thesis describes the experimental investigations carried out on FM/SC thin film heterostructures based on $Pr_{0.5}Ca_{0.5}MnO_3$ (PCMO) charge-ordered manganite and $YBa_2Cu_3O_{7-x}$ (YBCO) superconductor [6-18]. PCMO is a charge ordered insulator; it is well known that application of external control variables such as magnetic field, electric field, substrate induced strain, photon exposure etc. can potentially melt the charge-order and transform PCMO from the Charge Ordered (CO) insulating phase to a Ferromagnetic Metallic (FM) phase [9-11]. $Pr_{0.5}Ca_{0.5}MnO_3$ (PCMO) is a paramagnetic insulator at high temperature and undergoes a phase transition into a charge ordered insulating state below around 240 K. A charge exchange (CE) type antiferromagnetic order sets in at still lower temperatures (viz., ~170K) [13]. As discussed earlier, it is possible to destroy the charge ordered (CO) state and induce an insulator to metal transition [15] by the application of an external magnetic field. The destruction of the CO state is accompanied by a magnetic transition and a CMR effect [16]. A magnetic field of around 25 T is required to melt the CO state in bulk PCMO [16]. On the other hand CO melting occurs at a lower magnetic field [17-20] in the case of thin films. The effect of tensile and compressive strains induced by the substrate lattice mismatch on the CO melting in PCMO has already been studied [8]. In PCMO thin films with tensile strain grown on STO substrates, CO melting occurs at much lower values of magnetic fields (depending on the thickness of the film) compared to the bulk, whereas in the PCMO films with compressive strain grown on LAO substrates, magnetic field is reported to have a weaker effect [14, 21-23]. In the present chapter, the observation of charge order melting for very thin films of PCMO grown on highly lattice mismatched MgO substrate is described [8]. These studies also reveal that the orientation of the deposited thin film with respect to the substrate plays a crucial role in dictating the nature of the strain and, consequently, the CO melting.

3.2.2 Film Deposition:

Thin films of PCMO, with three different thicknesses of 35nm, 120nm and 200 nm respectively, were grown by the pulsed laser deposition (PLD) technique on (100) oriented MgO substrates. This substrate was chosen because of its higher lattice mismatch with that of PCMO. In particular the lattice mismatch δ defined by $\delta = (a_S - a_T)/a_S$, (where a_S and a_T are the lattice parameters of the substrate and bulk PCMO respectively) is calculated to be + 9.4 % for MgO; this value of δ is very large compared to the value of δ for STO (+ 2.25 %: tensile strain) or LAO (– 0.77 %: compressive strain) substrates [8], and results in a large tensile strain. Thus one can expect a large effect of strain on the CO state of PCMO in the films deposited on the MgO substrate. All the films were deposited by pulsed laser deposition technique using KrF excimer laser (wave length: 248 nm) with a fluence of ~ 1.1 J/cm^2 and pulse repetition rate of 5 Hz. Laser deposition was carried out under an oxygen pressure of 0.15 mbar with a flow rate of 40 sccm, after obtaining a base pressure of $\sim 3 \times 10^{-5}$ mbar in the chamber. The substrate temperature was maintained at 800 ºC and the substrate to target distance was kept at 4 cm during the deposition. After the deposition, the thin films were allowed to cool to room temperature in ~ 2 hours under 1 bar oxygen pressure.

The thickness and surface roughness of the films were measured using DEKTAK surface profiler. The crystal structure and the orientation of the thin films and the bulk polycrystalline target were characterized by X-ray diffraction (XRD) measurements in a STOE diffractometer using Cu K_α radiation. Electrical resistivity measurements were carried out in the temperature range 4.2 – 300 K using the four probe technique in a dipstick cryostat. Magnetoresistance (MR) measurements for all the thin film samples were carried out with the magnetic field (up to 12 T) applied parallel to the plane of the film. The details of the MR measurements have been described in chapter 2. MR of 35 nm film was measured by applying the magnetic field parallel as well as perpendicular to the plane of the film in order to check for any anisotropy in magnetoresistance. A calibrated cernox resistance thermometer was used for the temperature measurements in the presence of magnetic field.

3.2.3 Experimental Results:

Figure 3.2.1 shows the XRD pattern of bulk PCMO. All the lines could be indexed to an orthorhombic unit cell with lattice parameters, a = 5.3912 Å, b = 7.6304 Å and c = 5.4011 Å which are very close to the values reported in the literature [8] (a = 5.395 Å, b = 7.612 Å and c = 5.403 Å). Magnetization was measured down to a temperature of 10 K using a vibrating sample magnetometer (VSM) operating at 20.4 Hz. The results of the magnetization measurements are shown in the inset of Figure 3.2.1. The sharp drop in the magnetization at 240 K is associated with the transition from a paramagnetic (PM) state to a charge-ordered (CO) state as this drop appears to be a characteristic signature of the CO transition in PCMO [6]. Also the observed CO transition temperature of 240 K is very close to the value reported in the literature for PCMO based on neutron powder diffraction results. The phase diagrams reported by other research groups indicate that, for this composition, PCMO is antiferromagnetic at the lowest temperatures with the antiferromagnetically ordered phase appearing around 150 K. There is a small, but noticeable, change in the slope of the magnetization data (a small “hump”) around 150 K which can be used to identify the antiferromagnetic ordering as well [6].

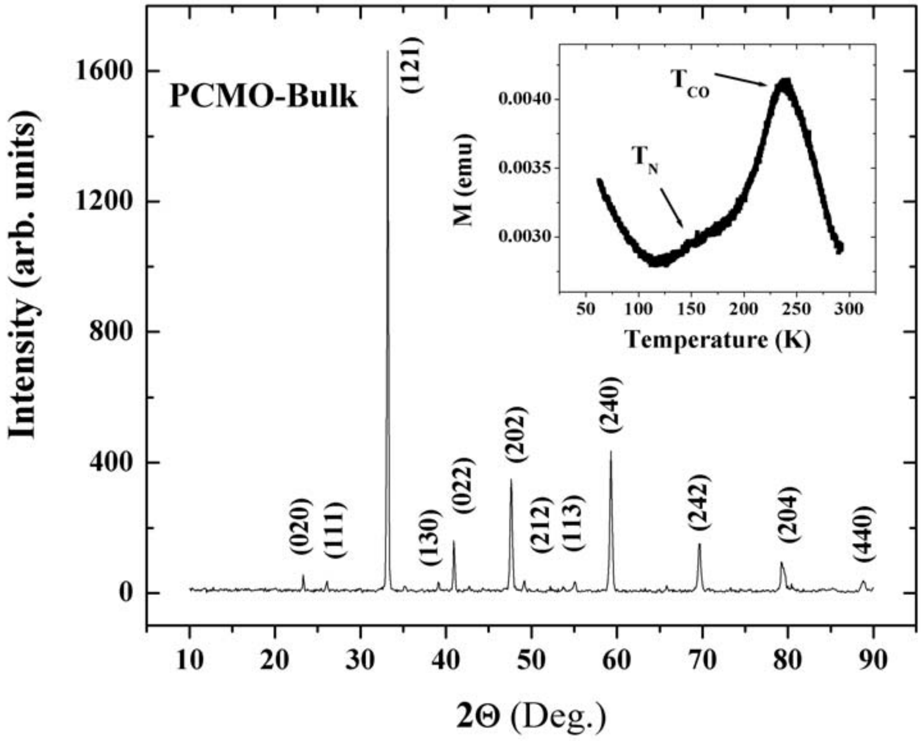

Fig. 3.2.1. *The XRD pattern of the polycrystalline bulk PCMO. The temperature dependent magnetization data is shown in the inset.* T_{CO} *and* T_N *are marked using arrows.*

The thicknesses of the thin films were measured to be 35, 120 and 200 nm using the DEKTAK surface profiler (designated henceforth as P35, P120 and P200 respectively). The average surface roughness of the films determined by the DEKTAK surface profiler was found to vary from 5.5 nm to 6.5 nm. Figure 3.2.2 represents the XRD patterns of these three thin films. All the films are observed to have (121) orientation (*i.e*., [121] axis perpendicular to the plane of the substrate). It may be noted that the d spacing corresponding to the (002) reflection (d = 2.700 Å) almost matches with that of the (121) reflection (d = 2.698Å). However, considering the large lattice mismatch between the *ab* plane of PCMO and the MgO substrate, it is very unlikely for the films to grow with

(002) orientation. Very small intensity lines indexed as (202) and (240) are also observed in some of the films as shown in figure 3.2.2. A broad peak has been observed close to 2θ value for the (002) reflection corresponding to the MgO substrate. The XRD patterns of the bare single crystalline MgO substrate before and after annealing (under conditions identical to those used during the deposition of PCMO films) are shown in the inset of figure 3.2.2(a).

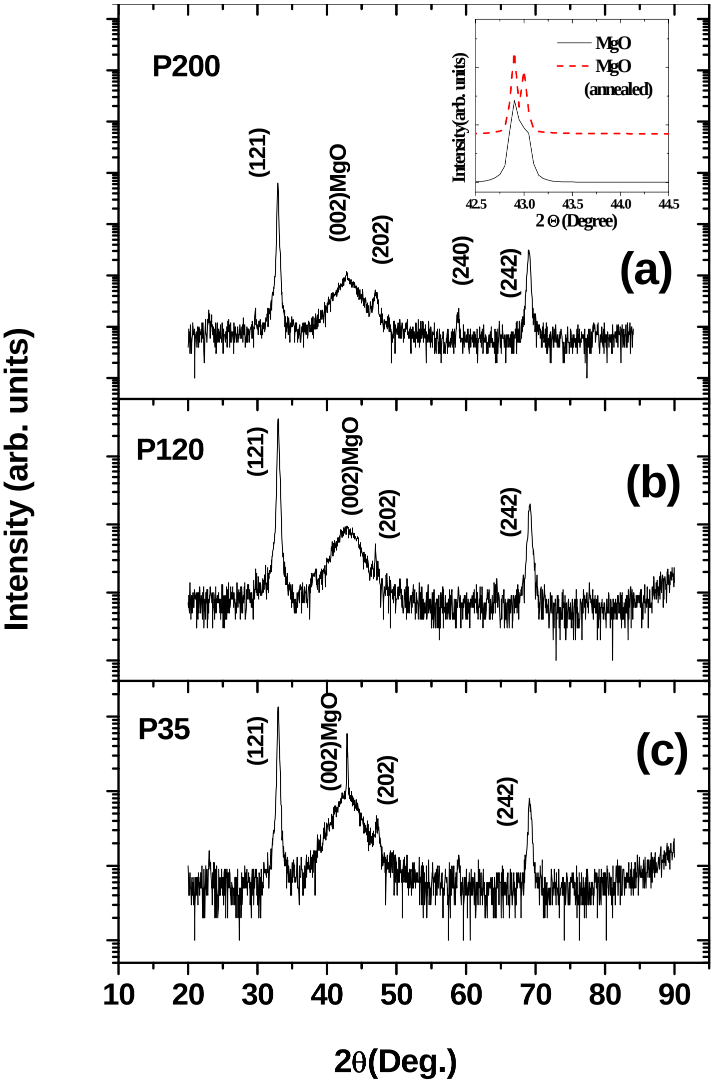

Fig. 3.2.2. *The XRD patterns of the films with thicknesses (a) 200 nm, (b) 120 nm and (c) 35 nm. All the films have (121) orientation. Inset of figure 3.2.2 (a) shows the XRD patterns of the bare single crystalline MgO substrate before and after annealing.*

As seen in the inset, both the patterns for the virgin MgO substrate exhibit a sharp MgO (002) peak with a characteristic splitting due to CuKα_1 and CuKα_2 radiation. This implies that the quality of substrate is good even under thermal treatment. Therefore, plausible reasons for the observed broadening of MgO (002) peak accompanying the diffraction pattern of the PCMO films may include the divergence and the secondary scattering of the X-ray beam from the PCMO films. Secondary scattering occurs when the intense diffracted beam of X-ray from the highly oriented MgO substrate passes through the top PCMO layer. The temperature dependent resistivity (*ρ(T)*) for these thin films along with that for the bulk polycrystalline PCMO is shown in Figure 3.2.3.

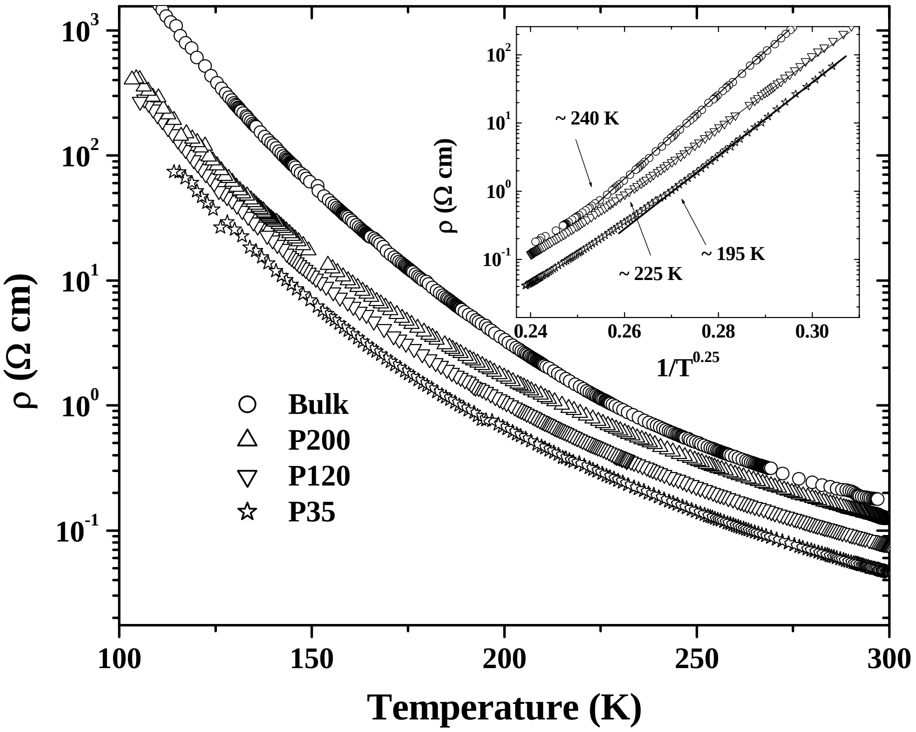

Fig. 3.2.3. *Resistivity vs temperature data for the bulk as well as a few representative thin film samples. Semi-logarithmic plots of resistivity as function of 1/*$T^{0.25}$ *for the bulk as well as the films P120 and P35 are shown in the inset for the temperature range from room temperature to 108K.*

The resistivity shows a negative temperature coefficient of resistance resembling a semiconductor-like behavior in the entire temperature range studied. A systematic reduction in resistivity is observed with decrease in film thickness indicating that the changes in the resistivity are intrinsic to the film. A variable range hopping type of conductivity (Resistivity, $\rho \propto exp\ (T_0/T)^{0.25}$ where T_0 is hopping parameter) is observed at low temperatures for the bulk and thin film samples as shown in the inset of Figure 3.2.3. The ρ vs $1/T^{0.25}$ plots for the bulk, and the thin films P120 and P35, drawn on a semi-logarithmic scale, are shown in the inset of figure 3.2.3. For the bulk sample, there is a deviation from the linear behavior near ~ 240 K, which is identified as the T_{CO}. Above this temperature, a thermally activated behavior for conductivity, viz., $\rho \propto exp\ (\Delta E/k_BT)$, where ΔE is the activation energy and k_B is *the* Boltzmann constant, is observed. In the samples P120 and P35, the slope change is observed at around ~ 225 K and ~ 195 K respectively, as shown in the inset of figure 3.2.3. We could not obtain the T_{CO} of the thin films from the magnetization measurements as the signal levels were below the detection limit of the VSM. Yang *et. al* [24] have estimated the T_{CO} of thin films by considering similar slope changes in the resistivity plot. Following this report, if we assume the slope change in ρ vs $1/T^{0.25}$ to be due to the CO transition, T_{CO} seems to decrease with decrease in the film thickness. Even though it is difficult to obtain the exact temperature at which the slope change occurs, the decrease in T_{CO} with decrease in film thickness is quite apparent from the plot shown in the inset of figure 3.2.3. If that is the case, the systematic decrease in resistivity observed with decrease in film thickness can be attributed to the stabilization of CO at a lower temperature, as compared to that in the bulk sample.

Magnetoresistance (MR) measurements were carried out for all the films by applying magnetic fields up to 12 T. Film with 35nm thickness showed an insulator to metal transition (MIT) on application of magnetic field. On the other hand, films with higher thicknesses did not show the MIT in the range of temperature and magnetic fields investigated. A negative MR is observed in all these films at low temperatures.

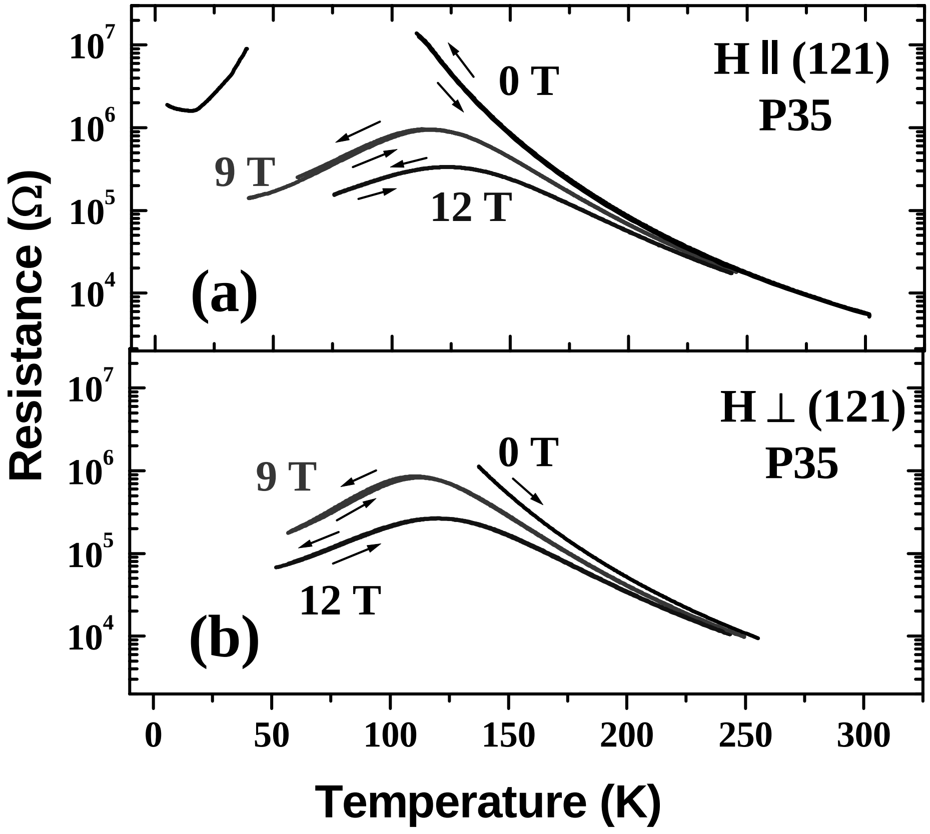

Fig. 3.2.4. *Temperature dependent resistance data under different magnetic fields for the film P35 with field (a) parallel and (b) perpendicular to the (121) plane. The cooling and warming cycles are marked with arrows.*

Figure 3.2.4 (a) represents the temperature dependent resistance of P35 with the magnetic field applied parallel to the plane of the film (*i.e.*, parallel to the (121) plane). An insulator to metal transition, corresponding to the CO melting, occurs under applied magnetic field. As can be seen from Figure 3.2.4 (a), a metallic behavior in resistivity is observed in P35 even under zero magnetic field at temperatures below ~ 50 K. The resistance data for the cooling and warming cycles are marked by the arrows in the figure. A small hysteresis, present between the cooling and the warming cycles, decreases with increase in the magnetic field. This result is at variance with the reported observations of other workers who have investigated the bulk and thin films of PCMO deposited on STO substrate [9]. The temperature corresponding to the MIT increases with increase in magnetic field. Magnetoresistance measurements for P35 were also carried out by applying the field perpendicular to (121) plane; these results are shown in Figure 3.2.4 (b). The absence of a significant anisotropy is evident from a comparison of figure 3.2.4 (a) and (b). MR is also measured for the film P35 at four different temperatures by changing the magnetic field from 0 to 12 T. The results of the field scan for P35 carried out at 52.5 K, 104 K, 136.5 K and 162.5 K are shown in figure 3.2.5 (a), (b), (c) and (d) respectively. The first two temperatures (52.5 K and 104 K) are arbitrarily chosen below the MIT temperature and other two (136.5 K and 162.5 K) are above it.

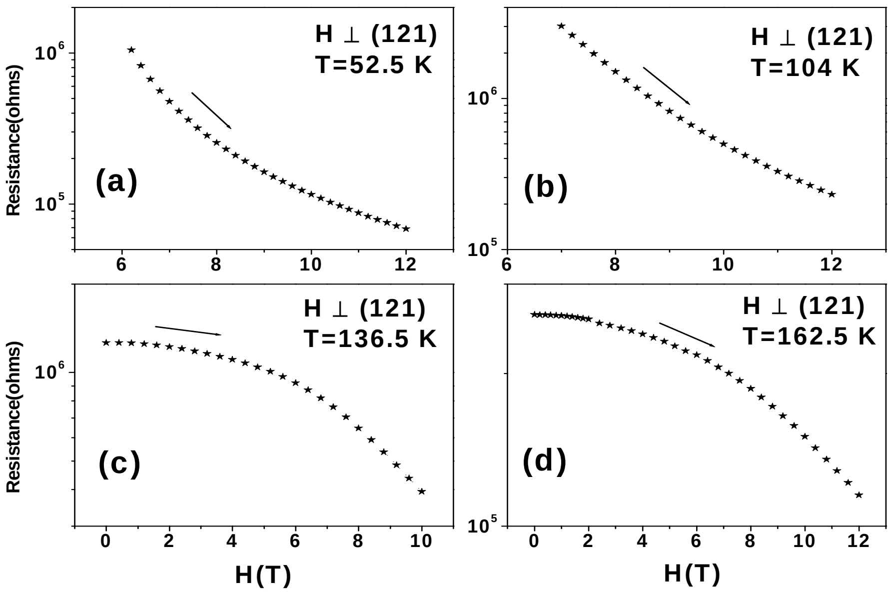

Fig. 3.2.5. *The resistance measured by scanning the magnetic field from 0-12 T at (a)52.5K, (b) 104K, (c) 136.5K and (d) 162.5K for P35 films.*

Figure 3.2.5 (a) and (b) show that the film is insulating and exhibits very high values of resistivity at relatively low temperatures under zero applied magnetic field. But the resistance starts decreasing rapidly at higher magnetic field which is seen by the positive curvature of the plot indicating a transition from insulating to metallic behavior. On the other hand, figure 3.2.5 (c) and (d) show a negative curvature of the plot with a slower rate of change of resistance with magnetic field which is probably due to the fact that there is no change in the conduction behavior at these temperatures.

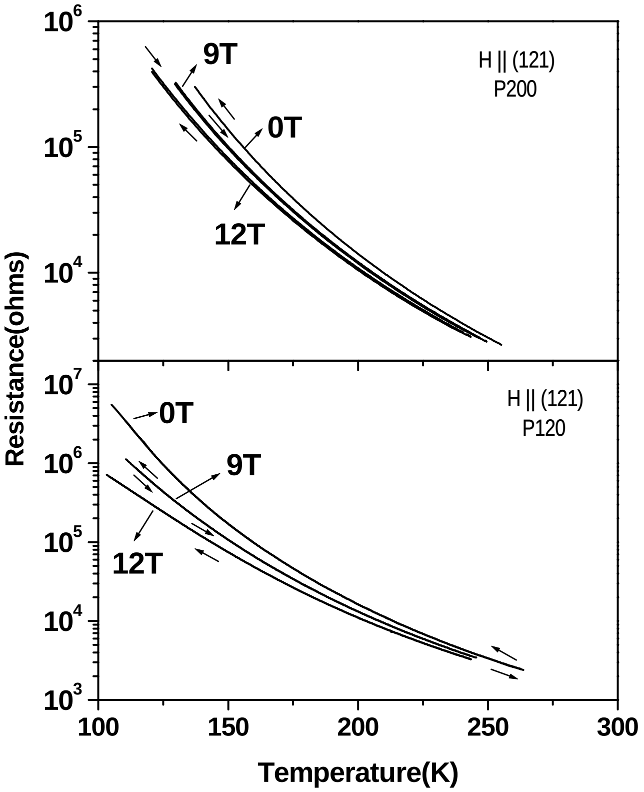

Fig. 3.2.6. *The temperature dependent resistance data for (a) P120 and (b) P200. A negative MR is observed for both the films.*

The films with higher thicknesses did not show the MIT even under the application of a field of 12 T. The resistance data for P120 and P200 taken under different magnetic fields are shown in figure 3.2.6 (a) and (b) respectively. A negative MR is clearly observed for non-zero external magnetic field. Another set of three films of different thicknesses (namely 25nm, 42nm and 65nm), which are very close to the thickness of 35nm film, were deposited on MgO substrate, maintaining nominally identical deposition conditions in order to clarify the role of thickness in driving the MIT. The behavior of all these three films has been studied by measuring the electrical resistance of the films as a function of temperature in different applied magnetic fields and the results are shown in figure 3.2.7.

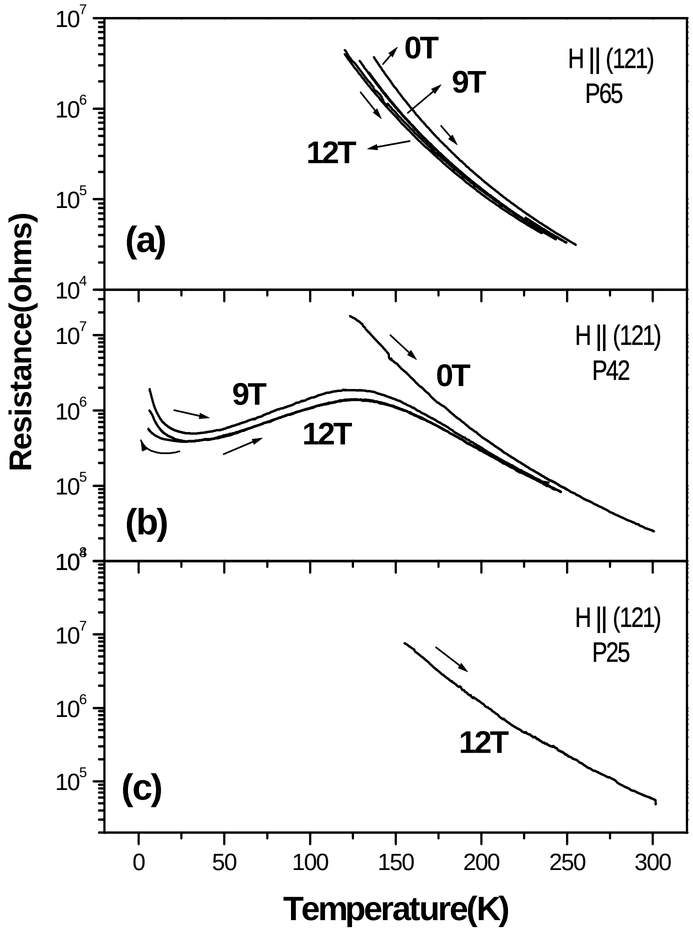

Fig. 3.2.7. *The temperature dependent resistance data for PCMO film of thickness (a) 65nm, (b) 42nm and (b) 25nm. A negative MR is observed for films (a) & (b). For P25 film, the resistance is measured only at H=12T.*

In all the experiments, the magnetic field was applied parallel to the plane of the film. Figure 3.2.7 (b) depicts the MR behaviour of the P42 film. Under zero applied magnetic field, MIT is not observed for P42 unlike the behaviour exhibited by P35. However, under the application of external magnetic field, P42 also exhibits the MIT as shown in Fig 3.2.7 (b). P42 also shows a small hysteresis between the cooling and the warming cycles, which decreases with increase in the applied field. On the other hand, P65 and P25 films did not show the MIT in the range of temperatures and magnetic fields investigated. Figure 3.2.7(a) shows the MR behaviour of P65 film at 0T, 9T and 12T magnetic field; a negative MR is observed at low temperatures. Figure 3.2.7(c) shows the MR behaviour of P25 film at 12T magnetic field.

It is seen from the MR results for all the films ranging from 25nm to 200nm thickness that MIT is observed in only a narrow range of thickness of the PCMO film. Therefore thickness plays a crucial role implying that the observation of MIT is linked to the substrate induced strain effect. To understand the strain evolution with the thickness, all the films were further analyzed by high resolution XRD using D8 DISCOVER High Resolution X-ray Diffractometer. The probing angle was confined to the region where (121) and (242) peaks are seen. Figure 3.2.8 (a) shows the variation of the diffracted intensity as a function of 2θ in the vicinity of the (121) peak position for all the six films of different thicknesses. The Gaussian fit of the XRD data gives the peak position for each film which is shown as a function of film thickness in figure 3.2.8(b).

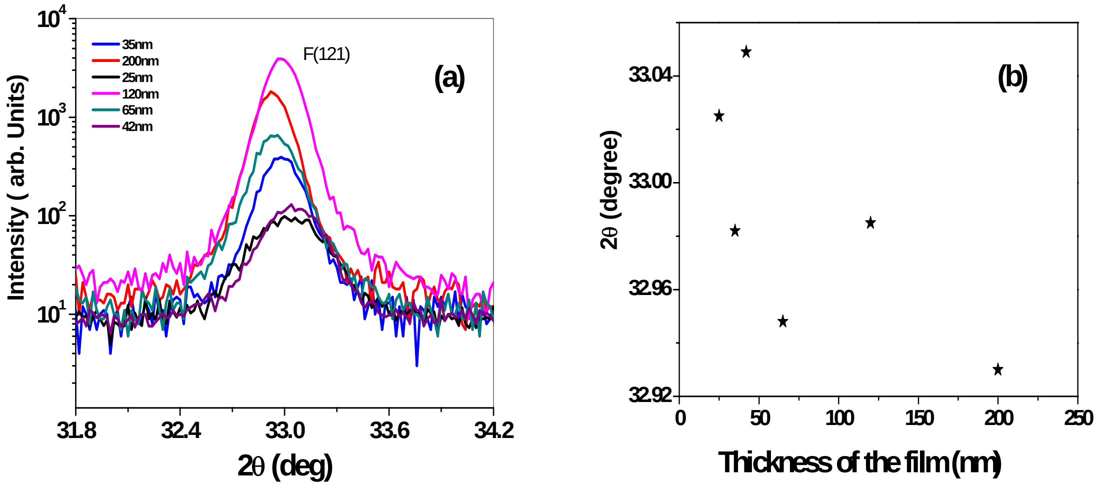

Fig. 3.2.8: *(a) High resolution XRD plot for the (121) peak position for all the thin films of PCMO (b) Variation of the peak position with film thickness obtained from the Gaussian fitting of the high resolution XRD data. Errors in 2θ are within the limit of ± 1.6 x* 10^{-3}.

It is well known that the interplanar spacing (d) is directly related to the 2θ value by the Bragg relation d=λ/(2sinθ) where λ is the x-ray wave length used for the XRD. The overall trend represented by an increase in d-value with the increase in film thickness is discernible from figure 3.2.8(b). This gives an impression of the relaxation of the lattice parameter for the films with higher values of thickness. The rocking curve measurements were also performed for the (121) peak position as shown in figure 3.2.9. Using the Lorentzian fitting, the variation of the Full Width at Half Maximum (FWHM) with increase in the film thickness is shown in figure 3.2.10. It is clear from the figure that the FWHM decreases with increase in film thickness, implying that thicker films have better crystallinity, assuming that the grain size effect is similar for all the films as the deposition parameters were kept nominally identical during the deposition of all the films.

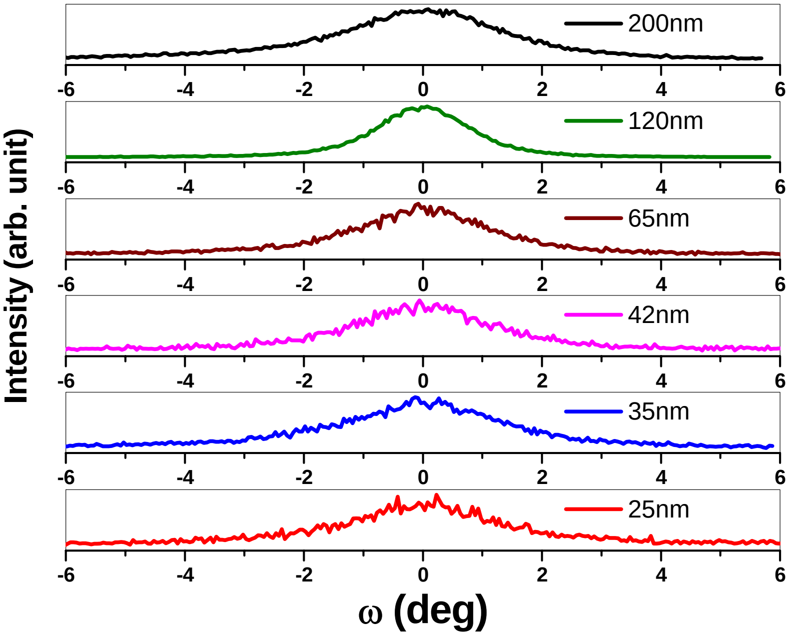

Fig. 3.2.9. *Rocking curve plot for all the PCMO films with thickness ranging from 25nm to 200nm.*

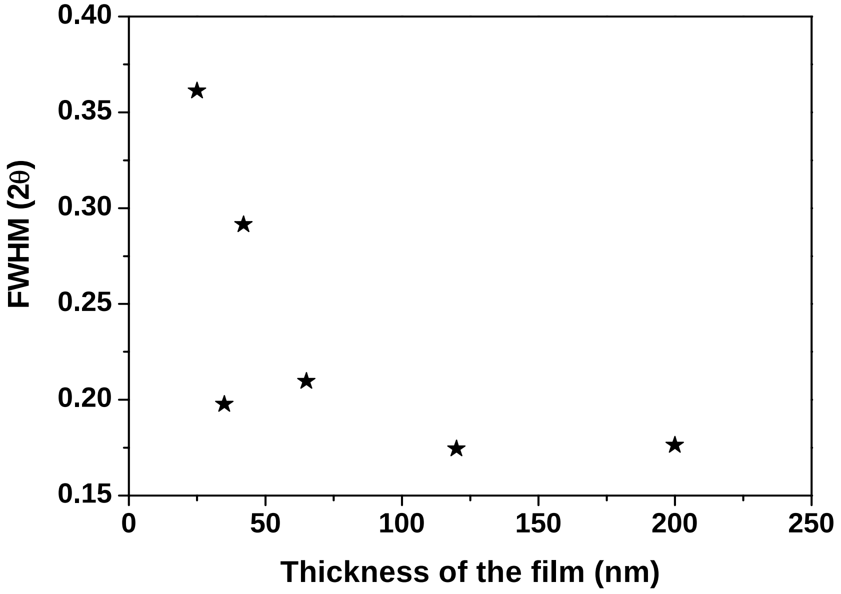

Fig. 3.2.10. *Variation of FWHM obtained from the Lorentzian fitting of the rocking curve data with film thickness. Errors in 2θ for all the films are within the limit of* $\pm 5.0 \times 10^{-3}$.

3.2.4 Discussion:

It is observed that the behavior of magnetoresistance for a PCMO thin film depends on its thickness. It may be noted that the MIT has not been observed by other workers in very thin films [13,17] of PCMO grown on STO substrates. On the other hand, thicker films show a field induced MIT and it has been observed that the MIT occurs for smaller fields when the thickness of the film is increased which is in stark contrast to the present observations. The unusual behaviour of the thin films observed in the present study appears to be on account of the fact that it is not the strain as such that is responsible for the CO melting in thin films but it is the strain relaxation, that leads to atomic scale disorder in the system, giving rise to the CO melting. So the very thin 'strained' films do not show CO melting whereas the 'strain relaxed' thicker films undergo CO melting under relatively small applied fields. The effect of strain relaxation on the CO melting has also been studied [17] by post-annealing the films, and a decrease in the CO melting field with increase in the annealing time has been reported. Also, an enhancement in CO melting temperature [19] has been reported in strained thin films grown on STO, which suggests the stabilization of CO with a tensile strain. Since MgO has a larger lattice mismatch (9.4%) with PCMO [3] compared to STO (+ 2.25 %), one can expect to observe a larger effect on the CO melting field for films grown on MgO. But we observed the CO melting only for films in a narrow thickness range and the CO melting field was observed to increase with increase in thickness, contrary to what is reported for films deposited on STO. According to our XRD results, the PCMO films have grown with a (121) orientation whereas those grown on STO are reported to have (010) orientation [13,17]. Hence one of the reasons for the difference between our results and those in the literature could be that the large strain that is calculated considering the *a* and *c* lattice parameters of PCMO is probably not present in our films due to the difference in the orientation of the film. There is a report of field induced MIT under the application of a magnetic field of 5 T for PCMO film with 200 nm thickness grown on MgO substrate [18]. But these films have (001) and (110) orientations as seen by the XRD. Hence, the orientation of the films may be playing a crucial role in controlling the strain and hence the CO melting. It is possible to have a small compressive strain, instead of the tensile strain as expected, in thin films formed with the (121) orientation. According to Yang *et. al*, [24] tensile strain (in PCMO films grown on STO) leads to an increase in T_{CO} whereas a compressive strain (in PCMO films grown on LAO) causes a decrease in T_{CO}. We have observed a decrease in $\mathrm{T_{CO}}$ with decrease in film thickness, for the films grown on MgO, from the analysis of the resistivity data. Resistivity, magnetoresistance and high resolution XRD data reveal a compressive strain in the films grown with (121) orientation. Additional experiments are required to understand the role of the microstructure, the exact nature of the strain and the relation between the effect of strain and CO melting in these films.

3.2.5 Summary:

$Pr_{0.5}Ca_{0.5}MnO_3$ films with thickness ranging form 25 to 200 nm were prepared by pulsed laser deposition technique. XRD measurements show (121) orientation for all the films studied. A decrease in resistivity and the charge order transition temperature is observed with decrease in the film thickness. A field induced insulator to metal transition corresponding to the charge order melting is observed for films with very small thickness (P35, P42). However, it appears that there is a range of film thickness (35 nm to 42nm in present study) for which CO melting is observed; films with thickness beyond this range do not exhibit MIT under applied magnetic fields upto 12 T. The film with 35 nm thickness exhibits a MIT even under zero field at low temperatures. The high resolution XRD data shows that d-spacing increases with increase in the thickness of the film which implies the relaxation of the lattice parameter due to the substrate induced strain for thicker film. It is suggested that the charge order melting and the observed variation in T_{CO} could be understood based on the strain relaxation effects arising from the (121) orientation of the PCMO films deposited on MgO substrates.

References:

[1] F. C. Wellstood, J. J. Kingston and John Clarke J. Appl. Phys. 75(2), 683 (1994)

[2] Rajiv K. Singh, D. Kumar Matt. Sci. & Engg. R22, 113 (1998)

[3] Julia M. Phillips J. Appl. Phys. 79(4), 1829 (1996)

[4] K. Scott, J. M. Huntley, W. A. Phillips, J. Clarke and J. E. Field Appl. Phys. Lett. 57, 922 (1990).

[5] D. H. Shin, J. Silcox, S. E. Russek, D. K. Lathrop, B. Moeckly and R. A. Buhrman Appl. Phys. Lett. 57, 508 (1990).

[6] E. Dagotto, T. Hotta and A. Moreo, Physics Reports, **344**, 1 (2001).

[7] G. Van Tendeloo, O. I. Lebedev, M. Hervieu and B. Raveau, Rep. Prog. Phys., **67**, 1315 (2004).

[8] A-M Haghiri-Gosnet and J-P Renard, J. Phys. D: Appl. Phys., **36**, R127, (2003).

[9] A. Asamitsu, Y. Tomioka, H. Kuwahara and Y. Tokura, Nature **388**, 50 (1997).

[10] V. Kiryukhin, D. Casa, J. P. Hill, B. Kelmer, A. Viglinate, Y. Tomioka and Y. Tokura, Nature **386**, 813 (1997).

[11] M. Rini, R. Tobey, N. Dean, J. Itatani, Y. Tomioka and Y. Tokura, Nature **449**, 72 (2007).

[12] T A Kaplan and S D Mahanti (Ed.) Kluwer Academic Publishers1999, pp155.

[13] Z. Jirák, F. Damay, M. Hervieu, C. Martin, B. Raveau, G. André and F. Bourée, Phys. Rev. B, **61**, 1181 (2000).

[14] W. Prellier, E. Rauwel Buzin, B. Mercey, Ch. Simon, M. Hervieu, and B. Raveau, J. Phys. Chem. Solids, **64**, 1665 (2003).

[15] Y. Tomioka, A. Asamitsu, H. Kuwahara, Y. Moritomo and Y. Tokura, Phys. Rev. B, **53**, R1689 (1996).

[16] M. Tokunaga, N. Miura, Y. Tomioka, Y. Tokura, Phys. Rev. B, **57**, 5259 (1998).

[17] Z. Q. Yang, R. W. A. Hendrikx, P. J. M. v. Bentum and J. Aarts, Europhys. Lett., **58** (6), 864 (2002)

[18] H. Yamamoto, T. Murakami, J. Sakai and S. Imai, Solid State Commun., **142**, 28 (2007).

[19] Y. Q. Zhang, Y. L. Zhu, Z. D. Zhang and J. Aarts, J. Appl. Phys., **101**, 063919 (2007)

[20] S.de Brion, G.Chouteau, A.Janossy, E.Rauwel Buzin and W.Prellier, J. of Magn. Magn. Mater, **272–276**, 450 (2004).

[21] W. Prellier, Ch. Simon, A. M. Haghiri-Gosnet, B. Mercey, and B. Raveau, Phys. Rev. B, **62**, R16337 (2000).

[22] W. Prellier, A. M. Haghiri-Gosnet, B. Mercey, Ph. Lecoeur, M. Hervieu, Ch. Simon and B. Raveau, Appl. Phys. Lett. **77**, 1023 (2000).

[23] A. M. Haghiri-Gosnet, M. Hervieu, Ch. Simon, B. Mercey, and B. Raveau, J. Appl. Phys., **88**, 3545 (2000).

[24] Z. Q. Yang, Y. Q., Zhang, J. Aarts, M. Y. Wu and H. W. Zandbergen, Appl. Phys. Lett., **88**, 072507 (2006).

Chapter 4

Current Induced Charge Order Melting and Its Effect on T_c of YBCO in PCMO/YBCO Bilayer Film

4.1 Introduction:

In general ferromagnetism is known to be detrimental to superconductivity [1] and therefore the coexistence of these two antagonistic phases is rarely seen in the bulk form. However, recent development of artificially fabricated thin film heterostructures has made it possible to bring the ferromagnetic (FM) phase in close proximity to the superconducting (SC) phase. The interplay of these two phases has resulted in exotic phenomena such as oscillation of superconducting transition temperature (T_C), domain wall superconductivity [2-5] etc. These phenomena are interesting from the point of view of basic research to understand the mechanism of high temperature superconductivity (HTSC), and also offer the possibility of potential technological applications in the areas such as spintronics [6,7]. In FM/SC thin film heterostructures, superconductivity can be influenced mainly by two mechanisms: first is the direct proximity effect involving leakage of Cooper pairs inducing weak superconductivity across the interface and the second is the injection of quasiparticles into the superconducting layer which results in the suppression of the superconducting energy gap. The details of these phenomena are discussed in the introduction chapter. Manganites constitute a class of materials which can be used for the fabrication of FM/SC heterostructures in conjunction with SC films made of high-T_C cuprate superconductor [8-13] with a view to investigate such effects.

$Pr_{1-x}Ca_xMnO_3$ is a hole doped manganite [14] which exhibits a highly insulating charge ordered phase for $0.3 \leq x \leq 0.7$. The onset of charge ordering temperature (T_{CO}) is measured to be ~ 240K for x = 0.5. It is also observed that charge ordered insulating phase of $Pr_{1-x}Ca_xMnO_3$ can transform to a conducting FM phase by application of external variables like magnetic and electric field, substrate induced strain, photon exposure etc [15-18]. In the 3rd chapter it has been shown that substrate (like MgO) induced strain plays a crucial role for the melting of charge ordered $Pr_{0.5}Ca_{0.5}MnO_3$ into a metallic ferromagnetic $Pr_{0.5}Ca_{0.5}MnO_3$ in thin film form. Thus a $Pr_{0.5}Ca_{0.5}MnO_3$ (PCMO) thin film placed in close proximity to a $YBa_2Cu_3O_7$ (YBCO) thin film to form a FM/SC heterostructure can be used for investigations of a variety of interesting physical phenomena. In this chapter, the current and magnetic field induced charge order melting of the upper PCMO layer is carried out. The charge order melted PCMO layer leads to the formation of FM clusters which, in turn, affects the superconductivity of the YBCO layer lying underneath.

4.2 Experimental Details:

The bulk polycrystalline target materials of $Pr_{0.5}Ca_{0.5}MnO_3$ (PCMO) and $YBa_2Cu_3O_7$ (YBCO) used for the preparation of thin films were synthesized by the standard solid state reaction method [18], as described in the 2nd chapter. Thin film of YBCO with a thickness of ~100 nm has been grown on (100) oriented $LaAlO_3$ (LAO) substrate by the pulsed laser deposition technique. A second layer of PCMO film with a thickness of ~100 nm was grown in situ on top of the YBCO layer. KrF excimer laser (wave length: 248 nm) with a fluence of ~ 1.2 J/cm^2 and pulse repetition rate of 5 Hz was used for the preparation of the bilayer. The laser deposition was carried out under an oxygen pressure of 0.33 mbar and 0.17 mbar with a flow rate of 40 sccm and 26 sccm respectively for the deposition of YBCO and PCMO films. A pre-deposition base pressure of 2.2×10^{-5} mbar was achieved in the chamber using a turbo-molecular pump. The substrate temperatures were maintained at 840 C and 800 C for the deposition of YBCO and PCMO film respectively based on the results of earlier experimental runs to optimize the deposition parameters. The substrate to target distance was maintained at 4 cm during deposition.

After the deposition, the film was allowed to cool rapidly from 800 C to 450 C in 30 minutes and subsequently it was annealed at 400 C for one and half hours, before rapid cooling to room temperature within a further period of 30 minutes.

The total thickness of the bilayer film was measured by DEKTAK 3030A surface profiler, whereas the individual layer thicknesses were estimated based on the number of laser shots and prior calibration runs on the deposition of the corresponding individual single layers while maintaining the identical deposition parameters. The thickness of each layer was estimated to be 100 nm. The crystal structure and the orientation of the film were characterized by X-ray diffraction (XRD) measurements in an STOE diffractometer using CuK_α radiation. Electrical resistivity measurements were carried out in the temperature range 4.2 to 300 K using four probe technique at different measuring currents ranging from 10µA to 40mA. Magnetoresistance (MR) measurements were carried out on the bilayer sample under magnetic fields upto 12T with different applied current (10 µA to 40 mA). A calibrated cernox resistance thermometer was used for temperature measurements in the presence of magnetic field.

4.3 Results and Discussion:

XRD pattern of the bilayer film is shown in Fig. 4.1**.** The peaks corresponding to YBCO, PCMO and LAO have been labeled as Y, P and L respectively. It is evident from fig.4.1 that a fully *c*-axis oriented YBCO film has been grown on LAO substrate whereas the PCMO peaks are very close to the peaks corresponding to LAO. It may also be noted that the b-axis of the PCMO film is perpendicular to the a-b plane of the LAO substrate. To distinguish the PCMO and LAO peaks, the XRD pattern near the (*040*) and (*060*) reflections of PCMO has been expanded and shown in Fig.4.1 (b).

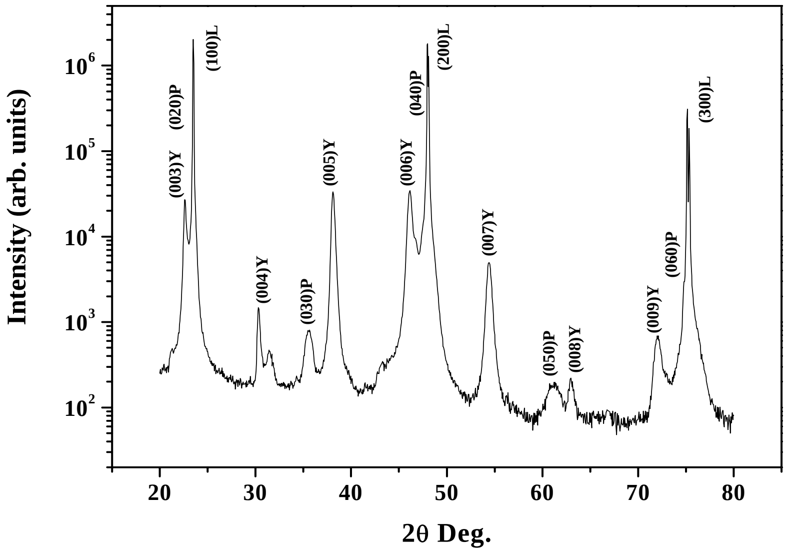
Intensity (arb. units)
10^6
10^5
10^4
10^3
10^2
2θ Deg.
20
30
40
50
60
70
80
(003)Y
(020)P
(100)L
(004)Y
(030)P
(005)Y
(006)Y
(040)P
(200)L
(007)Y
(050)P
(008)Y
(009)Y
(060)P
(300)L

(a)

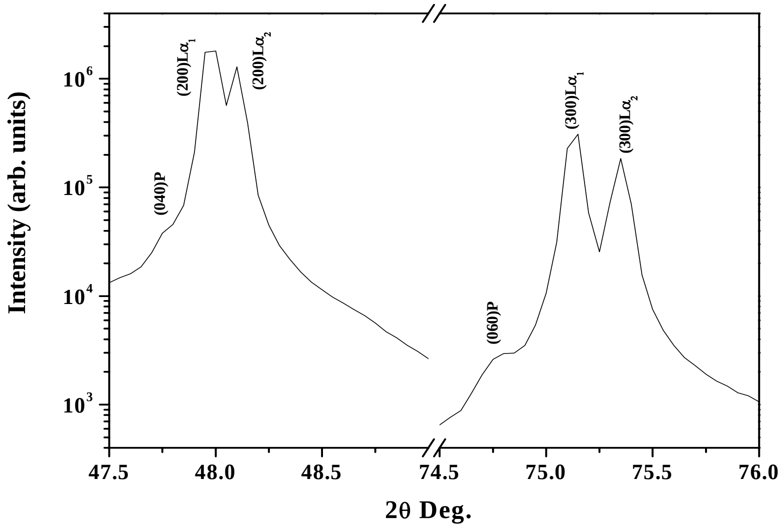
Intensity (arb. units)
10^6
10^5
10^4
10^3
2θ Deg.
47.5
48.0
48.5
74.5
75.0
75.5
76.0
(040)P
(200)Lα1
(200)Lα2
(060)P
(300)Lα1
(300)Lα2

(b)

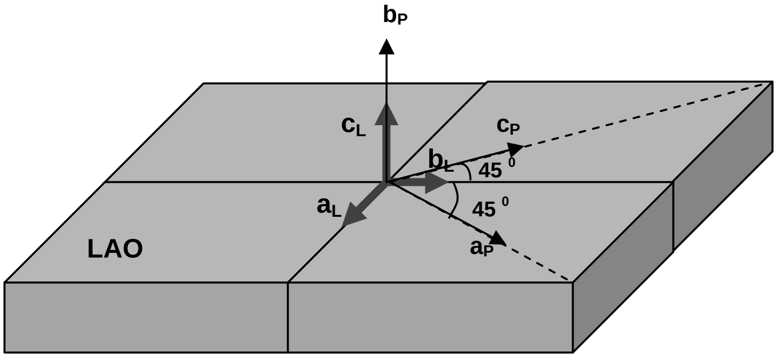

(c)

Fig. 4.1. *(a) XRD pattern of the PCMO/YBCO bilayer on LAO substrate. The peaks corresponding to YBCO, PCMO and LAO are labelled as Y, P and L respectively. (b) A magnified plot of the part of the XRD pattern indicating (040) and (060) peaks of PCMO as well as (200) and (300) peaks of LAO. (c) The dependency upon the [hkl] orientation of PCMO thin film in relation with the lattice mismatch values. Here* a_L, b_L, c_L *are the a, b, c crystal axes respectively for LAO whereas* a_P, b_P, c_P *are the a, b, c crystal axes respectively for PCMO.*

.

The crystal axes ‘a’ and ‘c’ of PCMO may be rotated through 45^0 relative to the crystal axes ‘a’ and ‘b’ of the LAO substrate to minimize the lattice mismatch. [18,19]. In this orientation, the lattice mismatch turns out to be much smaller (~ -0.75%) if the crystal axes “a” and “b” of PCMO are rotated through an angle of 45° relative to the crystal axes “a” and “b” of the LAO substrate. A schematic figure for the [hkl] orientation of PCMO thin film in relation with the lattice mismatched LAO substrate has been given in figure 1(c).

The results of the temperature dependent resistance R(T) measurements at the magnetic fields (H) of 0T, 6T and 12T are shown in fig. 4.2, fig. 4.3 and fig. 4.4 respectively. Figure 4.2 shows the evolution of R(T) behaviour under the application of different measuring currents ranging from 1 mA to 40 mA at H= 0 T. For 10 μA to 1 mA the resistance curve do not change.

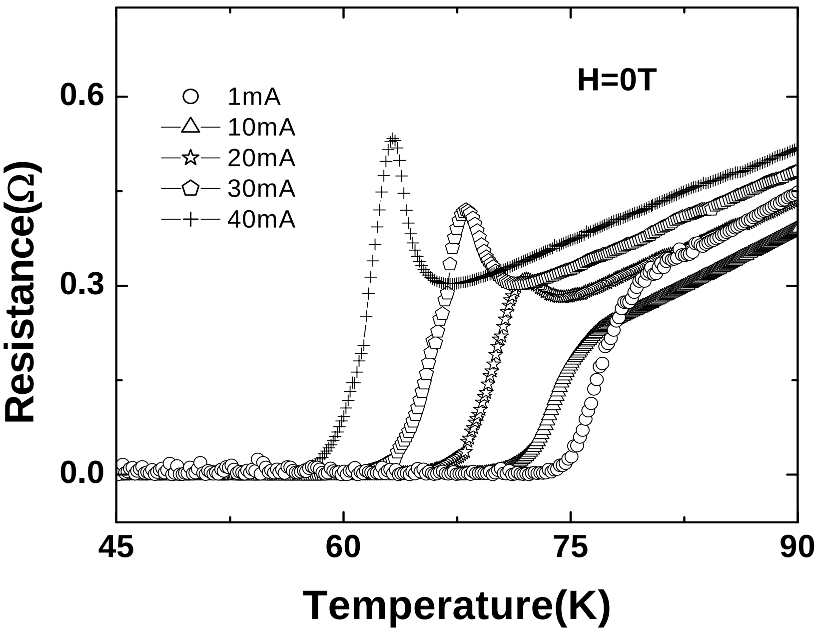

Fig. 4.2. *Temperature dependent resistance at H=0T for different applied current ranging from 1mA to 40mA. Note increasing resistance before the fall at* T_C.

It may be noted that for currents up to 1mA, the superconducting transition temperature (T_c) remains almost the same, beyond which the T_c is gradually reduced with increasing current. A hump like feature is observed just above the onset of the superconducting transition, whose height progressively increases with increase in the current. It is interesting to note that, as shown in fig.4.3, the hump height is reduced when a magnetic field of 6 T is applied; indeed, the hump like feature gets almost suppressed with further increase in field to 12T, as shown in fig. 4.4.

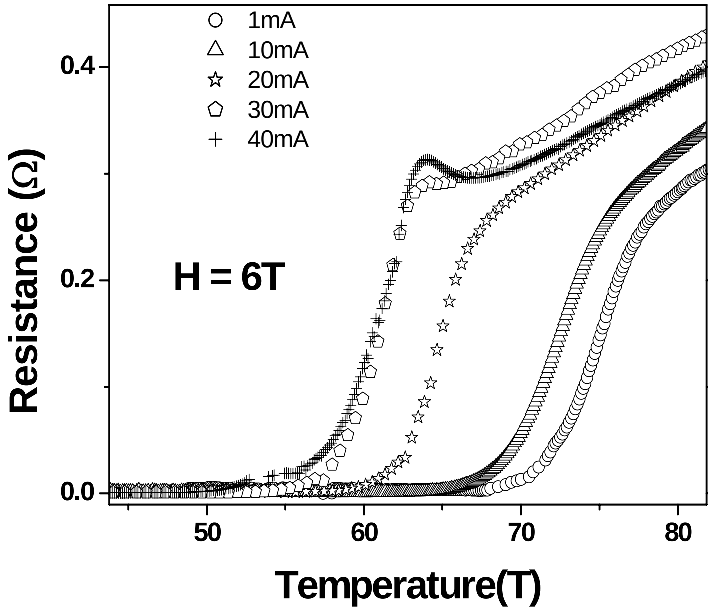

Fig. 4.3. Temperature dependent resistance at H=6 T for different applied current ranging from 1mA to 40 mA.

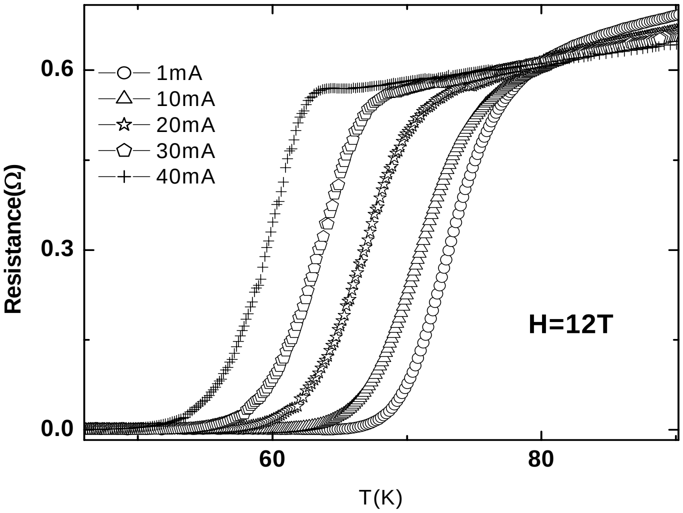

Fig. 4.4. Temperature dependent resistance at H=12 T for different applied current ranging from 1mA to 40 mA.

The various important findings which emerge from these measurements may be summarized as follows: (i) there is no shift in T_c up to a measuring current of 1mA; (ii) T_c progressively decreases with a further increase in current; (iii) a hump like feature is observed in the R(T) curve with increase in measuring current beyond 20 mA at 0 T; (iv) the hump like feature is gradually suppressed with increase in magnetic field at a fixed measuring current (see fig.4.2, 4.3 & 4.4); (v) there is no appreciable shift in the onset of T_c under the application of a magnetic field for a fixed measuring current; (vi) MR is found to be positive. These observations are explained on the basis of current induced partial charge order melting in the PCMO thin film and the injection of quasi-particles in YBCO. It is known that an electric field can induce insulator-metal transition (MIT) in PCMO thin films. By an analogy with the random field Ising and Heisenberg models [14], near a first order phase transition, two competing states can coexist by forming clusters of variable size depending on the value of the random field. In PCMO thin film, an electric current driven disordering mechanism brings about the competition between CO and FM phases which may lead to the formation of clusters of one phase dispersed in a matrix of the other. Here it is assumed that the FM and CO phases remain randomly oriented and isolated from each other upto the maximum current applied (~40 mA) as shown schematically in fig. 4.5 (a). In this figure the FM clusters are shown as darkly shaded regions over the uniform CO background.

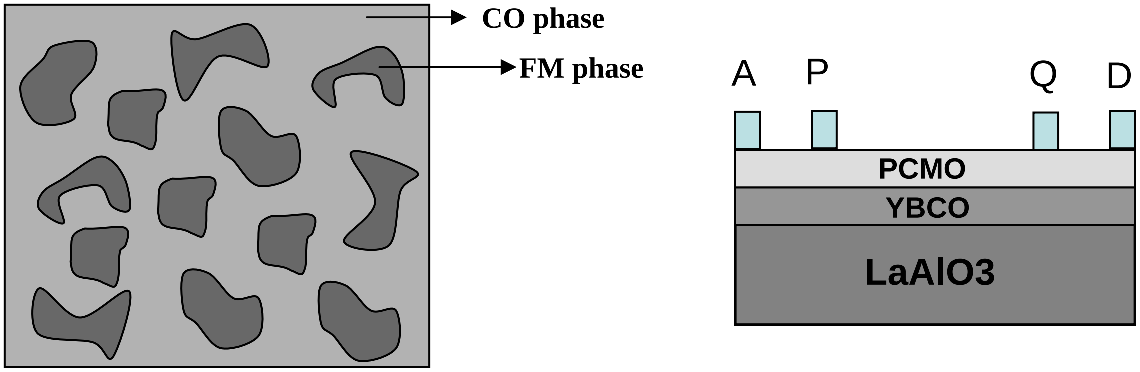

(a) (b)

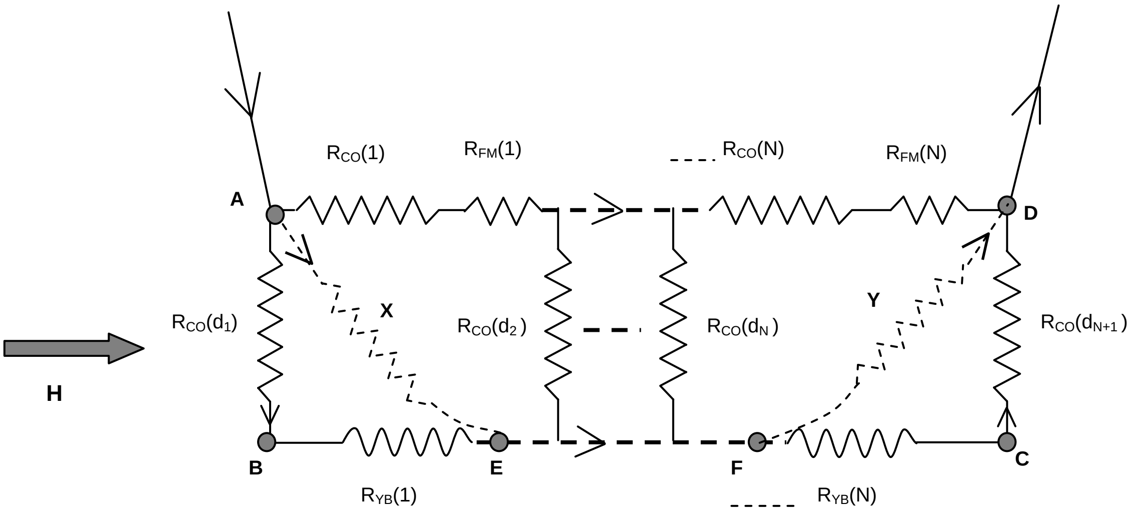

(c)

Fig. 4.5. *(a) Schematic illustration of FM clusters dispersed in a CO background of the PCMO film expected to form under the application of externally applied current (b) schematic cross-section of the PCMO/YBCO bilayer heterostructure deposited on LAO substrate indicating the contact points and (c) the schematic equivalent resistance circuit at a fixed applied current corresponding to (a).*

These FM clusters can grow in size with increase in applied magnetic field or current. Let us now concentrate on the schematic diagram of the bilayer film (see fig.4.5 (b)). Here current is passed through the contacts A and D, while the voltage is measured across the contacts P and Q. The top PCMO film can be modeled as a series of interconnected network of N charged ordered regions having a relatively high resistance and N low resistance FM clusters as shown schematically in fig. 4.5 (c). The values of these resistances between the contacts A and D are denoted as $R_{CO}(i)$ and $R_{FM}(i)$ (i=1 to N) respectively as shown in figure 4.5(c). In this figure, B-E-F-C denotes the low resistive path through the YBCO film which is also modeled to be comprised of N resistances $R_{YB}(i)$, connected in series. In this schematic, there are N parallel resistive paths between the lines AD and BC traversing through the thickness of PCMO (ie perpendicular to the surface of the film) whose values are denoted as R_{CO} (d_i). As the value of R_{CO} is much greater than that of R_{FM} and R_{YB}, we can neglect the current flowing through the intermediate high resistive paths namely R_{CO} (d_2) to R_{CO}(d_N) etc for simplicity. The effective resistance between the contacts A and D is then given by

$$R_{result} = \frac{(NR_{CO} + NR_{FM})(2R_{CO} + NR_{YB})}{(N+2)R_{CO} + NR_{CO} + NR_{YB}} \qquad \text{-----------------------------}\mathbf{(1)}$$

As N>>1 and near T_c, (R_{CO} + R_{FM})> R_{YB} , the above equation may be simplified as

$$R_{result} = 2R_{CO} + NR_{YB} \qquad \text{---------------------------}\mathbf{(2)}$$

Thus, $\mathbf{R_{result}}$ turns out to be the resultant resistance along the path A-B-E-F-C-D as shown in fig. 4.5 (c). On the basis of this model, all of our experimental observations can be explained as follows; **(i)** The fact that R(T) exhibits very little change for measuring currents up to ~ 1mA may be taken to imply that CO melting does not occur up to this value of current and thus there is no formation of FM clusters inside the PCMO film. Due to the absence of the FM phase, there is no significant proximity effect related shift in T_c as experimentally observed. **(ii)** As the current is increased beyond 1mA, the charge order melting begins which leads to the formation of tiny FM clusters. These clusters further grow in size with the increase in current. It may be noted that the increase in current has two prominent deleterious effects on the superconductivity of YBCO. Firstly, the proximity of FM clusters which grow under the influence of increased current suppresses the T_C of the bilayer on account of exchange field effect. Secondly, there will be an injection of quasi particles emanating from metallic FM clusters into the YBCO layer. It is known that the quasiparticle density (n_{qp}) increases with increasing current following the expression $n_{qp} = J_{inj}\tau_{eff}/et$, where τ_{eff} is the effective quasiparticle recombination time and t is the thickness of the perturbed region of YBCO and J_{inj} is the injected current density [20,21]. The superconducting order parameter decreases monotonically with increasing n_{qp} as shown by the relation, $\Delta(n_{qp})/\Delta(0) = 1- 2n_{qp}/4N(0)\Delta(0)$, where $N(0)$ is the single-spin density of states in the superconductor, $\Delta(n_{qp})$ is the perturbed energy gap and $\Delta(0)$ is zero temperature energy gap. Combining the two equations we get $d\Delta/d J_{inj} \approx -\tau_{eff} /2eN(0)t$ and we see that superconducting energy gap in the thin film decreases with increasing injection current which in turn decreases the T_c of the superconductor. Hence increase in current results in a decrease of T_c. The possibility of the T_c suppression due to current induced heating effect could be ruled out in this study on the basis of following observations: First, the current dependent R(T) measurements have been performed on the YBCO single layer (100 nm thick) under similar conditions, which reveal much smaller shift in T_c than that observed for the bilayer film. The comparison of T_c vs current for the single layer YBCO film as well as the bilayer YBCO/PCMO film are shown for H = 0 T and 12 T in fig. 4.6. It is evident from fig.4.6 that the rate of suppression of the T_C with current is much higher in the bilayer film compared to that in the single layer YBCO film.

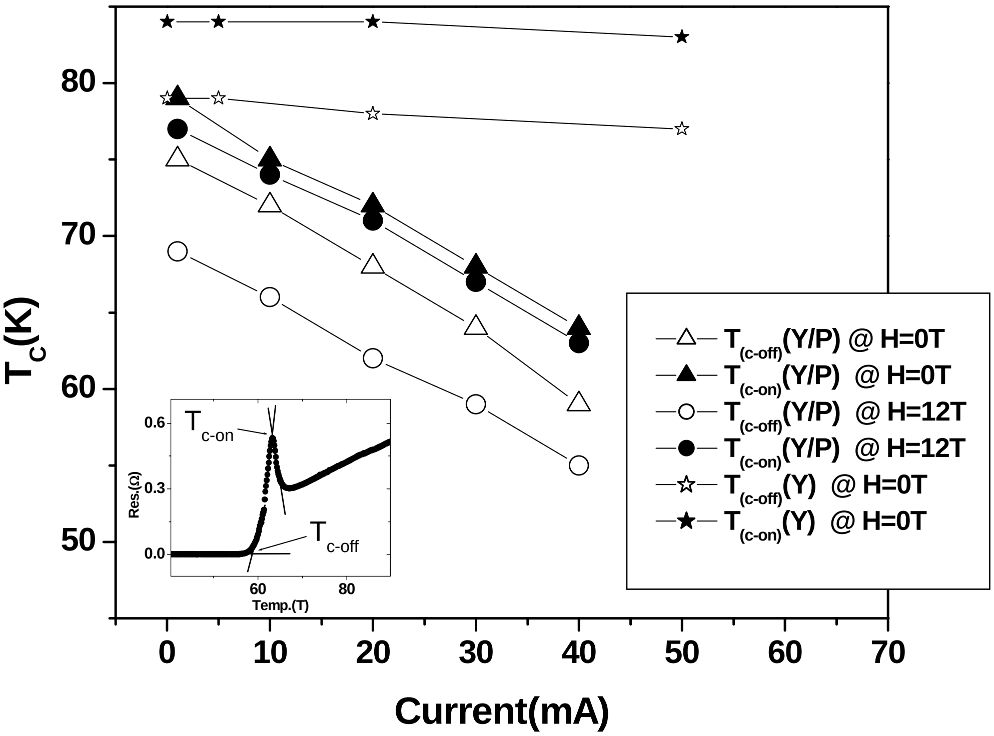

Fig. 4.6. *T_C vs applied current for a single layer YBCO (denoted as Y) and PCMO/YBCO bilayer (denoted as Y/P) for H=0 T and H=12 T field. $T_{(c\text{-}on)}$ and $T_{(c\text{-}off)}$ represent the onset and offset transition temperatures measured as shown in the inset.*

Second, the resistance of the bilayer film at three fixed temperatures of 10 K, 20 K and 40 K has been measured with increase in current. It is seen that up to a current of 25 mA, the temperature remains constant within ± 1 mK of the fixed temperature. This implies that the heating effect is not significant up to a current of 25 mA. For currents in the range of 25 mA – 40 mA, the change in temperature is found to be only ~ 0.2 K. However, the temperature is seen to increase by 0.8 K above the fixed temperature as the current is increased to 60 mA. (iii) From Eq. 2, we can write the temperature derivative of $\mathbf{R_{result}}$ as

$$\frac{dR_{result}}{dT} = 2\frac{dR_{CO}}{dT} + N\frac{dR_{YB}}{dT} \qquad \text{-----------------(3)}$$

Eq. 3 shows that near T_c the rate of change of resultant resistance is primarily dictated by the competition between the rate of change of resistances of PCMO and YBCO layers. At low temperatures just above T_c, $dR_{CO}/dT >> dR_{YB}/dT$**.** Under these circumstances, the temperature dependence of R_{result} is mainly dominated by the temperature dependent changes in R_{CO} and the negative temperature coefficient of resistance of R_{CO} causes a sudden rise in resistance near T_c resulting in a hump like feature. It is also clear that for higher applied current the T_c gets further suppressed to lower temperatures and thus dR_{CO}/dT continues to dominate to still lower temperatures. This results in a progressive increase in the hump height observed at higher applied currents. (**iv)** Application of higher magnetic field at a given current favors the growth of metallic FM clusters in the PCMO film which decreases the overall R(T) of PCMO film. This, in effect, decreases R_{CO} when a magnetic field is applied and ultimately results in a decrease of hump height. It is believed that the decrease of hump height observed at higher magnetic field arises on account of this effect. **(v)** Our magnetoresistance measurements on single layer YBCO film reveal that there is little change in T_c up to a field of 12 T. Thus it appears that in the case of FM /SC heterostructure, there is a possibility of injection of the spin polarized quasi-particles into the SC layer with increase in the magnetic field which strongly suppresses the $T_{c.}$ However, Gims et. al [20] have indicated that a well defined special geometry and very clean interface are required for spin injection to take place. In fact in most of the experiments, there is only ordinary quasi-particle injection. It may be noted that our bilayer geometry does not favor the spin injection and hence the influence of magnetic field on T_c of the underlying YBCO remains negligibly small (similar to that observed in the single layer YBCO). **(vi)** The positive MR (shown in fig. 4.7) for constant current can also be explained by the above model.

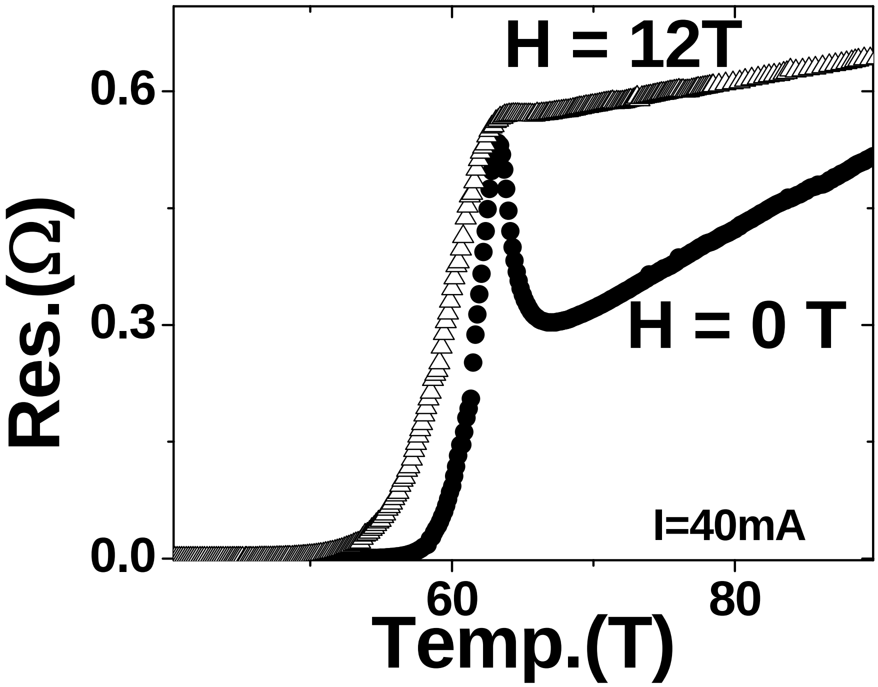

Fig. 4.7. *Comparison of MR data for two different values of applied magnetic field H=0T and H=12T at a fixed applied current I=40mA.*

During these measurements, the magnetic field (H) has been applied parallel to the plane of the film (see fig. 4.5 (c)), i.e., perpendicular to the resistive paths along A-B and C-D. In this situation, the charge carriers have to travel a virtually longer length in PCMO film as represented schematically by the paths A-X-E and F-Y-D in fig. 4.5(c). This effectively results in higher resultant resistance $\mathbf{R}_{\mathbf{result}}$ on application of a magnetic field giving rise to a positive MR for higher magnetic fields at a constant current.

4.4 Conclusion:

A bilayer thin film of YBCO and PCMO has been deposited on LAO substrate by pulsed laser deposition technique. The MR experiment has been performed with different values of applied current. Based on the results of these measurements, it is inferred that the charge order melting of PCMO is initiated for I> 1 mA at H = 0 T leading to the formation of isolated tiny clusters of the ferromagnetic phase. The size of these FM clusters increases with increase in the magnitude of applied current. The T_c of the underlying YBCO layer is thus suppressed by the proximity of the FM clusters and by injection of quasi-particles emanating from the top PCMO layer. Although there is little change in T_c with increasing magnetic field at a given value of applied current, a positive MR is observed with increasing field.

References:

[1] Ginzburg, V. L. Zh. Exsp. Teor. Fiz 31, 201 (1956)

[2] A. I. Buzdin, Rev. Mod. Phys. 77, 935 (2005)

[3] F. S. Bergeret, A. F. Volko, and K. B. Efetov, Rev. Mod. Phys. 77, 1321 (2005)

[4] W. Gillijns, A. Yu. Aladyshkin, M. Lange, M. J. Van Bael, and V. V. Moshchalkov, Phys. Rev. Lett. 95, 227003 (2005)

[5] Z. Yang, M. Lange, A. Volodin, R. Szymczak, and V. Moshchalkov, Nature Mat. 3, 793 (2004)

[6] S. A. Wolf, D. D. Awschalom,R. A. Buhrman, J. M. Daughton, S. Von Molnar, M. L. Roukes, A. Y. Chtchelkanova, and D. M. Treger, Science 294,1488 (2001)

[7] G. A. Prinz, Science 282, 1660 (1998)

[8] Daniel Hsu, L. G. Lin, C. P. Chang, C. H. Chen, C. H. Chiang, W. C. Chan and W. F. Wu *JAP 103, 07C710 (2008)*

[9] J. G. Lin, Daniel Hsu, W. F. Wu, C. H. Chiang and W. C. Chang *JAP 101, 09G106 (2007)*

[10] Hanns-Ulrich Habermeier, Soltan Soltan and Joachim Albrecht *Physica C 460-462, 32(2007)*

[11] J. G. Lin, S. L. Cheng, C. R. Chang and D. Y. Xing *JAP 98, 023910(2005)*

[12] Daniel Hsu, L. G. Lin, C. P. Chang, C. H. Chen, W. F. Wu,C. H. Chiang and W. C. Chan *APL 90, 162504(2007)*

[13] W. Westhauser, S. Schramm, J. Hoffmann and C. Jooss *Eur. Phys. J. B 53, 323(2006)*

[14] Elbio Dagotto, *Nanoscale Phase Seperation and Colossal Magnetoresistance: The Physics of Manganites and Related Compounds*, May27, 2002, Springer-Verlag

[15] A. Asamitsu, Y. Tomioka, H. Kuwahara and Y. Tokuta, Nature **388**, 50 (1997).

[16] V. Kiryukhin, D. Casa, J. P. Hill, B. Kelmer, A. Viglinate, Y. Tomioka and Y. Tokura, Nature **386**, 813 (1997).

[17] W. S. Tan, L. Yang, X. S. Wu, S. S. Jiang, T. L. Kam, J. Gao, J. Wang and Z. H. Wu *Physica C 384, 437 (2003)*

[18] D. K. Baisnab et al. *JMMM 323, 2823 (2011)*

[19] D Samal and P S Anil Kumar *J. Phys.: Condens. Matter 21, 492203 (2009)*

[20] Y. Gim, A. W. Kleinsasser, and J. B. Barner *JAP Vol.90, No. 8, 4063 (2001)*

[21] Awadhesh Mani, T. Geetha Kumary, Daniel Hsu and J. G. Lin *JAP 105, 103915 (2009)*

Chapter 5

Effect of Charge Order Melting on Superconducting Properties (T_c and J_c): Studies on Partially Masked PCMO/YBCO Bilayer Film

5.1 Introduction:

The co-existence of superconductivity and ferromagnetism in bulk compounds is rarely possible because the ferromagnetic exchange field prevents the formation of Cooper pairs by electrons with antiparallel spin orientation [1,2]. The artificially grown thin film superconductor/ferromagnet heterostructures present a unique opportunity to investigate the interplay between these two competing long range order phenomena and open up a new avenue for the development of the spin injection devices [3-8]. In such S/F hybrid devices, superconductivity is influenced by two distinct quantum mechanical effects viz., the proximity effect and the injection of spin polarized charge carriers into the superconductor. In the case of proximity effect, superconductivity and ferromagnetism coexist within a very short distance from the interface of the order of the induced superconducting correlation length, ξ_F [9] and the superconducting order parameter oscillates in the vicinity of the interface. On the other hand, the quasi-particle spin injection effect perturbs the order parameter within the spin-diffusion length, ξ_{FM} [10]. Both these effects are known to generally weaken superconductivity by suppressing the superconducting order parameter.

In the previous chapter, investigations on suppression of superconductivity in a superconducting thin film of $YBa_2Cu_3O_7$ (YBCO) placed in close proximity to a thin film of the charge ordered manganite $Pr_{0.5}Ca_{0.5}MnO_3$ (PCMO) were described; this suppression was the result of formation of ferromagnetic clusters in PCMO under the influence of an experimental control variable in a charge ordered matrix of $Pr_{0.5}Ca_{0.5}MnO_3$ (PCMO). It was observed that with the increase of applied current and magnetic field, the T_c of the PCMO/YBCO heterostructure was suppressed. To investigate these effects further, another PCMO/YBCO heterostructure has been deposited on $SrTiO_3$ (STO) substrate where about half of the bottom YBCO layer was deliberately not covered by the PCMO film by suitable masking techniques. The electrical transport measurements performed on this heterostructure in the presence of an applied magnetic field revealed a suppression of the superconducting properties of the uncovered YBCO portion which is not in direct electrical contact with the PCMO layer. These experimental results demonstrate the potential of developing spin injection based devices where the superconducting properties of YBCO thin film can be controlled by nucleating ferromagnetic clusters in a PCMO thin film under the influence of a suitable control variable even when the two regions are not in close proximity.

5.2 Experimental Details:

Stoichiometric polycrystalline $Pr_{0.5}Ca_{0.5}MnO_3$ (PCMO) and $YBa_2Cu_3O_7$ (YBCO) target materials were used for the growth of YBCO/PCMO bilayer thin films by the pulsed laser deposition technique. The target materials were synthesized by the standard solid state reaction method [11] as described in chapter 2. The bilayer heterostructure was grown on (100) oriented $SrTiO_3$ (STO) substrate by the pulsed laser deposition technique. Thin film of YBCO with a thickness of ~80nm was grown on STO substrate as a first layer. A second layer of PCMO film with a thickness of ~80 nm was then grown in-situ on top of YBCO layer. An in-situ shadow mask was used to get a specimen where nearly half of the YBCO thin film was covered by the PCMO (see the schematic figure 5.1(a)).

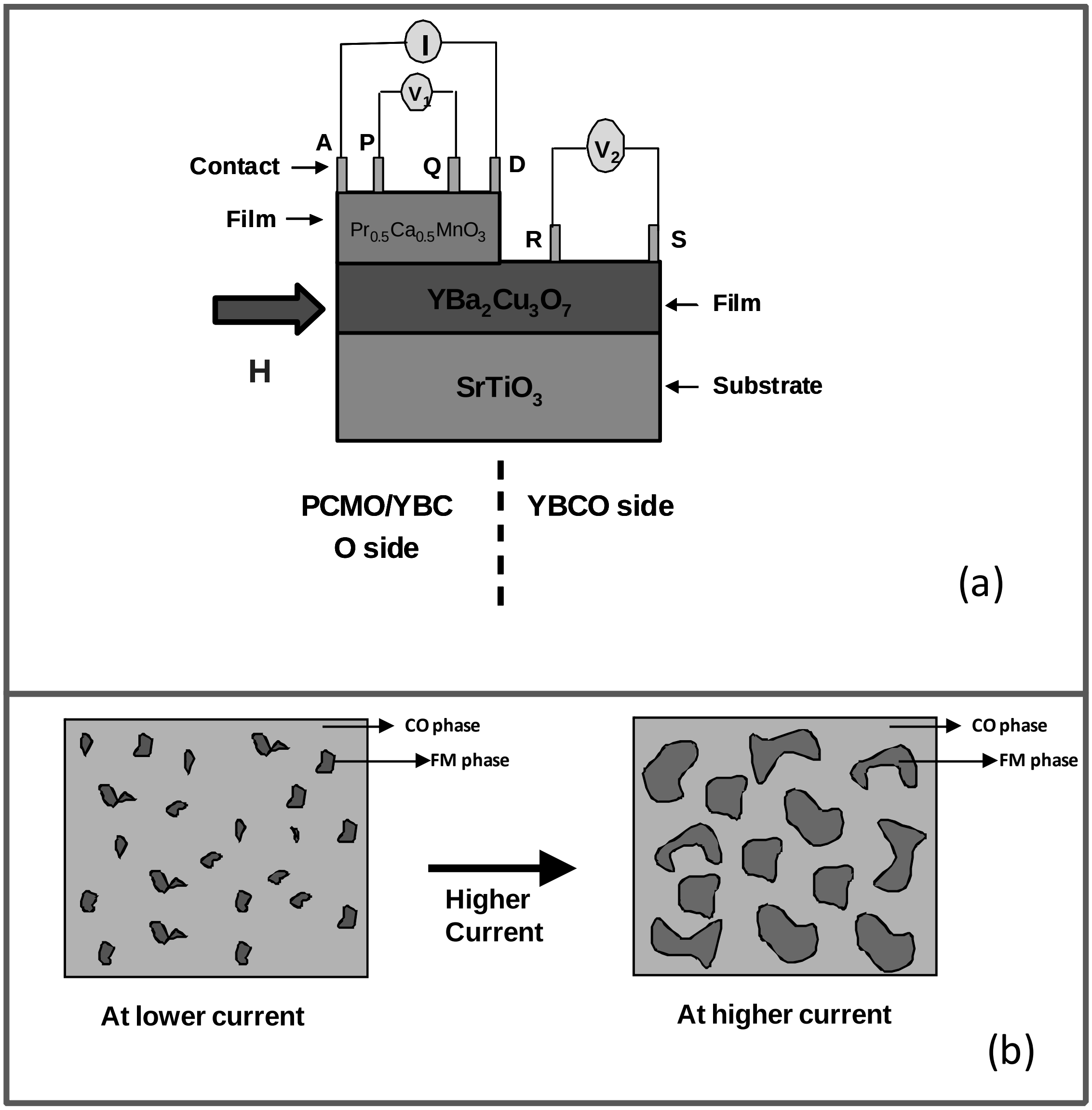

Fig. 5.1. *(a) schematic cross-section of the PCMO/YBCO bilayer heterostructure deposited on STO substrate where about half of the bottom YBCO layer is not covered by PCMO layer. The contact points are indicated by the letters A,P,Q,D,R and S (b)Schematic illustration of FM clusters dispersed in a CO background of the PCMO film, which are expected to grow under the application of an external current or magnetic field..*

Pulsed laser deposition was carried out using a KrF excimer laser (wave length: 248nm) with a fluence of ~ 1.2 J/cm^2 and a pulse repetition rate of 5Hz for the preparation of the bilayer. An oxygen pressure of 0.33 mbar and 0.17 mbar, with a flow rate of 26 sccm and 18 sccm, was used for the deposition of the YBCO and PCMO films respectively. A pre-deposition base pressure of 1.8 × 10^{-5} mbar was achieved in the chamber using a turbo-molecular pump. The substrate temperatures were maintained at 840 C and 800 C for the deposition of YBCO and PCMO film respectively based on the results of earlier experimental runs to optimize the deposition parameters. The substrate to target distance was maintained at 4 cm during the deposition. After the deposition, the film was annealed at 400 °C for one and a half hours, before rapid cooling to room temperature. The thickness of the bilayer film was measured by DEKTAK3030A surface profiler. The crystal structure and the orientation of the film were characterized by X-ray diffraction (XRD) measurements in an STOE diffractometer using CuK_{α} radiation. Electrical resistivity measurements were carried out in the temperature range 4.2 to 300 K using four probe technique at different measuring currents ranging from 10 μA to 40 mA. Resistance vs temperature measurements were carried out on the sample under magnetic fields upto 12T and with different applied currents from 10 μA to 40 mA. The applied current was injected on the YBCO/PCMO bilayer side using the current contacts A and D and the resistance of the film was measured at two different locations on the film by measuring the potential difference across the contacts P and Q for the YBCO/PCMO bilayer and the contacts R and S for the part of the YBCO film which was not covered by PCMO (fig.5.1a). A calibrated cernox thermometer was used for temperature measurements in the presence of magnetic field.

5.3 Results and Discussion:

Figure 5.2 shows the X-ray diffraction pattern recorded for the YBCO/PCMO bilayer film. The peaks corresponding to PCMO, YBCO and STO have been indicated as P, Y and S respectively. Analysis of the X-ray diffraction data confirms the formation of the bilayer films with a *c*-axis oriented growth of YBCO film on STO substrate. It is also seen from the figure 5.2 that the PCMO peaks are very close to the peaks corresponding to STO. It may also be noted that the b-axis of the PCMO film is perpendicular to the a-b plane of the STO substrate. The inset of figure 5.2 shows the expanded view of the *[300]* peak region of the STO substrate indicating Cu $K_{\alpha 1}$ and $CuK_{\alpha 2}$ splitting of *[300]* peak where *(009)* peak of YBCO and *(060)* peak of PCMO is also seen.

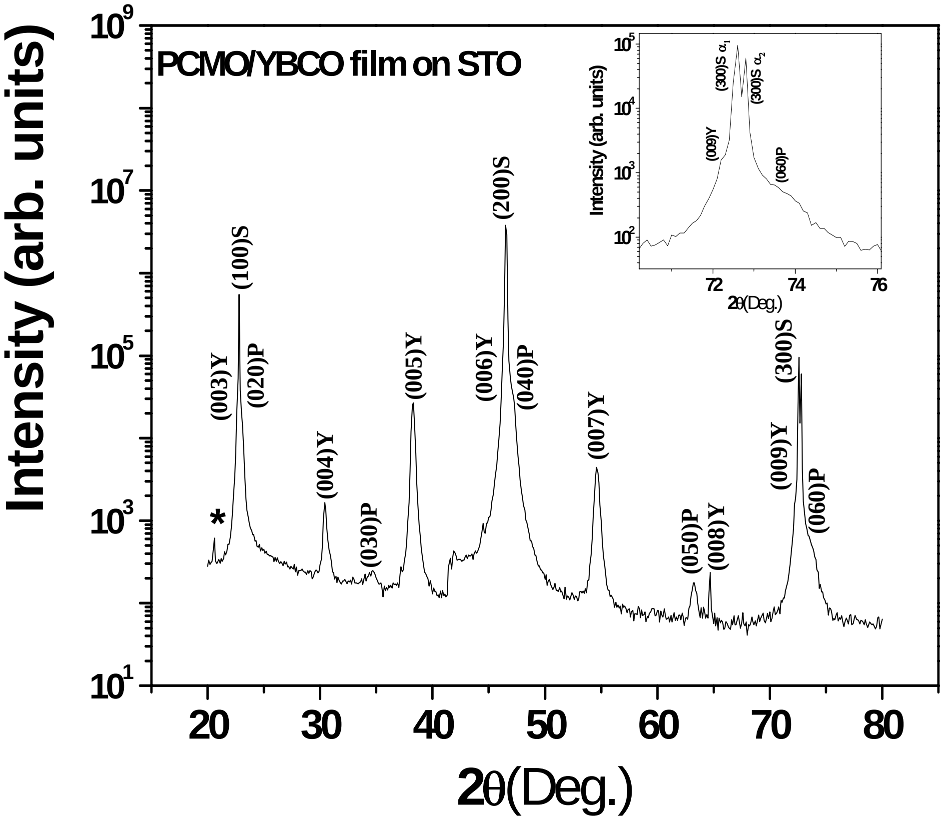

Fig. 5.2. *XRD pattern of the PCMO/YBCO bilayer deposited on STO substrate. The peaks corresponding to YBCO, PCMO and STO are labelled as Y, P and S respectively. An expanded view of the part of the XRD pattern indicating (300) peak of STO as well (009) peak of YBCO and (060) peak of PCMO is shown in the inset.*

The behaviour of electrical resistivity of the PCMO/YBCO bilayer under the application of different measuring currents ranging from 1mA to 40 mA has been shown in figure

5.3. R(T) behaviour on the bilayer side is shown in figure 5.3(a), 5.3(b) and 5.3(c) for applied magnetic fields of H= 0 T, 6 T and 12 T respectively, while figure 5.3(d), 5.3(e) and 5.3(f) show the R(T) plot measured on the uncovered YBCO side for H=0 T, 6 T and H=12 T respectively. It may be noted that no change in R(T) behaviour was observed for measuring current (I) in the range 10 μA – 1 mA in measurements carried out on both the sides. However, for I > 1mA, the superconducting transition temperature (T_c) was found to decrease gradually with increasing current (see figure 5.3(a), (b) and (c)). In addition, a hump like feature is observed in the electrical resistivity near the onset of T_c. The width of the superconducting transition ΔT_c, deduced from the R(T) at a given current, was found to increase with increase in applied magnetic field (see figure 5.3). Fig. 5.3(d), 5.3(e) and 5.3(f) clearly show the absence of the hump like feature in the electrical resistivity near the onset of T_c on the YBCO side in stark contrast to the experimental observations on the YBCO/PCMO bilayer side as shown in fig 5.3(a), 5.3(b),and 5.3(c). It may also be noted that the rate of suppression of T_c with increase in measuring current is considerably lower on the YBCO side as compared to that observed on the bilayer side which will be explained later.

The important experimental observations may be summarized as follows:

(1) Upto 1mA applied current, there is no shift in the superconducting transition temperature T_c observed by the resistivity technique.

(2) A hump like feature is observed for all values of the applied current and magnetic field on the bilayer side, whereas no hump is seen on the YBCO side (see fig.5.3).

(3) Suppression of T_c is seen in the R(T) curve for applied currents greater than 1mA on both the YBCO side as well as the bilayer side. However, the suppression of T_c

is higher on bilayer side compared to that observed on the YBCO side (see fig. 5.5).

(4) Maximum resistance measured in the hump region decreases with increase in applied magnetic field and current (see fig. 5.6).

(5) Measured value of the critical current (I_c) is relatively higher on the YBCO side compared to that on the bilayer side (see fig.5.7).

(6) Width of the superconducting transition increases with increase in applied current and magnetic field on both the YBCO side and the bilayer side (see fig. 5.3).

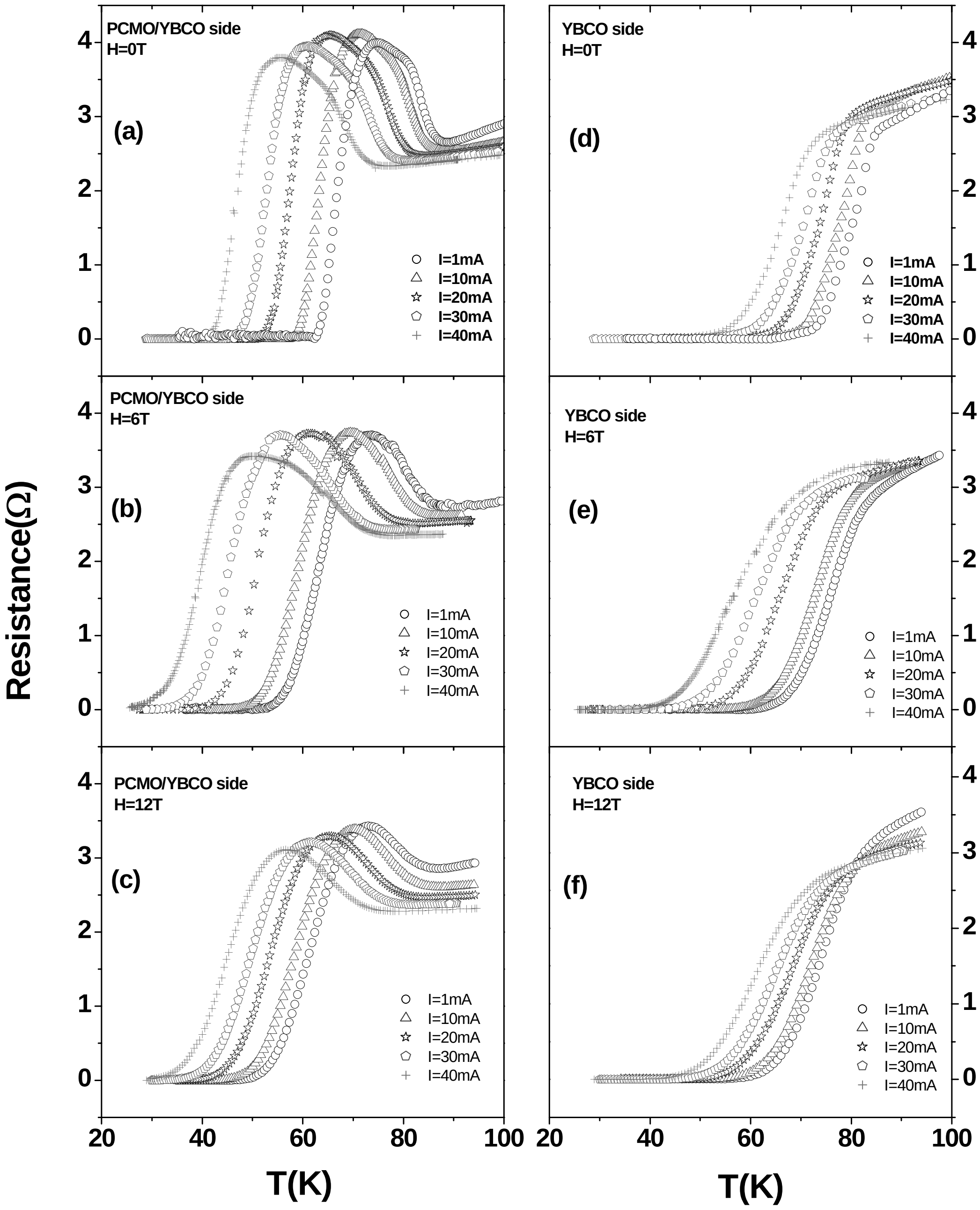

***Fig. 5.3**. (a), (b) & (c) Temperature dependent resistance at H=0T, 6T and 12T respectively for different applied current ranging from 1mA to 40mA for the PCMO/YBCO bilayer side whereas (d), (e) & (f) show the corresponding data for the YBCO side.*

The above observations can be rationalized by invoking a current dependent proximity effect associated with the PCMO film deposited on the superconducting YBCO layer. PCMO undergoes a phase transition from charge ordered (CO) antiferromagnetic insulating state to charge delocalized ferromagnetic metallic (FM) state. The volume fraction of the nucleated FM metallic phase increases with an increase in the externally applied current or magnetic field [12]. The FM domains seems to grow preferentially along the applied electric field (current); it is assumed that the FM and CO phases remain randomly oriented and isolated from each other upto the maximum current applied (~40 mA) as shown schematically in fig. 5.1(b). In this figure, the FM clusters are shown as darkly shaded regions over the uniform CO background. These FM clusters can grow in size with an increase in applied magnetic field or current. The effects such as proximity effect and quasi-particle spin injection from these FM clusters can influence the superconducting properties of the adjacent YBCO layer.

A schematic sketch of the YBCO film, half of which is covered by the PCMO film on the bilayer side, is shown in figure 5.1(a). The left side of the diagram indicates the PCMO/YBCO bilayer portion while the right side of the diagram indicates the YBCO portion not covered by PCMO. During the measurements, applied current was passed through the contacts A and D on the bilayer side, while the voltage was measured across the contacts P & Q for the resistance measurements on the bilayer side and across the contacts R & S for the resistance measurements on the YBCO side respectively. The top PCMO film can be modeled as a series of interconnected network of N charged ordered regions having a relatively high resistance and N low resistance FM clusters as shown schematically in figure 5.4. The values of these resistances between the contacts A and D are denoted as $R_{CO}(i)$ and $R_{FM}(i)$ (i=1 to N) respectively as shown in figure 5.4. In this figure, B-E-F-C denotes the low resistive path through the YBCO film which is also modeled to be comprised of N resistances $R_{YB}(i)$, connected in series. In this schematic, there are N parallel resistive paths between the lines AD and BC traversing through the thickness of PCMO (i.e. perpendicular to the surface of the film) whose values are denoted as $R_{CO}(d_i)$. As the value of R_{CO} is much greater than that of R_{FM} and R_{YB}, we can neglect the current flowing through the intermediate high resistive paths namely $R_{CO}(d_2)$ to $R_{CO}(d_N)$ etc for simplicity. The effective resistance between the contacts A and D is then given by

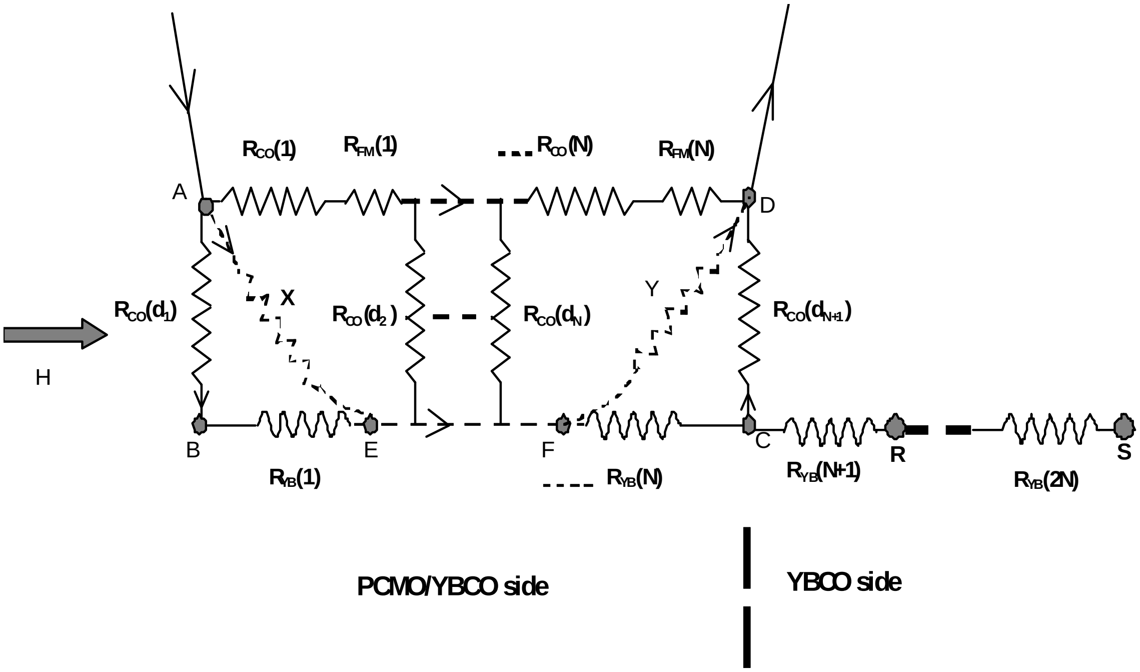

Fig. 5.4. *The schematic equivalent resistance circuit representing the bilayer side and YBCO side of the sample represented in fig.5. 1(a).*

$$R_{result} = \frac{(NR_{CO} + NR_{FM})(2R_{CO} + NR_{YB})}{(N+2)R_{CO} + NR_{FM} + NR_{YB}} \text{ ------------------------------} \mathbf{(1)}$$

As N>>1 and near T_c, $(R_{CO} + R_{FM}) > R_{YB}$, the above equation may be simplified as

$$R_{result} = 2R_{CO} + NR_{YB} \text{ --(2)}$$

Thus, R_{result} turns out to be the resultant resistance along the path A-B-E-F-C-D as shown in figure 5.4. Our experimental observations can be explained using this simplified resistance network model as follows;

(1) It has already been observed that a critical value of external control variable is required for the charge ordered manganite PCMO to undergo a phase transition from a charge ordered phase with positionally ordered arrangement of Mn^{3+} and Mn^{4+} ions to a charge delocalized phase, which is ferromagnetic [13-15]. In the present experiment, the formation of FM phase in the PCMO layer of the thin film bilayer structure requires the applied current to exceed a critical value of 1mA. Due to the absence of FM clusters in the PCMO film below a current of 1mA, no significant proximity effect related shift in T_c is experimentally observed below an applied current of 1mA.

(2) An electric field (current) induced charge order melting occurs in the PCMO thin film when the applied current is higher than 1mA, leading to the nucleation of tiny clusters of ferromagnetic (FM) phase dispersed in a matrix of charge ordered PCMO. These FM clusters can grow larger in size with further increase in measuring current and (or) applied magnetic field as illustrated schematically in figure 5.1(b). The proximity of FM clusters and the underlying YBCO superconducting film leads to the suppression of the T_c of the bilayer due to effects such as exchange field, injection of quasiparticles from FM clusters etc. The gradual suppression of the T_c at higher values of measuring current

indicates that the FM clusters grow larger in size with an increase in current. The local heating effect at higher values of measuring current was ruled out as a possible reason for the observed decrease in T_c since sufficient cooling time was given during the measurements; in fact, only a very small temperature change (less than 0.5K at 40mA current) was recorded by the cernox sensor mounted on the sample holder during the measurements. The current dependent R(T) measurement on the virgin YBCO single layer (not shown in figure), under similar experimental conditions, showed much smaller shifts in T_c compared to those observed for the bilayer film, which further rules out the possible apparent decrease of T_c because of the self-heating effect in the sample at high values of applied current. It may be noted that the proximity effect (associated with the ferromagnetic clusters in PCMO) and quasi-particle spin injection effect are two distinct effects which are responsible for the suppression of the superconducting transition temperature T_c as observed in the present study. The variation of T_c measured on the PCMO/YBCO bilayer side and on the YBCO side of the sample with applied current and magnetic field has been shown in fig. 5.5. For comparison, variation of T_c of a virgin single layer YBCO film deposited on STO substrate with applied current is also shown in fig.5.5. It is evident from fig.5.5 that when the applied current is increased beyond 1 mA, T_c suppression on the YBCO side is relatively less compared to that observed on the bilayer side.

The higher rate of suppression of T_c observed on the PCMO/YBCO bilayer side compared to that on the YBCO side indicates a greater overall weakening of superconductivity on the bilayer side because of the ferromagnetic clusters in the PCMO layer. The underlying YBCO thin film on the bilayer side is directly under electrical rise contact with PCMO layer on top. This direct contact of PCMO film onto YBCO gives to two distinct effects, namely, exchange-field induced proximity effect and quasi particle spin injection emanating from the FM clusters embedded into the charge ordered PCMO. On the other hand, thin film on the YBCO side does not have any direct contact with the top PCMO layer and, hence, only the spin injection effect can influence the superconducting properties on the YBCO side [16]. These experimental results clearly demonstrate the distinction between the proximity and the spin injection effects, which can be judiciously used to control the T_c of a superconducting YBCO film. It may be noted here that the T_C suppression in virgin YBCO sample is negligible compared to the bilayer structure due to the absence of any proximity and spin injection effect arising from PCMO film.

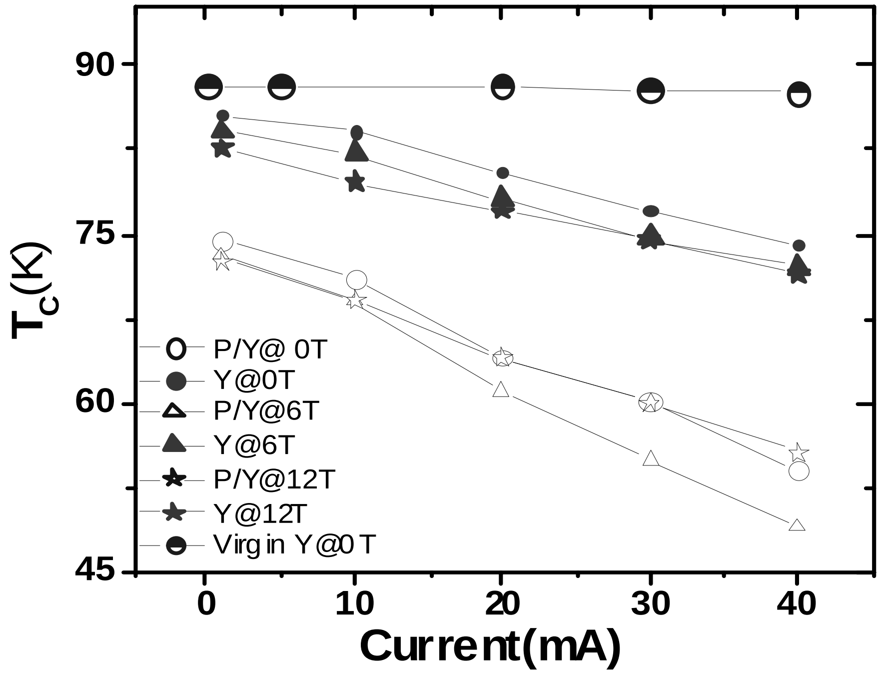

Fig. 5.5. *Variation of T_C with applied current for a virgin YBCO film (denoted as 'virgin Y'), single layer film on the YBCO side (denoted as 'Y') and on the PCMO/YBCO bilayer side (denoted as 'Y/P') for H=0T, 6T and H=12T field.*

(3) A hump like feature has been observed near the onset of the superconducting transition in the temperature dependence of resistance of the bilayer side for a range of values of applied current and magnetic field (fig.5.3) but is absent on the YBCO side not covered by PCMO. It may be noted that the net variation of effective resistance of the sample with temperature is mainly governed by a competition between R_{CO} and R_{YB}. As the temperature decreases, the value of R_{CO} varies exponentially with temperature with a large negative temperature coefficient of resistance and, hence, the magnitude of $dR_{CO}/dT >> dR_{YB}/dT$ in the temperature range just before the onset of superconductivity. Under these circumstances, the temperature dependence of $R_{resultant}$ is mainly dominated by the temperature dependent changes in R_{CO} and the negative temperature coefficient of resistance of R_{CO} causes a sudden rise in resistance near T_c resulting in the appearance of a hump-like feature. The absence of this hump-like feature on the YBCO side at different values of applied current and magnetic field lends support to this hypothesis.

(4) The maximum resistance attained in the hump region is designated as "R_{peak}"; R_{peak} decreases with increase in magnetic field and current. The variation of R_{peak} with applied current at different values of external magnetic field is shown in fig.5.6.

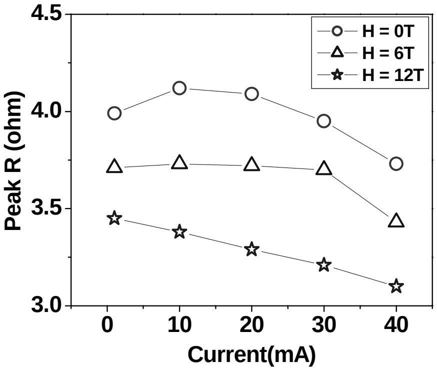

Fig. 5.6. *Variation of the resistance at the peak position of the hump with the applied current ranging from 1mA to 40mA at different values of external magnetic field.*

The possible reason for the above observation is that the FM metallic clusters generated in the PCMO film grow further in size with increase in magnetic field and applied current which leads to the reduction in the effective resistance between the contact points A and D. Therefore the overall resistance $R_{resultant}$ of the bilayer side decreases with increase in applied magnetic field as well as current. It may be noted that the measured value of R(T) at different values of applied current and magnetic field critically depends on the thickness of the top PCMO layer in any individual PCMO/YBCO multilayer heterostructure.

(5) The critical currents (I_c) for both the YBCO side and the bilayer side of the sample have been measured at three prefixed temperatures (33K, 38K and 45K) for applied magnetic field ranging between 0T and 12T. During this measurement, the contact points have been maintained at positions similar to those indicated in fig. 5.1(a). The variation of I_c with applied magnetic field for both the YBCO side and the bilayer side is shown in fig. 5.7(a) and 5.7(b) respectively. Our experimental observations indicate that at any fixed temperature, the I_c values on the YBCO side are relatively lower compared to those measured on the bilayer side. While I_c decreases initially with increase in applied magnetic field, the dependence flattens at higher applied magnetic field (i.e. 6 T and 12 T). The influence of direct proximity and spin injection effects is much stronger on the bilayer side than on the YBCO side since the latter experiences only the spin injection effect. Therefore, T_c gets suppressed on the bilayer side to a greater extent compared to the suppression of T_c observed on the YBCO side.

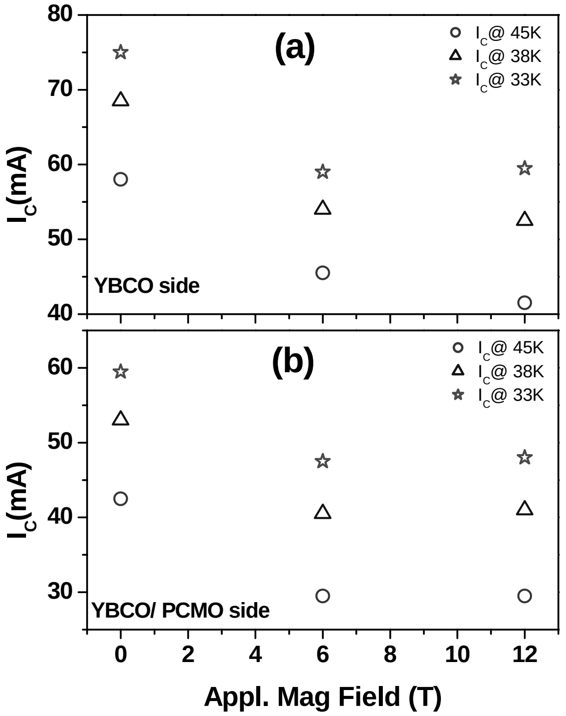

Fig. 5.7. *Variation of critical current (I_c) with applied magnetic field for the part of the sample on the (a) YBCO side and (b) PCMO/YBCO bilayer side at three fixed temperatures, viz., 45K, 38K and 33K.*

(7) The width of the superconducting transition, as observed using the measurement of resistance of the film as a function of temperature, is found to increase under the application of external magnetic field. The measured resistance at temperatures just higher than those at which zero resistance state is attained is a consequence of thermally activated flux flow [17,18]. The energy associated with this activated behavior depends on the pinning of vortices in the YBCO layer. The activation energy may be estimated by fitting the tails of the superconducting transitions to the usual activated behavior, for instance, by plotting lnρ vs 1/T. Assuming $U(H,T) = U_0(H)(1-T/T_C)$ for the temperature dependence of the activation energy, it is possible to express the resistance $R(H,T)= R_0 \exp[-U_0(H, T) /k_BT]$. Then one can estimate the extrapolated zero temperature activation

energy U(T=0,H) = U_0(H) from the slope of plots of lnR vs 1/T. The value of U_0 has been estimated using this method at different values of applied magnetic field and current. The variation of U_0 as a function of magnetic field and current is shown in fig. 5.8(a) and fig. 5.8(b) respectively for the part of the film on the bilayer side as well as the YBCO side.

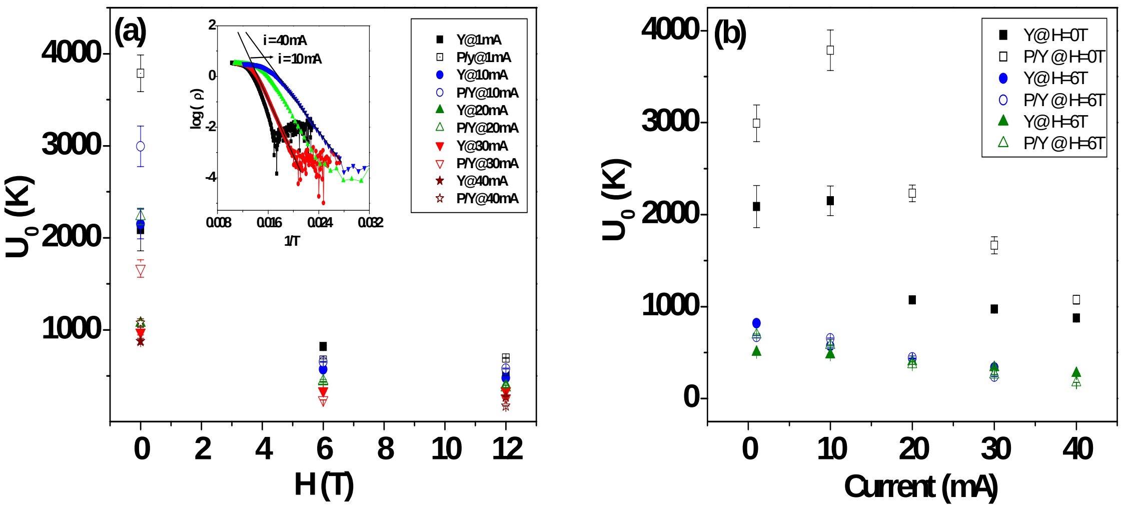

Fig. 5.8. *(a) Variation of activation energy (U_0) with applied magnetic field (H) for both the YBCO (indicated as Y) side and the PCMO/YBCO (indicated as P/Y) bilayer side. (b) Variation of activation energy (U_0) with applied current for both the YBCO side and the PCMO/YBCO side. Inset of fig. 5.8(a) shows some representative plots for estimating U_0 by linear fitting of log(R) vs 1/T.*

It is seen from fig. 5.8(a) that after an initial rapid decrease in the value of U_0 with an increase in the magnetic field (upto H=6 T), the dependence flattens at higher fields; such a behavior has been seen in many superconducting materials and may possibly indicate a transition from single vortex pinning at low magnetic fields to a collective pinning at high magnetic fields. In epitaxial YBCO film, the U_0 is known to be proportional to ($1/H^{\alpha}$) where $\alpha = 1$. It may also be noted that the value of U_0 inferred for the bilayer side is higher compared to that observed for the YBCO side. In the bilayer side, the YBCO thin film is in direct contact with the PCMO layer so that the FM clusters nucleated in the PCMO layer contribute to the enhancement of pinning strength leading to the observation of higher activation energy U_0 on the bilayer side compared to that for the YBCO side. Fig.5.8 also shows that U_0 decreases with an increase in the applied current and the U_0 for the bilayer portion is estimated to be relatively higher compared to that for the YBCO side. While the number of ferromagnetic clusters may be expected to increase with increase in applied current, there is an inevitable weakening of superconducting properties due to spin injection effect and proximity effect leading to a relatively lower value of U_0 at higher applied current.

5.4 Conclusion:

A bilayer thin film of PCMO/YBCO has been deposited in which about half of the bottom YBCO film is covered by the top PCMO layer. The magnetoresistance measurements on this film and related analysis reveal that the suppression of T_c is higher on the bilayer side of the sample compared to that on the YBCO side. This is due to the proximity effect and the quasi-particle spin injection effect from the top PCMO layer into the adjacent YBCO layer. But on the YBCO side, the proximity effect associated with the FM clusters in the PCMO layer may be excluded; superconducting properties on the YBCO side may, however, be affected by injection of spin polarized charge carriers. The results show a possibility of using these effects in spin injection devices where the superconductivity in a part of the YBCO thin film may be controlled by using spin injection effect arising from the ferromagnetic clusters in an adjoining YBCO/PCMO bilayer using a control variable such as applied current or magnetic field.

Reference:

[1] A. I. Buzdin *Rev. Mod. Phys. 77, 935 (2005)*

[2] F. S. Bergeret, A. F. Volko, and K. B. Efetov *Rev. Mod. Phys. 77, 1321 (2005)*

[3] Daniel Hsu, L. G. Lin, C. P. Chang, C. H. Chen, C. H. Chiang, W. C. Chan and W. F. Wu *JAP 103, 07C710 (2008)*

[4] J. G. Lin, Daniel Hsu, W. F. Wu, C. H. Chiang and W. C. Chang *JAP 101, 09G106 (2007)*

[5] Hanns-Ulrich Habermeier, Soltan Soltan and Joachim Albrecht *Physica C 460-462, 32 (2007)*

[6] J. G. Lin, S. L. Cheng, C. R. Chang and D. Y. Xing *JAP 98, 023910 (2005)*

[7] Daniel Hsu, L. G. Lin, C. P. Chang, C. H. Chen, W. F. Wu,C. H. Chiang and W. C. Chan *APL 90, 162504 (2007)*

[8] W. Westhauser, S. Schramm, J. Hoffmann and C. Jooss *Eur. Phys. J. B 53, 323 (2006)*

[9] G. Deutscher *Rev. Mod. Phys. 77, 109 (2005)*

[10] S. Soltan, J. Albrecht and H. U. Habermeier *Phys. Rev. B 69, 224502 (2004)*

[11] Dipak Kumar Baisnab, T. Geetha Kumary, A. T. Satya, Awadhesh Mani, R. Nithya, L. S. Vaidhyanathan, M. P. Janawadkar and A. Bharathi *J. Appl. Phys. 111, 113910 (2012)*

[12] W. Westhauser, S. Schramm, J. Hoffmann and C. Jooss *Eur. Phys. J. B 53, 323 (2006)*

[13] V. Kiryukhin, D. Casa, J. P. Hill, B. Kelmer, A. Viglinate, Y. Tomioka and Y. Tokura *Nature 386, 813 (1997).*

[14] Y. Tomioka, a. Asamitsu, H. Kuwahara, Y. Morotima and Y. Tokura *Phys. Rev. B 53, 1689 (1996)*

[15] M. Hervieu, A. Barnabe, C. Martin, A. Maignan and B. Raveau *Phys. Rev. B 60, 726 (1999)*

[16] Hyunsoo Yang, See-Hun Yang, Saburo Takahashi, Sadamichi Maekawa and Stuart S. P. Parkin *Nature Materials 9, 586 (2010)*

[17] T. T. M. Palstra, B. Batlogg, R. B. Van Dover, L. F. Schneemeyer and J. V. Waszczak, *Phys. Rev. B 41, 6621 (1990)*

[18] H. C. Yang , L. M. Wang and H. E. Horng *Phys. Rev. B 59, 8956 (1999).*

Chapter 6

Combined Effect of Current and Strain Induced CO Melting in PCMO/YBCO/PCMO Trilayer

6.1 Introduction:

In the last few years, there has been considerable interest in the study of charge ordered manganites such as $Pr_{0.5}Ca_{0.5}MnO_3$ (PCMO) due to several unique characteristics of the phase transition from a charge ordered antiferromagnetic insulating state to a charge delocalized ferromagnetic (FM) metallic state [1-5]. There is a substantial experimental evidence to show that the charge ordered (CO) state is unstable under a variety of external perturbations [7-13]. Indeed, the influence of external parameters such as magnetic field, substrate induced strain and electric field on this phase transition are quite remarkable. The influence of the magnetic field on the phase transition is due to the Zeeman energy gain of FM state on account of the external magnetic field [14,15] whereas a strong electric field is known to influence the phase transition due to movement of hole-like charge carriers derived from the plane containing Mn^{3+} and Mn^{4+} ions in charge ordered manganites [11,16 &17]. On the other hand the phase transition in CO manganite is known to be driven by coupled electronic and lattice degrees of freedom and, therefore, the substrate induced strain on the lattice can also influence the phase transition [18-23]. When deposited in the thin film form, manganites allow the possibility of investigating the effect of these external perturbations on the phase transition. In recent years, there is an increasing effort to use these CO melting phenomena to control the spin injection into the high temperature superconductor (HTS) and thereby control the superconducting properties of HTS [24-29]. While it would be interesting to investigate the behavior of HTS/manganite heterostructures when simultaneously subjected to several of these external perturbations, there is no report in the literature on the effect of simultaneous use of several such external perturbations to effectively control the spin injection into the HTS. An experimental study was therefore undertaken to investigate this and the results obtained have been described in this chapter.

In the preceding chapters, the formation of ferromagnetic (FM) clusters in the charge ordered $Pr_{0.5}Ca_{0.5}MnO_3$ layer by the application of substrate induced strain and electric field has been described in detail. Experimental evidence was presented to show that the substrate induced strain can effectively nucleate the FM clusters in PCMO thin film below a certain thickness. As the specimen is cooled, the nucleation and growth of FM clusters are formed as a result of melting of the charge-order which can result in an overall metallic behavior in charge transport by the mechanism of percolation. In a similar way, the electric field (current) can also induce the formation of FM clusters in the PCMO layer of YBCO/PCMO bilayer thereby progressively increasing the injection of spin polarized electrons into the adjacent YBCO layer, consequently, suppressing the superconducting transition temperature T_c of the YBCO layer. The estimation of the activation energy for hopping of vortices using the thermally assisted flux-flow model indicates that the formation of FM clusters due to the application of current enhances the pinning of vortices (shown in chapter 5). The experiments described in this chapter investigate the effect of simultaneous use of both the substrate induced strain and applied electric field (current) to generate FM clusters in the PCMO layer and examine the cumulative effects of these two external parameters on the superconducting properties of the sandwiched YBCO layer. Towards this, two different PCMO/YBCO/PCMO trilayers were deposited on MgO substrate; the thicknesses of the layers were appropriately selected to enable the investigations of the phenomena of interest. In one trilayer heterostructure, the PCMO layer experienced both substrate induced strain as well as electric field (current) whereas in the other trilayer, PCMO layer was subjected to electric field only. Both the trilayers were characterized by measuring the electrical resistivity of the trilayer as a function of temperature in the presence of external magnetic fields. A comparison of the behavior of the two trilayers clearly shows that the trilayer under the simultaneous influence of both strain and electric field exhibits a stronger spin injection behavior compared to the trilayer which was subjected to the effect of electric field only.

6.2 Experimental Details:

$Pr_{0.5}Ca_{0.5}MnO_3$ /$YBa_2Cu_3O_7$ / $Pr_{0.5}Ca_{0.5}MnO_3$ trilayer thin films of different thicknesses were deposited on (100) oriented MgO substrates using the pulsed laser deposition technique. The bulk polycrystalline target materials of $Pr_{0.5}Ca_{0.5}MnO_3$ (PCMO) and $YBa_2Cu_3O_7$ (YBCO) used for the preparation of thin films were synthesized by the standard solid state reaction method [see chapter 4]. As a first (bottom) layer, PCMO thin film was deposited on the MgO substrate and YBCO thin film was then deposited on top of this PCMO layer. Finally, another layer (top layer) of PCMO was deposited on the YBCO layer. The trilayer deposition using the PLD technique was similar to the bilayer deposition described in chapter 4.

In one trilayer thin film heterostructure, the thickness of the bottom PCMO layer was selected to be ~40 nm whereas the second layer YBCO and the top PCMO layers had a thickness of ~ 100 nm and ~110 nm respectively. This trilayer is designated as a strained film because the bottom PCMO layer was very thin (~40 nm) and experienced a substrate induced strain due to the lattice mismatch between MgO and PCMO. As mentioned in chapter 3, the lattice mismatch between PCMO and MgO is ~9.4%. In the other trilayer film, designated as a relaxed film, the thickness of the bottom PCMO layer was selected to be ~100nm, whereas both the second YBCO layer and the top PCMO layers had a thickness of ~100nm. In this relaxed film, selection of a sufficiently higher thickness for the bottom PCMO layer helps to relax the strain induced by the substrate. The schematic diagrams of these two thin film heterostructures have been given in figure 6.1.

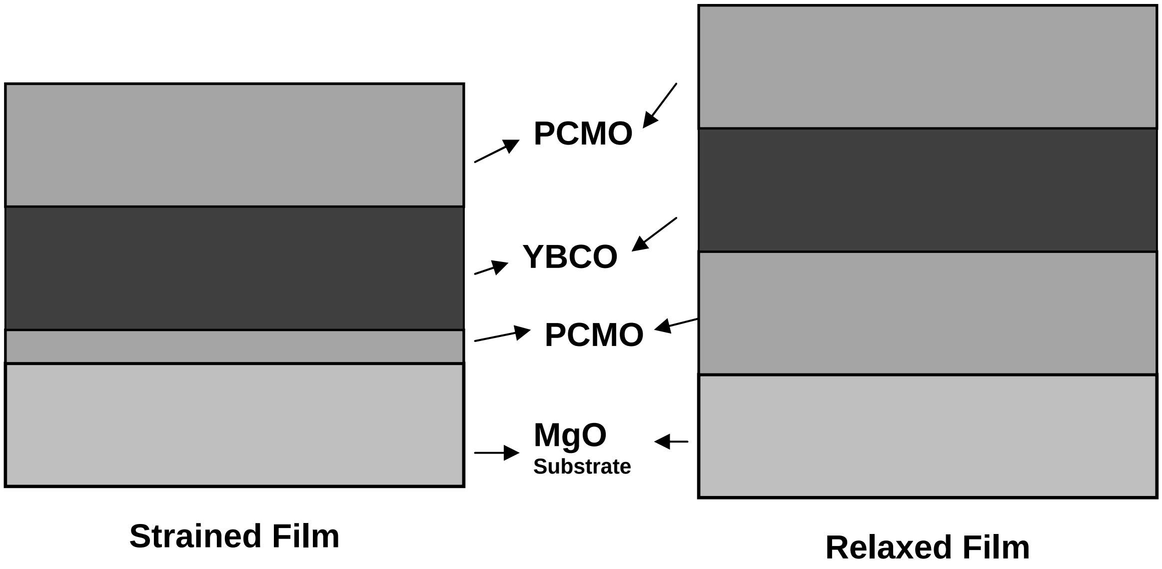

Fig. 6.1. *The schematic illustration of PCMO/YBCO/PCMO trilayers deposited on the MgO substrate.*

The total thickness of both the trilayer films was measured by DEKTAK 3030A surface profiler, whereas the individual layer thicknesses were estimated based on the number of laser shots and prior calibration runs on the deposition of the corresponding individual single layers while maintaining the identical deposition parameters. The crystal structure and the orientation of the film were characterized by X-ray diffraction (XRD) measurements in an STOE diffractometer using CuK$_\alpha$ radiation. Electrical resistivity measurements were carried out in the temperature range 4.2 K to 300 K using four probe technique at two different measuring currents, 1mA and 5 mA. Magnetoresistance (MR) measurements were also carried out under magnetic fields upto

8 T with two different values of applied current (1mA and 5 mA). A calibrated cernox resistance thermometer was used for temperature measurements in the presence of magnetic field.

6.3 Results and Discussion:

XRD pattern of the trilayer film is shown in Fig. 6.2. The peaks corresponding to YBCO, PCMO and MgO have been labeled as Y, P and M respectively.

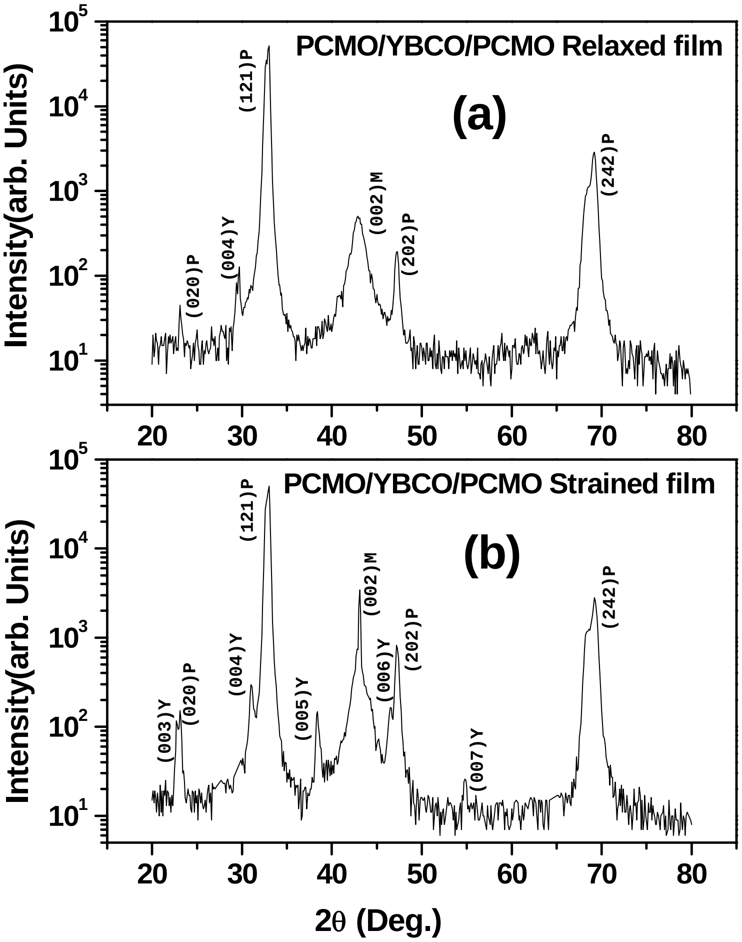

Fig. 6.2. *XRD pattern of the PCMO/YBCO/PCMO trilayer on MgO substrate for (a) relaxed film and for (b) strained film. The peaks corresponding to YBCO, PCMO and MgO have been labeled as Y, P and M respectively.*

It is evident from the figure that PCMO films have a (*121*) orientation (*i.e.*, [*121*] axis perpendicular to the plane of the substrate). As mentioned in chapter 3, the d spacing corresponding to the (002) reflection (d = 2.700 Å) almost matches with that of (*121*) reflection (d = 2.698Å). However, considering the large lattice mismatch between the *ab* plane of PCMO and that of the MgO substrate, it is very unlikely for the films to grow with (*002*) orientation. Small intensity lines indexed as (*020*) and (*202*) are also observed in both the films as shown in Fig.6.2. The broad peak of the MgO substrate observed near $2\theta = 43°$ represents the (*002*) reflection. [13] . It may be noted that several diffraction peaks for the YBCO film are seen in the strained film whereas only the highest intensity peak (004) is seen for the relaxed film. The possible reason for the absence of the lower intensity YBCO peaks in the relaxed film is due to the higher lattice mismatch between the relaxed PCMO and YBCO. In the strained film, the PCMO layer is very thin and exhibits lattice parameters somewhat closer to those of MgO substrate and is, therefore, likely to provide a more ideal platform for the subsequent growth of the YBCO film compared to that provided by the relaxed PCMO layer.

Figure 6.3 represents the temperature dependent resistance behaviour for both the trilayers at two different values of applied current (1mA and 5 mA) without externally applied magnetic field. As shown in figure 6.3(a) and 6.3(b), both the trilayers exhibit a negative temperature coefficient of resistance from room temperature to a certain value of low temperature (~ 80 to 90 K). As the specimen is cooled further, the temperature dependence of electrical resistivity shows a double-hump like behaviour at low temperature and a shoulder like plateau at ~50 K. At still lower temperatures, resistance is seen to vanish as the trilayer transforms to the superconducting state.

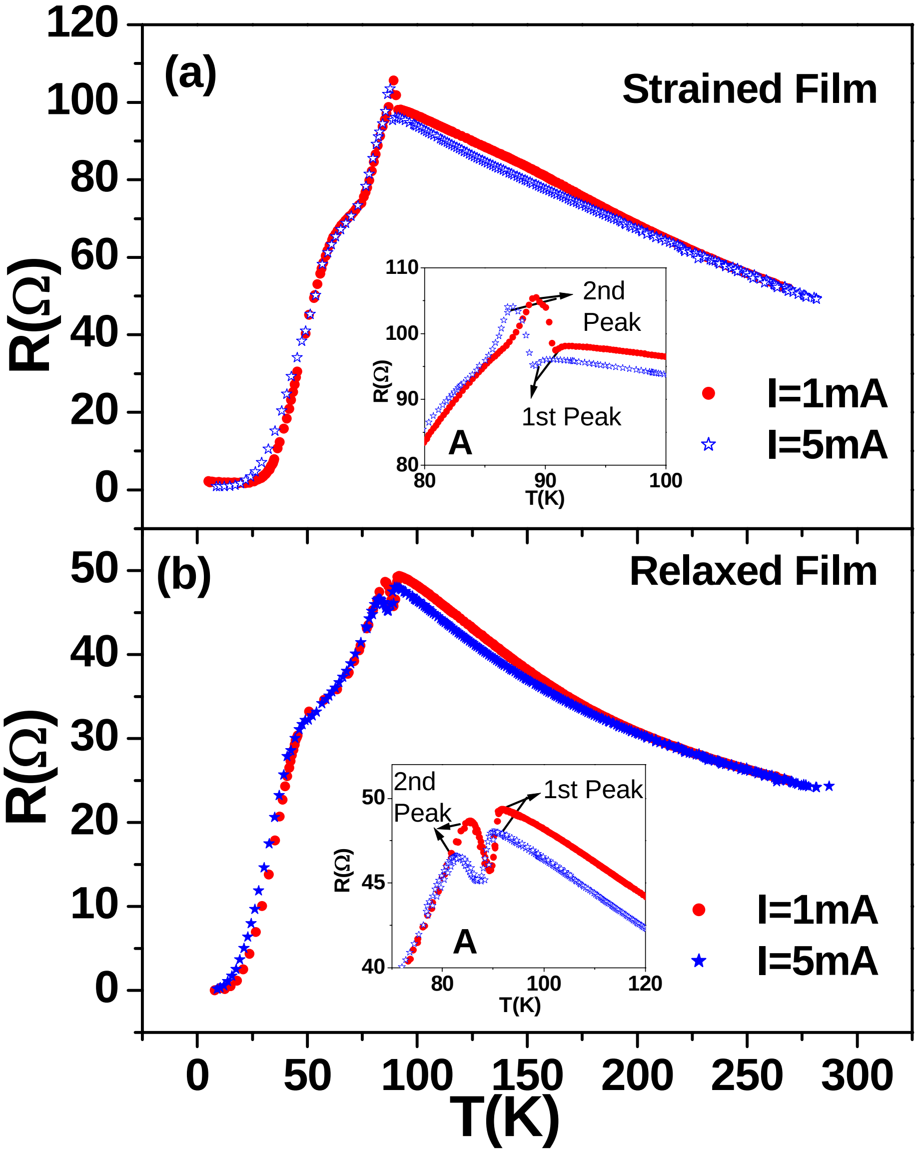

Fig. 6.3. *Temperature dependent resistance at 1mA and 5mA applied current without qpplying external magnetic field for (a) strained film and for (b) relaxed film.*

Figure 6.4 shows the observed temperature dependence of resistance of the two trilayers at an applied current of 1mA and 5 mA when a magnetic field ranging from 0 T-8 T is applied.

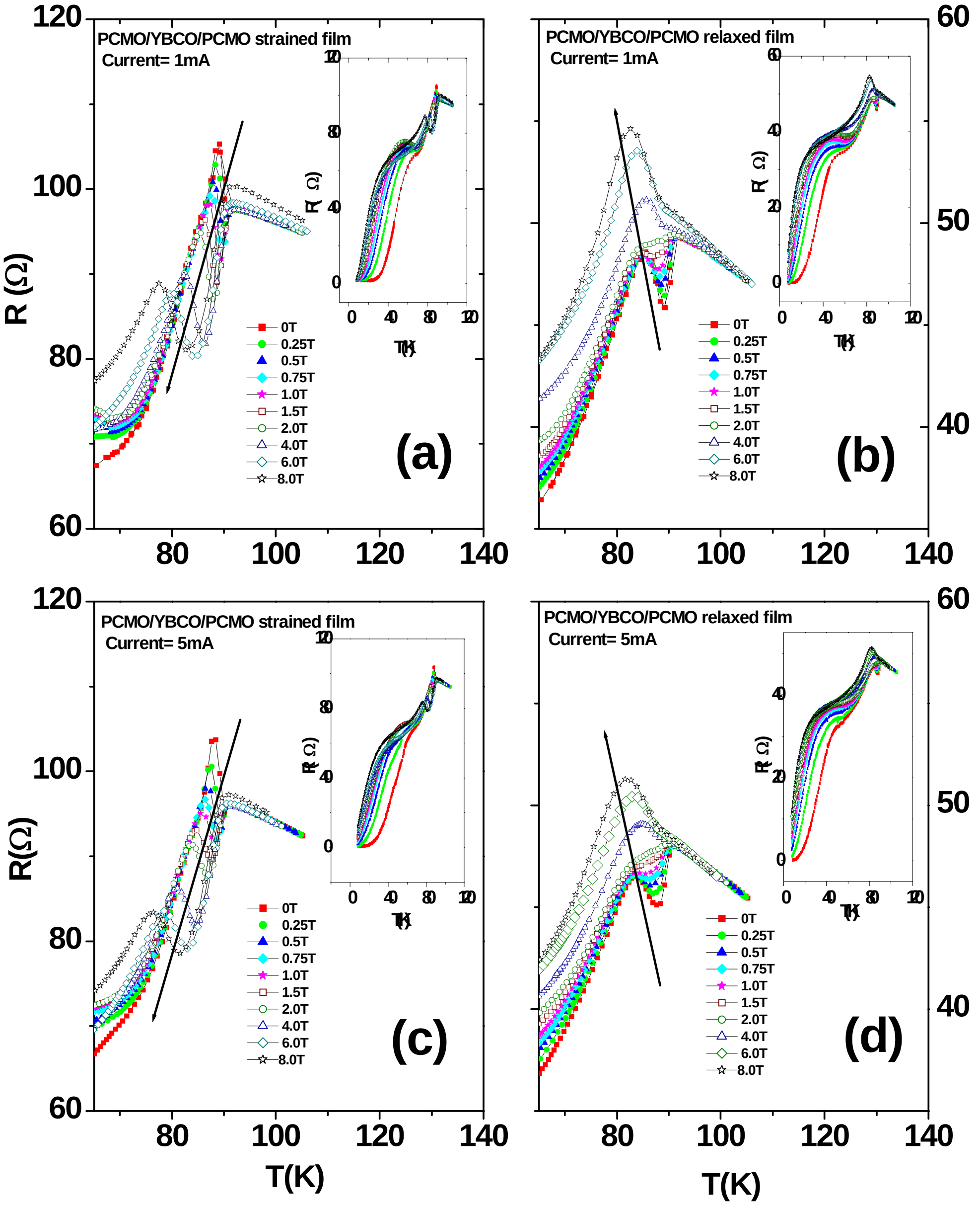

Fig. 6.4. Temperature dependent resistance behaviour near the hump region for different applied magnetic field ranging from 0 T to 8 T for (a) strained film at 1mA applied current (b) relaxed film at 1mA applied current (c) strained film at 5mA applied current and (d) relaxed film at 5 mA applied current. Insets of fig.6. 4(a), (b), (c) and (d) show the corresponding temperature dependent resistance for a wider range of temperature (from 4.2 K to 100 K).

Figures 6.4(a) and (c) show an expanded view of magnetic field dependent R(T) behaviour near the hump like region for the strained film at 1mA and 5 mA current respectively whereas the insets show the R(T) behavior of the strained film over a wider temperature range (from 4.2K to 100K). Figures 6.4(b) and (d) show the expanded view of the magnetic field dependent R(T) behaviour near the hump region for the relaxed film at 1mA and 5 mA applied current respectively whereas the insets show the R(T) behavior of the relaxed film over a wider temperature range (4.2K to 300K). The relaxed film exhibits a positive magnetoresistance near the hump region as well as for the entire temperature range. It may also be noted that for the relaxed film the double-hump feature observed at zero magnetic field changes in appearance to a single hump-like feature as the magnetic field is increased. In the case of the strained film, a negative magnetoresistance is observed near the hump region but a positive magnetoresistance is seen for the rest of the temperature range. Further, for the strained film, the double hump like feature retains its characteristic shape when a magnetic field is applied. The experimentally observed characteristic features in the temperature dependence of resistance of the two trilayers in the presence of a magnetic field may be summarized as follows:

(1) both the films show a semiconductor-like negative temperature coefficient of resistance over the temperature range of ~ 90 K to 300 K;

(2) in general the resistance value of the strained film is higher than that of the relaxed film;

(3) a double hump like feature is seen just below the temperature of ~90 K;

(4) a positive magnetoresistance is seen for the relaxed film near the hump region whereas a negative magnetoresistance is seen for the strained film near the hump region;

(5) overall positive magnetoresistance is seen for both the films at lower temperatures;

(6) suppression of T_c (taken at mid point) for the strained film is higher at higher current compared to that observed for the relaxed film,

(7) at lower temperatures (~50K), a shoulder-like plateau is seen for both the films.

The above observations may be explained on the basis of the formation of the ferromagnetic clusters under the application of substrate induced strain, applied magnetic field and the applied electric field (current). However, it is necessary at this stage to recapitulate a few basic facts described in the preceding chapters as well as literature:

(a) charge ordered PCMO thin film exhibits a insulator-to-metal transition for a certain thickness (35 nm to 45 nm) due to the substrate induced strain;

(b) fully relaxed (thick film) PCMO film or the bulk PCMO requires the application of a relatively large magnetic field ~25 T to induce the melting of charge order and the formation of ferromagnetic metallic phase;

(c) relaxed PCMO film without substrate induced strain can show a higher resistance when a magnetic field is applied due to the increased path lengths of trajectories of charge carriers on account of the Lorentz force experienced by them.

(d) applied currents below 1mA have no significant effect on the PCMO film, but at higher current (≥1mA), the formation of ferromagnetic clusters in the PCMO is initiated;

In what follows we try to explain our experimental observations on the basis of charge order melting in the PCMO film due to both substrate induced strain and applied current leading to the formation of ferromagnetic clusters and consequently the injection of spin polarized quasi-particles into the superconducting YBCO layer. It is known that an electric field or substrate induced strain can induce insulator-metal transition in PCMO thin films [7-13]. In charge ordered PCMO thin film, an electric current or substrate induced strain brings about a competition between CO and FM phases which may lead to the formation of clusters of FM phase dispersed in a matrix of the charge ordered PCMO. FM clusters formed in a CO matrix is schematically illustrated in figure 6.5(a) [31]. These FM clusters can grow in size with increase in applied magnetic field. For the measurement of resistance, the current is passed through the contacts A and D, while the voltage is measured across the contacts P and Q which is shown in figure 6.5(b). The PCMO films in both the top and bottom layers can be modeled as a series of interconnected network of N charged ordered regions having a relatively high resistance R_{CO} and N low resistance FM clusters having a relatively low resistance R_{FM} as shown schematically in fig.6.5 (c). The values of these resistances between the contacts A and D on the top PCMO layer are denoted as $R_{COT}(i)$ and $R_{FMT}(i)$ (i=1 to N) respectively whereas the resistance between the points E and F on the bottom PCMO layer are denoted as $R_{COB}(i)$ and $R_{FMB}(i)$ (i=1 to N) respectively. In this figure, the path BC denotes the low resistive path through the YBCO film which is also modeled to be comprised of N resistances $R_{YB}(i)$, connected in series. In this schematic, there are N parallel resistive paths between the lines AD and BC traversing through the thickness of PCMO (ie perpendicular to the surface of the film) whose values are denoted as $R_{COT}(d_i)$.

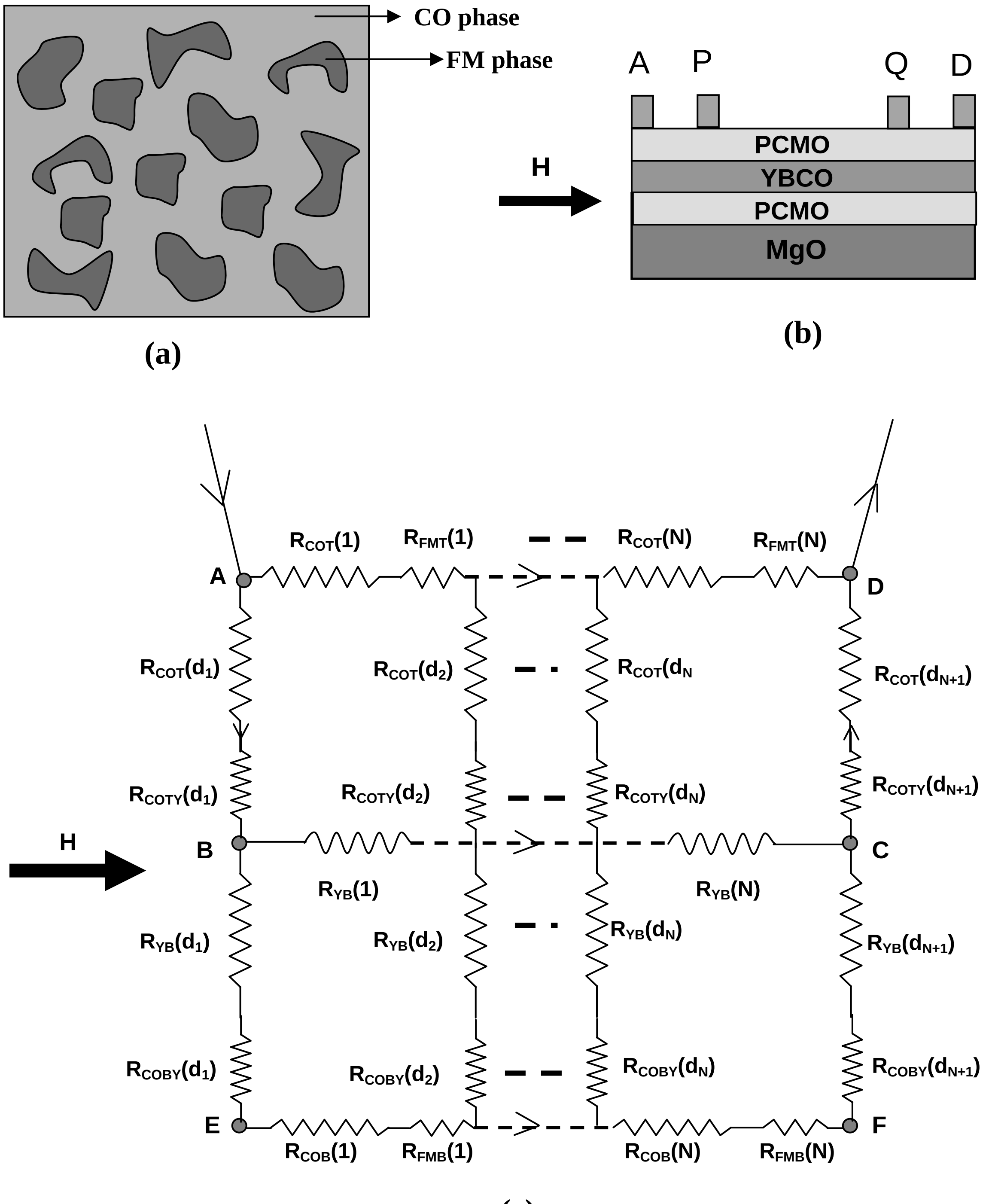

(a)

(b)

(c)

Fig. 6.5. *(a) Schematic illustration of the FM clusters dispersed in a CO background of the PCMO film, which are expected to form under the application of suitable external perturbation. (b) Schematic cross section of the PCMO/YBCO/PCMO trilayer heterostructure deposited on MgO substrate indicating the points at which electrical contacts were established for the measurement of resistance and (c) the schematic equivalent resistance circuit corresponding to (a) and (b).*

Similarly there are N parallel low resistive path between the lines BC and EF crossing the thickness of YBCO layer and these resistive paths are denoted as $R_{YB}(d_i)$. Here R_{COTY} is the resistance associated with the interface between the top PCMO and YBCO layer whereas R_{COBY} is the resistance associated with the interface between the bottom PCMO and YBCO layer. As the value of R_{CO} is much greater than that of R_{FM} and R_{YB}, we can neglect the current flowing through the intermediate high resistive paths namely $R_{COT}(d_2)$ to $R_{COT}(d_N)$ etc for simplicity.

Analytical evaluation of the actual effective resistance (R_{res}) between the points A and D for such a complex resistive network is not straightforward. However, we assume that R_{res} is a function of all the resistances present in the network. Hence, we may formally write

$$R_{res} = R_{res}\,(R_{COT}, R_{FMT}, R_{COTY}, R_{YB}, R_{COBY}, R_{COB}, R_{FMB}) \qquad \ldots\ldots\ldots\ldots\ldots\ldots\ldots\ldots \quad \mathbf{(1)}$$

Differentiating the above equation with respect to temperature, we get

$$\frac{dR_{res}}{dT} = \frac{\partial R_{res}}{\partial R_{COT}}\frac{dR_{COT}}{dT} + \frac{\partial R_{res}}{\partial R_{FMT}}\frac{dR_{FMT}}{dT} + \frac{\partial R_{res}}{\partial R_{COTY}}\frac{dR_{COTY}}{dT} + \frac{\partial R_{res}}{\partial R_{YB}}\frac{dR_{YB}}{dT} + \frac{\partial R_{res}}{\partial R_{COBY}}\frac{dR_{COBY}}{dT} + \frac{\partial R_{res}}{\partial R_{COB}}\frac{dR_{COB}}{dT} + \frac{\partial R_{res}}{\partial R_{FMB}}\frac{dR_{FMB}}{dT} \qquad \ldots\ldots\ldots\ldots\ldots\ldots\ldots\ldots\ldots\ldots \quad \mathbf{(2)}$$

It is possible to account for all the experimental observations on the two trilayers using this simplified picture:

(1) It may be noted that the bottom PCMO layer of the trilayer film, which is a charge ordered insulator, has little effect on the resultant effective resistance of the network unless the resistance of the path EF is substantially reduced, for example, by transformation to a conducting FM phase by the application of an external

perturbation. Also not much current is likely to flow through the path AD compared to the path A-B-C-D since the resistance of the former is much higher than that of the latter. Hence, as the sample is cooled from room temperature to ~100 K (where a hump is observed in the temperature dependence of resistance), the overall resistance is simply defined as

$$R_{COT}(d_1) + R_{COT}(d_{N+1}) + NR_{YB} + R_{COTY}(d_1) + R_{COTY}(d_{N+1})$$

As R_{CO} is much higher than the other resistances in this expression, the overall resistance in this temperature range is dominated by R_{CO} and, hence, the temperature dependence of the effective resistance shows a semiconductor-like behavior with a negative temperature coefficient of resistance.

(2) The total thickness of the strained film is somewhat lower than that of the relaxed film. In view of this, the resistance of the relaxed film may be expected to be less compared to that of the strained film. Also slight difference in the positions of the contacts could account for different values of resistance observed for the two trilayers.

(3) From eq. (2), it is evident that the temperature dependent rate of change of R_{res} is greatly influenced by temperature dependent rate of change of R_{COT}, R_{FMT}, R_{YB}, R_{COB}, R_{COTY}, R_{FMB} and R_{COBY}. Hence, the temperature dependence of the measured resistance is decided by a competition between the temperature dependence of the individual components of the network (i.e. R_{COT}, R_{FMT}, R_{YB}, R_{COB}, R_{FMB}, R_{COTY} and R_{COBY}) in different ranges of temperature. As the temperature reaches ~ 100K, dR_{YB} / dT assumes large positive values which are larger in magnitude compared to the value of dR_{CO} / dT (which is negative). This

causes dR_{YB} / dT to dominate in determining the net behavior of the resistance at temperatures just below ~100 K and R_{res} falls with further decrease in temperature. The resistance, $R_{COBY,}$ in the network that represents the scattering of charge carriers at the interface between PCMO and YBCO begins to dominate quickly thereafter and its temperature dependence (dR_{COBY} / dT) gives rise to the second hump in the temperature dependence of the measured resistance. The characteristic shape of the second hump in the two trilayers shows that the dR_{COBY}/dT is a crucial factor in this temperature range. The bottom PCMO in the relaxed film is in the charge ordered state, whereas in the strained film, it is in the phase separated state where both charge ordered and FM phases coexist with FM phase dispersed in the charge ordered matrix. This difference influences the scattering of charge carriers at the interface and affects the relative height of the second hump in the two trilayers as shown in figure 6.4.

(4) The experimental data for strained film shows that the hump height decreases when a magnetic field is progressively increased from 0 T to 8 T (see figure 6.4(a) and 6.4(c)). In the strained film, the FM clusters are already formed in the bottom layer PCMO film due to substrate induced strain and these FM clusters may be expected to grow in size when a magnetic field is applied. This results in a progressive decrease in the resistance of the path EF in fig.6.5(c) due to the increase in the number and size of the FM clusters in the bottom PCMO layer. Since the FM clusters are metallic, this could account for the observed decrease in resistance on application of magnetic field. But in the case of relaxed film, the bottom layer PCMO is not subjected to much lattice strain. The application of

magnetic field tends to increase the resistance associated with $R_{COT}(d_1)$ and $R_{COT}(d_{N+1})$ due to an increase in the path length traversed by the charge carriers; this can account for the observed increase in the resistance when a magnetic field is applied to the relaxed film. The resistance observed at the peak of the second hump is taken as a parameter R_P, whose variation with the applied magnetic field has been shown in figure 6.6. for both strained and relaxed films at applied currents of 1 mA and 5 mA. The experimental data shows that, for the strained film, $\Delta R_P/\Delta H$ is -2.14 ohm/Tesla at 1mA current and -2.55 ohm/Tesla at 5 mA current. In the case of relaxed film, $\Delta R_P/\Delta H$ is +0.78 ohm/Tesla at 1mA and +0.60 ohm/Tesla at 5 mA current respectively. The increased value of $\Delta R_P/\Delta H$ at different currents reveal that the applied current has a tendency to enhance the growth of FM phase in top PCMO layer in both the films.

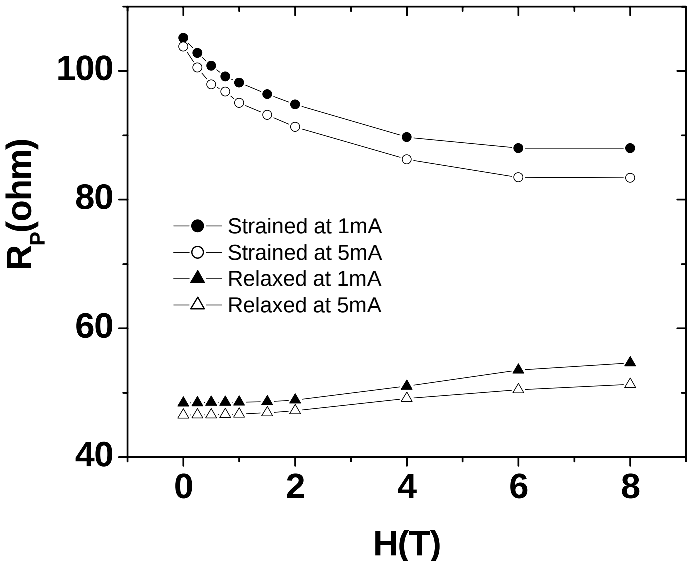

Fig. 6.6. *H vs R_P plot for strained and relaxed film at 1mA and 5mA applied current.*

(5) As the temperature is decreased further, a positive magnetoresistance is observed in both the films. This is because of the higher value of resistance of $R_{CO}(d_1)$ and $R_{CO}(d_{N+1})$ at low temperatures and also as the applied magnetic field increases the path length of the charge carriers traversing through the thickness of the top PCMO layer. Thus the values of $R_{CO}(d_1)$ and $R_{CO}(d_{N+1})$ tend to increase further leading to an increase in the observed resistance when a magnetic field is applied.

(6) The temperature at the midpoint of each falling resistance curve is denoted by T_{C-mid}. Suppression of T_{C-mid} as the magnetic field increases is shown in fig.6.7 for the strained as well as relaxed films at applied currents of 1mA and 5mA. It is seen from fig.6.7 that the rate of suppression of T_{C-mid} is ~3.5K/Tesla and ~1.8K/Tesla respectively for the strained and the relaxed films. It may also be noted that the suppression of T_{C-mid} at a fixed applied magnetic field is observed to be ~1.0 K/mA and ~ 0.38 K/mA respectively for the strained and the relaxed films. It has to be noted here that the value of T_C suppression due to applied current for trilayer relaxed film is almost similar to that of the bilayer film (~0.35 K/mA) described in chapter 4.

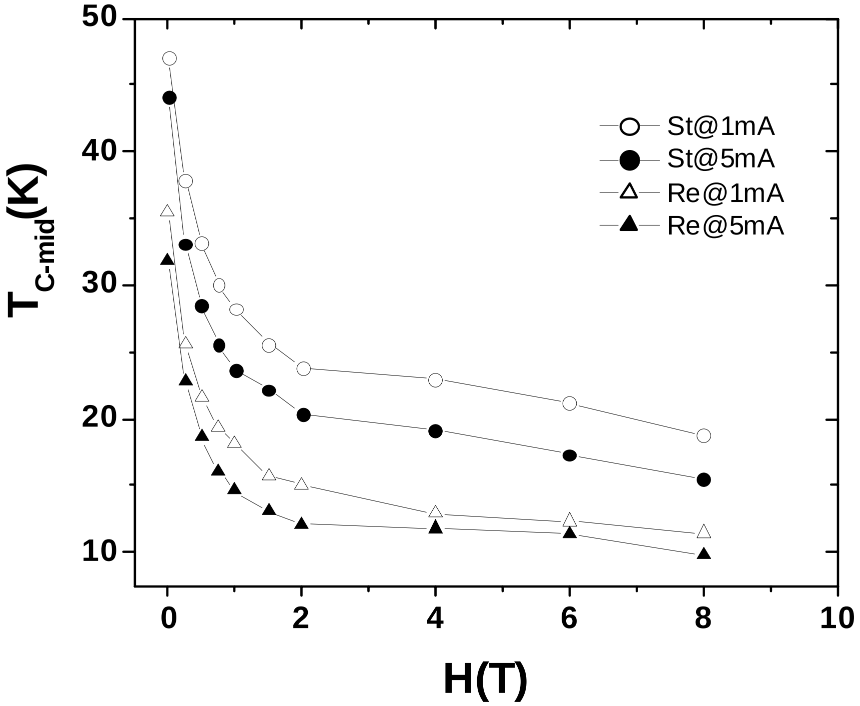

Fig. 6.7. *T_C taken at the mid point of the transition curve plotted against the applied magnetic field ranging from 0T to 8T.*

These facts can be explained on the basis of effects such as proximity effect and spin injection effect [24-29, 32, 33] associated with the FM clusters generated inside the PCMO layer on the superconducting properties of the adjacent YBCO layer. First, we consider the experimentally observed behavior for the strained film. As the magnetic field is increased the tiny FM clusters inside the strained bottom layer of PCMO grow further in size. This decreases the overall resistance of the bottom PCMO layer favouring a flow of higher current flow through it. The increase in the number and size of the FM clusters as well as injection of charge carriers from the bottom PCMO layer have two prominent detrimental effects on the superconductivity of the YBCO layer. First, the FM clusters suppress the superconducting transition temperature T_c of the YBCO layer on account of the proximity effect driven by the exchange field inside the FM cluster. Second, the injection of quasi-particles emanating from metallic FM clusters into the YBCO layer can also depress the superconducting transition temperature T_c. The mechanism of T_c suppression due to this effect has been described in the preceding chapters (chapter 4 and chapter 5). It may be noted that the top PCMO layer also contributes to the suppression of T_c of the YBCO layer as it supports the formation of FM clusters when applied current exceeds 1mA. In case of the relaxed film, the bottom PCMO layer is not subjected to substrate induced strain and hence the situation is not conducive to the formation of FM clusters in the bottom PCMO layer in the relaxed film. Thus, in the relaxed film, T_c suppression due to the proximity effect and injection of charge carriers associated with FM clusters in the bottom PCMO layer is not significant. FM clusters formed in the top PCMO layer at applied currents exceeding 1mA lead to a comparatively smaller suppression of the superconducting transition temperature T_c of the sandwiched YBCO layer. The increase in the applied current to 5 mA is observed to further suppress the T_c value in both the strained as well as the relaxed films as shown in figure 6.7. It may be noted that the T_c of the relaxed film is observed to be lower than the T_c of the strained film at zero external magnetic field in contradiction with the normal expectation. This is probably because the YBCO film deposited on the thinner PCMO layer in the strained trilayer is of better quality compared to that deposited on the relatively thicker PCMO in the relaxed trilayer. The XRD patterns for the strained and relaxed trilayers lend credence to this as explained earlier. This rationalizes the observation of a somewhat higher T_c for the YBCO in the strained trilayer as compared to that observed for the relaxed trilayer.

(7) At low temperatures (between 45K to 70K), a shoulder-like plateau in the temperature dependence of electrical resistivity has been observed for both the strained as well as the relaxed films. The rapid fall in the observed resistance of the trilayer below the plateau region in the R(T) curve is attributed to the transition from the normal metallic phase of the YBCO layer to the superconducting state. At the onset of superconductivity, YBCO layer begins to exhibit a large and positive dR_{YB}/dT, which dominates the temperature dependence of all other resistors in the network and the observed resistance rapidly falls to zero as the specimen is cooled further. When the YBCO layer becomes superconducting, applied current gets short circuited solely through the sandwiched YBCO layer and the observed resistance R_{res} eventually becomes zero. The temperature at which the zero resistance state is attained depends on the characteristics of the deposited films as well as external parameters such as magnetic field, electric field (current) and substrate induced strain.

In an another set of experiments, resistance of these two trilayers has been measured at applied magnetic field ranging from 0 T to 8 T at three different fixed temperatures, namely 58 K, 27 K and 8 K. Figure 6.8 shows the variation of the observed resistance as a function of magnetic field for the strained and the relaxed films at applied currents of 1mA and 5 mA.

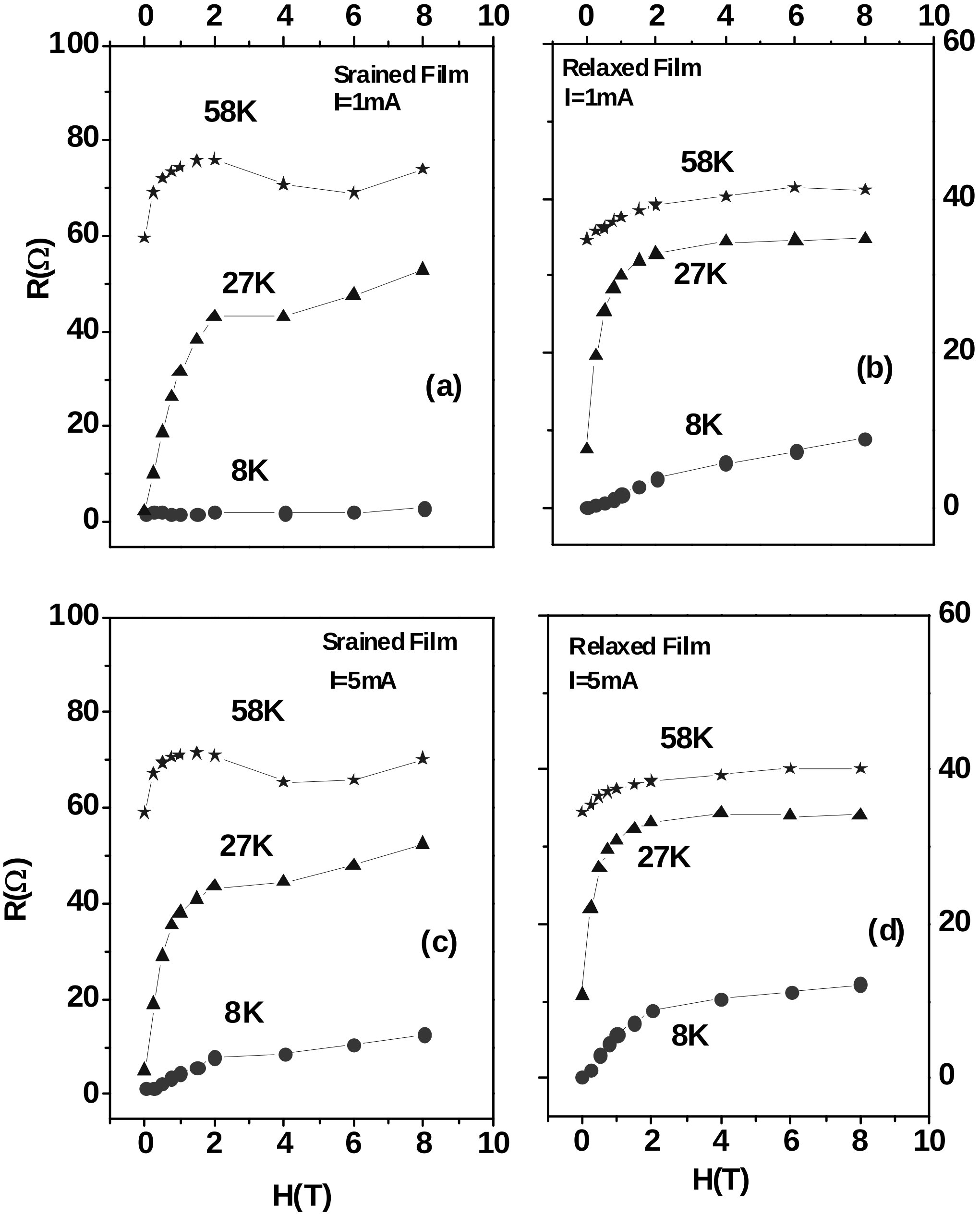

Fig. 6.8. *Variation of the resistance of the strained and relaxed trilayers at applied current of 1mA (a and b) and 5mA (c and d) at selected temperatures.*

For the relaxed film, resistance is observed to monotonically increase relatively quickly and saturates as the applied magnetic field increases at all the three temperatures. At 27 K, increase in resistance as the magnetic field is increased is relatively rapid compared to that observed at 58 K or 8 K. For the strained film, the experimental data shows similar behavior at 8 K and 27 K but at 58 K, observed resistance shows a non-monotonic variation with magnetic field. At 58 K, the observed resistance of the strained film initially increases upto ~1.5 T, begins to decrease as the magnetic field is increased from 1.5 T to 5.5 T and increases again as the magnetic field is increased beyond 5.5T. These experimental observations may be explained using equation (3) which represents the derivative of equation (1) with respect to the magnetic field, H:

$$\frac{dR_{res}}{dH} = \frac{\partial R_{res}}{\partial R_{COT}}\frac{dR_{COT}}{dH} + \frac{\partial R_{res}}{\partial R_{FMT}}\frac{dR_{FMT}}{dH} + \frac{\partial R_{res}}{\partial R_{COTY}}\frac{dR_{COTY}}{dH} + \frac{\partial R_{res}}{\partial R_{YB}}\frac{dR_{YB}}{dH} + \frac{\partial R_{res}}{\partial R_{COBY}}\frac{dR_{COBY}}{dH} + \frac{\partial R_{res}}{\partial R_{COB}}\frac{dR_{COB}}{dH} + \frac{\partial R_{res}}{\partial R_{FMB}}\frac{dR_{FMB}}{dH} \qquad \text{..............(3)}$$

It may be noted that the magnetic field (H) has been applied parallel to the plane of the film (see figure 6.5.b), i.e., perpendicular to the resistive paths along A-B and C-D traversing through the thickness of the top PCMO layer(see figure 6.5.c). In this situation, there is an increase in the path length traversed by the charge carriers when a magnetic field is applied. Thus in equation (3), dR_{COT}/dH factor dominates by increasing its value. This effectively results in higher value of dR_{res}/dH on application of a magnetic field giving rise to a positive magnetoresistance at a constant current. But further increase in applied magnetic field favours the growth of FM clusters inside the top PCMO leading to a decrease in the value of R_{FMT} and dR_{FMT}/dH with increasing magnetic field. The actual variation of observed resistance as a function of magnetic field in this range is dependent on the balance between the increase in the value of dR_{COT}/dH and the decrease in the value of dR_{FMT}/dH. This balance causes the observed resistance to saturate with further increase in the magnetic field. In the case of the strained film, the FM clusters in the bottom PCMO layer formed by strain induced charge order melting lead to a rapid decrease in the value of dR_{FMB}/dH. At relatively higher temperatures (>58 K), and at a high magnetic field, the magnitude of dR_{FMB}/dH exceeds dR_{COT}/dH leading to the experimental observation of a decrease in resistance as the magnetic field is increased from ~1.5 T to ~5 T. Beyond this field, however, formation of FM clusters and dR_{FMB}/dH have a tendency to saturate. With no further decrease possible in the value of dR_{FMB}/dH beyond 5 T, dR_{COT}/dH begins to dominate and the observed resistance R_{res} starts increasing as the magnetic field is increased beyond 5 T.

It may be noted that the above discussion is qualitative and accounts for the observed experimental trends. Based on the above explanations, a simplified mathematical expression can be derived which can be used to model the transport behaviour of a multilayer heterostructure thin film consists of superconductor and manganites. A highly simplified account for the behavior of the resultant resistance of the network sketched in fig.6.5(c) may be found for the trilayer geometry where the resultant resistance is dependent on temperature (T), applied magnetic field (H), applied current (I) and substrate induced strain (S). We denote the resistance of top layer PCMO, bottom layer PCMO and middle layer YCBO by R_{COT}, R_{COB} and R_{YB} respectively. Then R_{res} is a function of these three resistances and may be expressed as,

$$R_{res} = R_{res}(R_{COT}, R_{COB}, R_{YB}) \qquad \text{----------(4)}$$

We note that the resistances of the PCMO and YBCO layers are influenced by some external parameters such as T, H, I and S. Since the top PCMO layer is not subjected to substrate induced strain, R_{COT} may be expressed as

$$R_{COT} = R_{COT}(T, H, I) \qquad \text{--------- (5)}$$

Similarly R_{COB} can be expressed as,

$$R_{COB} = R_{COB}(T, H, I, S) \qquad \text{--------- (6)}$$

The resistance of the YBCO layer may be taken to depend on temperature only:

$$R_{YB} = R_{YB}(T) \qquad \text{--------- (7)}$$

Under the above assumptions, we may write

$$dR_{res} = \frac{\partial R_{res}}{\partial R_{COT}} dR_{COT} + \frac{\partial R_{res}}{\partial R_{COB}} dR_{COB} + \frac{\partial R_{res}}{\partial R_{YB}} dR_{YB} \qquad \text{--------- (8)}$$

$$dR_{COT} = \frac{\partial R_{COT}}{\partial T} dT + \frac{\partial R_{COT}}{\partial H} dH + \frac{\partial R_{COT}}{\partial I} dI \qquad \text{---------- (9)}$$

$$dR_{COB} = \frac{\partial R_{COB}}{\partial T} dT + \frac{\partial R_{COB}}{\partial H} dH + \frac{\partial R_{COB}}{\partial I} dI + \frac{\partial R_{COB}}{\partial S} dS \qquad \text{----------- (10)}$$

$$dR_{YB} = \frac{\partial R_{YB}}{\partial T} dT \qquad \text{---------- (11)}$$

Now, substituting equations (9), (10) and (11) into equation (8), we get

$$dR_{res} = \frac{\partial R_{res}}{\partial R_{COT}} [\frac{\partial R_{COT}}{\partial T} dT + \frac{\partial R_{COT}}{\partial H} dH + \frac{\partial R_{COT}}{\partial I} dI] + \frac{\partial R_{res}}{\partial R_{COB}} [\frac{\partial R_{COB}}{\partial T} dT + \frac{\partial R_{COB}}{\partial H} dH + \frac{\partial R_{COB}}{\partial I} dI + \frac{\partial R_{COB}}{\partial S} dS] + \frac{\partial R_{res}}{\partial R_{YB}} [\frac{\partial R_{YB}}{\partial T} dT]$$

\- --------- (12)

This may be expressed as a general form:

$$dR_{res} = \sum_{R_{f_i}, f_i} \frac{\partial R_{res}}{\partial R_{f_i}} \frac{\partial R_{f_i}}{\partial f_i} df_i \qquad \text{----------- (13)}$$

where $R_{fi} =$ R_{COT}, R_{COB} and R_{YB}

f_i = T, H, I and S

Integrating both sides of equation (13), it can be expressed as

$$R_{res} = \int \sum_{R_{f_i}, f_i} \frac{\partial R_{res}}{\partial R_{f_i}} \frac{\partial R_{f_i}}{\partial f_i} df_i \qquad \text{----------- (14)}$$

Eqn. (14) may finally be expressed as,

$$R_{res} = \sum_{R_{f_i}, f_i} \int \frac{\partial R_{res}}{\partial R_{f_i}} \frac{\partial R_{f_i}}{\partial f_i} df_i \qquad \text{----------- (15)}$$

The above expression can be applied to the N layers in a multilayer thin film of manganite and YBCO.

In any resistive network system having a fixed number of layers (N), $\frac{\partial R_{res}}{\partial R_{f_i}}$ may be assumed to be a constant, say, C_{fi}, which is dependent on the network geometry but not on factors such as temperature T, magnetic field H, applied current I etc. The above equation then becomes

$$R_{res} = \sum_{R_{f_i}, f_i} C_{f_i} \int \frac{\partial R_{f_i}}{\partial f_i} df_i \qquad \text{-----------(16)}$$

Equation (16) shows that if the dependence of resistance of each individual layer on parameters f_i is known, the characteristic transport behavior of the multilayer heterostructure can be predicted based on the above explained model.

As shown in fig.6.4, there is a considerable broadening of the resistive transition of the PCMO/YBCO/PCMO trilayer to the superconducting state when a magnetic field is applied. Such broadening of the resistive transition under the application of magnetic field is known to arise due to the dissipation of energy caused by the motion of vortices [34-36]. For finite current density, the Lorentz force is sufficiently strong that the vortices can overcome a certain class of pinning barriers leading to flux flow, and consequently, generation of voltage. Because of this, above the glass transition temperature $T_g(H)$, the observed resistance is nonzero and the temperature dependent resistivity $\rho(T)$ is of the thermally activated type and follows an Arrehenius law. The temperature dependent resistance is described by the equation, $R(T,H)= R_0 \exp[-U_0(T,H)/k_BT]$ where U_0 is the flux flow activation energy which depends on temperature and the applied field H, R_0 is the prefactor and k_B is the Boltzman constant. Activaton energy U_0 can therefore be obtained from the slope of the linear part of Arrehenius plot of R(T) at temperatures ostensibly below T_c. The value of U_0 has been estimated using this method for both the trilayers (strained and relaxed) at different values of applied magnetic field and at two different values of applied current (1mA and 5 mA). The variation of U_0 as a function of magnetic field is shown in figure 6.9 for both the strained as well as the relaxed film.

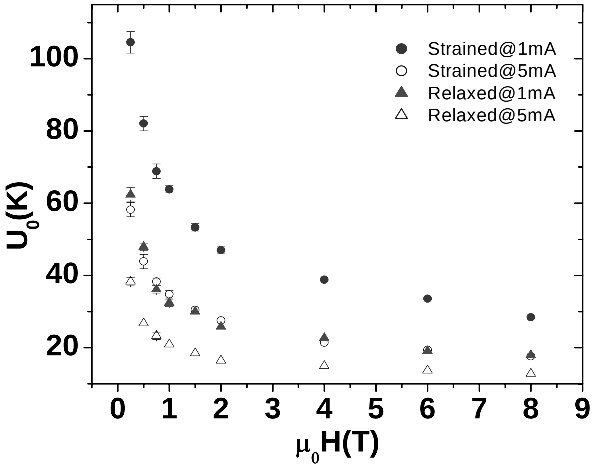

Fig. 6.9. *Activation energy plot for different applied magnetic field ranging from 0 T to 8 T.*

It may be noted from figure 6.9 that the activation energy for the strained film is found to be higher compared to that for the relaxed film. Also, the values of U_0 for the strained film at applied currents of 1mA and 5 mA are found to be higher compared to the corresponding values for the relaxed film. The higher value of U_0 for the strained film shows that the vortex pinning is relatively stronger in the strained film compared to the relaxed one. This is because of the presence of FM clusters inside the bottom PCMO layer due to the substrate induced strain in the trilayer. The presence of these FM clusters enhances pinning of vortices participating in the thermally activated flux flow. When the applied current is increased from 1mA to 5 mA, there is an increase in the number and the size of the FM clusters which further enhances the vortex pinning, accounting for the observation of lower value of U_0 at lower applied currents.

6.4 Conclusion:

PCMO/YBCO/PCMO trilayer heterostructures with different thicknesses of the individual layers have been grown on MgO substrate using the pulsed laser deposition technique. In one trilayer, the thickness of the bottom PCMO layer was selected to be relatively low (~ 40 nm) compared to that in the other (~100 nm). The trilayer with ~40 nm thick bottom PCMO layer was designated as the “strained film”, while the trilayer with ~100 nm thick bottom PCMO layer was designated as the relaxed film. Both the trilayers were characterized by XRD technique, which confirmed the growth of PCMO and YBCO layers on the MgO substrate. Four probe measurement technique was used to characterize the transport behaviour under the externally applied magnetic field (0 to 8 T) and applied current (1mA and 5 mA). Analysis of the temperature dependence of the resistance of the trilayers in the presence of different values of applied magnetic field has been carried out to delineate the role of the FM clusters in the PCMO film. The experimental data on the strained and the relaxed films may be accounted for by invoking the nucleation and growth of FM clusters in the PCMO film promoted by experimental variables such as strain, magnetic field and applied current. Near the “hump” region, the magnetoresistance was observed to be negative for the strained film and positive for the relaxed film. The suppression of the superconducting transition temperature T_c of the YBCO layer was found to be relatively higher for the strained film compared to that for the relaxed film. This was ascribed to the spin injection and proximity effects due to the growth of FM clusters inside the PCMO layer. The activation energy estimated for both the trilayers reveals that the vortex pinning force is higher for the strained film compared to that for the relaxed film, confirming the role played by strain induced FM clusters in the bottom PCMO film of the strained trilayer.

Reference:

[1] H. Yoshizawa, H. Kawano, Y. Tomioka and Y. Tokura *Phys. Rev. B 52, 13 145 (1995).*

[2] H.Y. Hwang, S. W.Cheong, P.G. Radaelli, M. Marezo and B. Batlogg *Phys. Rev. Lett. 75, 914 (1995)*

[3] V. N. Smolyaninova, K. Ghoh and R. L. Greene *Phys. Rev. B 58, 14 725 (1998)*

[4] B. Raveau, A. Maignan and V. Caignaert *J. Solid State Chem. 117, 424 (1995)*

[5] Anthony Arulraj, Amlan Biswas, A. K. Raychaudhuri, C.N.R. Rao, P. M. Woodward, T. Vogt, D. E. Cox and A. K. Cheetham *Phys. Rev. B 57, 8115 (1998).*

[6] A. Asamitsu, Y. Tomioka, H. Kuwahara and Y. Tokuta, *Nature **388**, 50 (1997).*

[7] V. Kiryukhin, D. Casa, J. P. Hill, B. Kelmer, A. Viglinate, Y. Tomioka and Y. Tokura, Nature ***386**, 813 (1997).*

[8] W. S. Tan, L. Yang, X. S. Wu, S. S. Jiang, T. L. Kam, J. Gao, J. Wang and Z. H. Wu *Physica C 384,437 (2003)*

[9] Y. Tomioka, a. Asamitsu, H. Kuwahara, Y. Morotima and Y. Tokura *Phys. Rev. B 53, 1689 (1996).*

[10] H. Yoshizawa, R.Kajimoto, H. Kawano, Y. Tomioka and Y. Tokura *Phys. Rev. B 55, 2729 (1997).*

[11] M. Hervieu, A. Barnabe, C. Martin, A. Maignan and B. Raveau *Phys. Rev. B 60, 726 (1999).*

[12] K. Miyano, T. Tanaka, Y. Tomioka and Y. Tokura *Phys Rev. Lett. 78, 4257 (1997).*

[13] Dipak Kumar Baisnab, T. Geetha Kumary, A. T. Satya, Awadhesh Mani, J. Janaki, R. Nithya, L. S. Vaidhyanathan, M. P. Janawadkar and A. Bharathi *J. Magn. Magn. Mater. 323, 2823 (2011)*

[14]Y. Tokura and Y. Tomioka *J. Magn. Magn. Mater 200,1 (1999)*

[15] Y. Tomioka, A Asamitsu, Y Morimoto and Y tokura *J. Phys. Soc. Japan 64, 60 (1995)*

[16] Jolanta Stankiewicz, Javier Sese, Joaquin Garcia, Javier Blasco and Conrado Rillo *Phys. Rev. B 61, 11 236 (2000)*

[17] Shivani Srivastava, Navneet K. Panday, P. Padhan and R. C. Budhani *Phys. Rev. B 62, 13 868 (2000)*

[18] W. Prellier, Ch. Simon, A. M. Haghiri-Gosnet, B. Mercey, and B. Raveau, *Phys. Rev. B, **62**, R16337 (2000).*

[19] W. Prellier, A. M. Haghiri-Gosnet, B. Mercey, Ph. Lecoeur, M. Hervieu, Ch. Simon and B. Raveau, *Appl. Phys. Lett. **77**, 1023 (2000).*

[20] A. M. Haghiri-Gosnet, M. Hervieu, Ch. Simon, B. Mercey, and B. Raveau, *J. Appl. Phys., **88**, 3545 (2000).*

[21] W. Prellier, E. Rauwel Buzin, B. Mercey, Ch. Simon, M. Hervieu, and B. Raveau, *J. Phys. Chem. Solids, **64**, 1665 (2003).*

[22]B. Mercey, J. Wolfman, W. Prellier, M. Hervieu, Ch. Simon, B. Raveau, *Chem. Mater. 12, 2858 (2000)*

[23]C. S. Nelson, J. P. Hill, D. Gibbs, M. Rajeswari, A. Biswas, S. Shinde, R. L. Greene, T Venkatesan, A. J. Millis, F. Yokaichiya, C Giles D Casa, C. T. Venkataraman and T. Gog *J. Phys.: Condens. Matter 16, 13-27 (2004)*

[24] Daniel Hsu, L. G. Lin, C. P. Chang, C. H. Chen, C. H. Chiang, W. C. Chan and W. F. Wu *J. Appl. Phys. 103, 07C710 (2008)*

[25] J. G. Lin, Daniel Hsu, W. F. Wu, C. H. Chiang and W. C. Chang *J. Appl. Phys., 101, 09G106 (2007)*

[26] Hanns-Ulrich Habermeier, Soltan Soltan and Joachim Albrecht *Physica C 460-462, 32 (2007)*

[27] J. G. Lin, S. L. Cheng, C. R. Chang and D. Y. Xing *JAP 98, 023910 (2005)*

[28] Daniel Hsu, L. G. Lin, C. P. Chang, C. H. Chen, W. F. Wu,C. H. Chiang and W. C. Chan *Appl. Phys. Lett. 90, 162504 (2007)*

[29] W. Westhauser, S. Schramm, J. Hoffmann and C. Jooss *Eur. Phys. J. B 53, 323 (2006)*

[30] Dipak Kumar Baisnab, T. Geetha Kumary, A. T. Satya, Awadhesh Mani, R. Nithya, L. S. Vaidhyanathan, M. P. Janawadkar and A. Bharathi *J. Appl. Phys. 111, 113910 (2012)*

[31] Elbio Dagotto, Nanoscale Phase Seperation and Colossal Magnetoresistance: The Physics of Manganites and Related Compounds, May27, 2002, Springer-Verlag

[32] Y. Gim, A. W. Kleinsasser, and J. B. Barner *J.Appl. Phys. Vol.90, No. 8, 4063 (2001)*

[33] G A Ovsyannikov, K Y Constantinian, Yu V Kislinski, A V Shadrin, A V Zaitsev, A M Petrzhik, V V Demidov, I V Borisenko, A V Kalabukhov and D Winkler *Supercond. Sci. Technol. 24, 055012 (2011)*

[34] P. W. Anderson, *Phys. Rev. Lett. 9, 309 (1962)*

[35] P. W. Anderson and Y. B. Kim *Rev. Mod. Phys. 36, 39 (1964)*

[36] T. T. M. Palstra, B. Batlogg, R. B. Van Dover, L. F. Schneemeyer and J. V. Waszczak, *Phys. Rev. B 41, 6621(1990)*

Chapter 7

Summary and Outlook

7.1 Conclusion:

The charge ordered (CO) state of $Pr_{0.5}Ca_{0.5}MnO_3$ is known to be unstable under a variety of external perturbations such as magnetic field, substrate induced strain and electric field [1-7]. In thin film $Pr_{0.5}Ca_{0.5}MnO_3$ / $YBa_2Cu_3O_7$ (PCMO/YBCO) heterostructures, the CO melting phenomena can be used to control the injection of spin polarized charge carriers into the high temperature superconductor (HTS) and, hence, influence its superconducting properties [8-12]. In this thesis, the effect of substrate induced strain and applied electric and magnetic fields are used to generate FM clusters in the PCMO layer, which in turn affects the superconducting properties of the YBCO layer in the PCMO/YBCO thin film heterostructures. In addition the individual and cumulative effects of these external perturbations on the superconducting properties of the YBCO layer in the PCMO/YBCO thin film heterostructures have also been investigated.

In order to prepare PCMO/YBCO thin film heterostructure, at first the optimization of the process parameters for the deposition of high quality (viz. relatively high superconducting transition temperature T_c, surface smoothness etc) thin films of YBCO was carried out. Here we have adopted the Pulsed Laser Deposition (PLD) technique to deposit YBCO thin films on different substrates viz., STO, LAO and MgO. The deposited thin films were characterized for structure by X-ray diffraction. The physical property measurement undertaken were electrical transport measurements. X-ray Diffraction data shows c-axis oriented growth of YBCO film when deposited on all the three substrates. YBCO film grown on STO substrate exhibited the maximum superconducting transition temperature T_c of ~92K obtained from resistance measurements whereas the T_c for the YBCO film grown on MgO substrate was slightly lower at 88.4 K. The measurements of electrical resistance as a function of temperature were performed at low temperatures for different applied currents ranging from 50μA to 200mA and the measurements show only a relatively small change in the superconducting transition temperature as a function of applied current. A comparative study has been carried out for both as deposited and post-deposition-annealed thin films of YBCO deposited on STO substrate, which shows that, without proper annealing, the YBCO film can even show a negative temperature coefficient of resistance.

Charge ordered PCMO undergoes a phase transition from charge ordered antiferromagnetic insulating state to charge delocalized ferromagnetic metallic (FM) state under an external perturbation like magnetic field, electric field, substrate induced strain etc. Films with different thicknesses (ranging from 25nm to 200nm) were deposited on larger lattice mismatched (~9.4 %) MgO substrate to demonstrate the substrate induced strain effect on CO-melting phenomena in charge ordered PCMO film. A decrease in resistivity and the charge order transition temperature was observed with decrease in the film thickness. A narrow range of film thickness for PCMO (35nm and 42nm) only exhibited the CO melting and metal insulator transition (MIT) under the applied magnetic field upto 12 T. This FM state of PCMO can then be judiciously used as a source of spin injection into the HTSC. A variety of bilayer and trilayer thin film heterostructures of PCMO and YBCO have been fabricated on different substrates like MgO, $SrTiO_3$ (STO) and $LaAlO_3$ (LAO) to demonstrate the spin injection effect in these heterostructures. Measurement of magnetoresistance has been performed on PCMO/YBCO bilayer thin film with different values of applied current (10μA to 40mA) and magnetic fields (0T to 12T). Applied current(I) has been used here as an external perturbation to induce localized clusters of FM state inside the matrix of charge ordered PCMO layer. Based on the results of these measurements, it is inferred that the charge order melting is initiated in PCMO for I>1mA at H=0 T leading to the formation of isolated tiny clusters of the ferromagnetic phase. The size of these FM clusters increases with increase in the magnitude of applied current. The T_c of the underlying YBCO layer is thus suppressed by injection of quasi-particles emanating from the top PCMO layer.

T_c of the YBCO layer is decreased not only by the quasi-particle spin injection effects, but also by the direct proximity of the FM phase; indeed the latter effect can play a crucial role in determining the overall behavior of the system. This fact can be cleverly used to control the T_c of the superconductor even without the direct electrical contact with the FM phase. This behaviour has been demonstrated in another experiment where magneto-resistance measurements have been performed on PCMO/YBCO bilayer deposited on STO substrate using an in-situ masking technique to cover ~ 50% area of the bottom YBCO layer by a top PCMO layer with a view to delineate the effects of spin injection and proximity effect of ferromagnetic layer on the superconducting properties. The T_c seems to be higher and the current induced decrease in T_c smaller on the YBCO portion not masked by PCMO, compared to the corresponding behavior observed for YBCO/PCMO bilayer. Flux pinning parameters of the YBCO film in the two regions were deduced from an analysis of the Arrhenius fit of R(T) versus 1/T using thermally activated flux flow (TAFF) model. The activation energy in the part of the YBCO film covered with PCMO was found to be higher compared to that for the part which is not covered by PCMO under applied current and magnetic field. The results clearly show that while T_c suppression effect is stronger in the part of the YBCO film under direct contact with

PCMO, significant suppression of T_c is also achieved in the far away region of YBCO film which is not covered by PCMO. Simultaneous use of multiple sources of external perturbation can enhance the nucleation of FM clusters and thus can create a new possibility to effectively control the spin injection effect into the manganite/superconductor hetero-structure. Detailed investigations on PCMO/YBCO/PCMO tri-layer heterostructures have been used to demonstrate this concept of simultaneous use of two or more external perturbations to influence the formation of FM regions in PCMO. The trilayer was deposited on MgO substrate. There is a 9.4% lattice mismatch between the MgO and PCMO and thus PCMO film with thickness (~40 nm) lower than a threshold experiences a substrate induced strain. This lattice strain can assist the formation of FM clusters in PCMO. Magnetoresistance measurements have been performed on the trilayers using two different sets of current (1mA and 5mA) applied to the top PCMO layer. The investigations on the T_c for this trilayer for different values of applied magnetic fields and currents reveals that the suppression of T_c is much higher for the trilayer compared to that for the bilayer (where strain as a parameter was absent). The suppression of T_c due to the applied current has been measured to be ~ 0.8K/mA for the trilayer whereas the value was only ~0.35K/mA for the bilayer. Both substrate induced strain and electric field (current) are responsible for the nucleation of the FM clusters in bottom and top PCMO layers respectively and this results in a higher quasiparticle spin injection effect as well as the direct proximity effect of FM phase on the superconducting YBCO layer. These results demonstrate that strain can be used to control the formation of FM clusters just like applied current. These experimental results demonstrate the possibility of using controlled formation of FM clusters in PCMO as a source of spin injection in YBCO and thereby control the T_c of the YBCO.

7.2 Future Scope:

The experimental studies on PCMO/YBCO thin film heterostructures unveil the potential of using external perturbations such as substrate induced strain, applied current, and magnetic field as control variables to influence the superconducting transition temperature T_c of the superconducting YBCO layer in a thin film PCMO/YBCO heterostructure. These experimental investigations open up a new opportunity to use these properties for the realization of novel spin injection devices by suitable choice of materials of charge ordered manganites and high T_c superconductors. It may be noted that controlled growth of these multilayer heterostructures and the related interface studies are required to realize these devices. There is a scope to further promote the melting of charge ordered phase of manganites by choosing substrates with even higher lattice mismatch (~ 10 %). There is also a possibility to use a number of external perturbations simultaneously to create a situation inside the charge ordered manganites where a small value of applied current or external magnetic field can bring about drastic changes in the physical properties. There are possibilities to induce 0 to π transition in superconductor/manganite/superconductor multilayer heterostructures, a phenomenon of considerable contemporary interest. In general, it is known that the thickness of FM layer governs the nature of coupling of the superconducting order parameters of the two superconducting layers in SC/FM/SC trilayer structures [13-16]. Once the thickness of FM layer is fixed in a multilayer, it cannot be used to induce the transition from 0 to π

phase. However, in SC/manganite/SC heterostructures, it may be possible to use external perturbations to influence the sign of the coupling of order parameters in the two superconducting layers separated by a manganite layer. In these heterostructures, the size and density of FM clusters inside the manganite layer can be varied by the external perturbations without changing the thickeness of the deposited manganite layer. Our experimental studies on a partially masked YBCO/PCMO bilayer demonstrate the possibility of controlling the superconducting properties of the unmasked YBCO part using a control variable to influence the nucleation of FM clusters in the PCMO layer that covers only a part of the YBCO thin film.

References:

[1] A. Asamitsu, Y. Tomioka, H. Kuwahara and Y. Tokuta, *Nature 388, 50 (1997)*.

[2] Z. Q. Yang, R. W. A. Hendrikx, P. J. M. V. Bentum and J. Aarts *Europhys. Lett. 58, 864 (2002).*

[3] V. Kiryukhin, D. Casa, J. P. Hill, B. Kelmer, A. Vigliante, Y. Tomioka and Y. Tokura, *Nature 386, 813 (1997).*

[4] Y. Tomioka, A. Asamitsu, H. Kuwahara, Y. Moritomo and Y. Tokura *Phys. Rev. B 53, R1689 (1996).*

[5] M. Hervieu, A. Barnabe, C. Martin, A. Maignan and B. Raveau *Phys. Rev. B 60, R726 (1999).*

[6]C. S. Nelson, J. P. Hill, D. Gibbs, M. Rajeswari, A. Biswas, S. Shinde, R. L. Greene, T Venkatesan, A. J. Millis, F. Yokaichiya, C Giles, D Casa, C. T. Venkataraman and T. Gog *J. Phys.*: *Condens. Matter 16, 13 (2004)*

[7] Dipak Kumar Baisnab, T. Geetha Kumary, A. T. Satya, Awadhesh Mani, J. Janaki, R. Nithya, L. S. Vaidhyanathan, M. P. Janawadkar and A. Bharathi *J. Magn. Magn. Mater. 323, 2823 (2011)*

[8] Daniel Hsu, J. G. Lin, C. P. Chang, C. H. Chen, C. H. Chiang, W. C. Chan and W. F. Wu *J. Appl. Phys. 103, 07C710 (2008)*

[9] J. G. Lin, Daniel Hsu, W. F. Wu, C. H. Chiang and W. C. Chan *J. Appl. Phys., 101, 09G106 (2007)*

[10] J. G. Lin, S. L. Cheng, C. R. Chang and D. Y. Xing *J.Appl.Phys. 98, 023910(2005)*

[11] Daniel Hsu, J. G. Lin, C. P. Chang, C. H. Chen, W. F. Wu,C. H. Chiang and W. C. Chan *Appl. Phys. Lett. 90, 162504 (2007)*

[12] W. Westhauser, S. Schramm, J. Hoffmann and C. Jooss *Eur. Phys. J. B 53, 323 (2006)*

[13] Z. Radovi´c, M. Ledvij, L. Dobrosavljevi´c-Gurji´c, A.I. Buzdin and J.R. Clem, Physical Review B 44, 759 (1991).

[14] Th. Muhge, N.N. Garif'yanov, Yu.V. Goryunov, G.G. Khaliullin, L.R. Tagirov, K. Westerholt, I.A. Garifullin and H. Zabel, Physical Review Letters 77, 1857 (1996).

[15] L.V. Mercaldo, C. Attanasio, C. Coccorese, L. Maritato, S.L. Prischepa and M. Salvato, Physical Review B 53, 14040 (1996).

[16] J.S. Jiang, D. Davidovi´c, D.H. Reich and C.L. Chien, Physical Review B 54, 6119 (1996).

List of Publication

(Included in thesis)

1. Intricacies of Strain and Magnetic Field Induced Charge Order Melting in $Pr_{0.5}Ca_{0.5}MnO_3$ Thin Films
   Dipak Kumar Baisnab T. Geetha Kumary, A. T. Satya, Awadhesh Mani, J. Janaki, R. Nithya, L.S. Vaidhyanathan, M.P. Janawadkar, and A. Bharathi, Journal of Magnetism and Magnetic Materials, 323, (2011) 2823

2. Evolution of Ferromagnetic clustering in $Pr_{0.5}Ca_{0.5}MnO_3$ and its effect on the Critical Temperature of YBa2Cu3O7 thin film
   Dipak Kumar Baisnab T. Geetha Kumary, A. T. Satya, Awadhesh Mani, R. Nithya, L. S. Vaidhyanathan, M. P. Janawadkar and A. Bharathi, Journal of Applied Physics, 111 (2012) 113910

3. Current Dependent Proximity Effects in $Pr_{0.5}Ca_{0.5}MnO_3/YBa_2Cu_3O_7$ Bilayer
   Dipak Kumar Baisnab T. Geetha Kumary, A. T. Satya, Awadhesh Mani, L. S. Vaidhyanathan, M. P. Janawadkar and A. Bharathi,, Journal of Nanoscience Letters 3:13 (2013)

4. The effects of strain, current and magnetic field on superconductivity in trilayer $Pr_{0.5}Ca_{0.5}MnO_3$ /$YBa_2Cu_3O_7$/ $Pr_{0.5}Ca_{0.5}MnO_3$
   Dipak Kumar Baisnab, M. P. Janawadkar, Shilpam Sharma, R. M. Sarguna, L. S. Vaidhyanathan and A. Bharathi , Journal of Applied Physics, 2013 (Accepted)

5. Effect of current induced charge-order melting of $Pr_{0.5}Ca_{0.5}MnO_3$ in partially masked superconducting $Pr_{0.5}Ca_{0.5}MnO_3$/ $YBa_2Cu_3O_7$ bilayer film
   Dipak Kumar Baisnab et al. (to be comunicated)

Conference

6. Strain Enhanced charge-order melting in Pr0.5Ca0.5MnO3 thin films
   Dipak Kumar Baisnab T. Geetha Kumary, A. T. Satya, Awadhesh Mani, J. Janaki, R. Nithya, L. S. Vaidhyanathan, M. P. Janawadkar and A. Bharathi AIP Conf. Proc. 1347 (2011) 199

7. Effect of Current Induced Charge Order Melting of Pr0.5Ca0.5MnO3 on YBa2Cu3O7 Thin Film
   Dipak Kumar Baisnab T. Geetha Kumary, A. T. Satya, Awadhesh Mani, R. Nithya, L. S. Vaidhyanathan, M. P. Janawadkar and A. Bharathi, AIP Conf. Proc. 1447 (2012) 675

8. Spin injection effects in superconductor / manganite multilayer structures
   Dipak Kumar Baisnab, A. Bharathi, L. S. Vaidhyanathan and M. P. Janawadkar, MRSI-AGM- 2013, February 11-13, IGCAR, Kalpakkam, Tamilnadu, India

(Not included in thesis)

9. Superconducting $Fe_{1+\delta}Se_{1-x}Te_x$ thin films: Growth, characterization and properties
T. Geetha Kumary, Dipak Kumar Baisnab et. al, Superconductor Science and Technology, 22 (2009) 095018

10. Synthesis of β-Ga_2O_3 nano-particles embedded in Nb matrix by radiofrequency co-sputtering.
L.S. Vaidhyanathan, M.P. Janawadkar, D. K. Baisnab et. al, International Symposium on Materials Chemistry-2008 , Mumbai (2-6th December, 2008).

11. Development of High Tc Superconducting Quantum Interference Devices
L. S. Vaidhyanathan, D. K. Baisnab, and M. P. Janawadkar , AIP Conf. Proc. 1349, (2011)463

12. Synthesis and low temperature studies of the Fe1+δTe system
J.Janaki, T.GeethaKumary, Awadhesh Mani, Dipak Kumar Baisnab et. al, DAE SSPS-2009

13. Resistivity of thin films of $YBa_2Cu_3O_{7-\delta}$ and Multilayers of YBCO/Ga_2O_3
L.S.Vaidhyanathan, D. K. Baisnab et. al, PLD-2007, DAE-BRNS 4th National Symposium on PLD of thin films & Nanostructured materials.

14. Superconductivity inYBCO/Ga_2O_3 Multilayers
L.S.Vaidhyanathan, D. K. Baisnab et. al, 52, DAE Solid State Physics Symposium-2007

15. Development and utilization of SQUID sensors
M.P. Janawadkar, R. Baskaran, L S Vaidhyanathan, R Nagendran, K Gireesan, D. K. Baisnab et. al, Eeast Asia Symposium on Superconductor Electronics held at IIT Delhi(Dec 11-15, 2007).